

8-2018

# Development of Biomimetic Models of Human Cardiac Tissue

Dylan Jack Richards

Clemson University, [djack.richards@gmail.com](mailto:djack.richards@gmail.com)

Follow this and additional works at: [https://tigerprints.clemson.edu/all\\_dissertations](https://tigerprints.clemson.edu/all_dissertations)

---

## Recommended Citation

Richards, Dylan Jack, "Development of Biomimetic Models of Human Cardiac Tissue" (2018). *All Dissertations*. 2192.  
[https://tigerprints.clemson.edu/all\\_dissertations/2192](https://tigerprints.clemson.edu/all_dissertations/2192)

This Dissertation is brought to you for free and open access by the Dissertations at TigerPrints. It has been accepted for inclusion in All Dissertations by an authorized administrator of TigerPrints. For more information, please contact [kokeefe@clemson.edu](mailto:kokeefe@clemson.edu).

DEVELOPMENT OF BIOMIMETIC MODELS OF  
HUMAN CARDIAC TISSUE

---

A Dissertation  
Presented to  
the Graduate School of  
Clemson University

---

In Partial Fulfillment  
of the Requirements for the Degree  
Doctor of Philosophy  
Bioengineering

---

by  
Dylan Jack Richards  
August 2018

---

Accepted by:  
Dr. Ying Mei, Committee Chair  
Dr. Martine LaBerge  
Dr. Donald Menick  
Dr. Hai Yao

## ABSTRACT

The leading cause of death worldwide is cardiovascular disease (CVD). Myocardial infarction (MI) (i.e., heart attack) makes up ~8.5% of CVD and is a common cause of heart failure with a 40% five-year mortality after the first MI. This highlights a substantial patient population and an urgent need to develop new therapeutic strategies (e.g., regenerative cell therapies). Moreover, this also indicates that current models may not sufficiently recapitulate human cardiac tissue. To date, drug development strategies have largely depended on high throughput 2D cell models and pre-clinical testing in animal models of MI leading to minimal improvements in the heart failure treatment paradigm over the past 20 years. Relevant human cardiac models would provide insight into human cardiac tissue physiology and maturation while also providing an advanced in vitro screening tool to explore heart failure pathogenesis. Cardiac tissue engineering has allowed for advances in the development of cardiac constructs by combining developments in biomaterials, 3D microtissue culture, and human induced pluripotent stem cells (hiPSC) technology. Notably, approaches that mimic the natural processes in the body (i.e., biomimetic) have led to further insight into cardiac physiology. Here, I have pursued biomimetic strategies to create a biomimetic model of human cardiac tissue using hiPSC-derived cardiomyocytes (hiPSC-CMs). Throughout this development, I explored the role of the matrix microenvironment on cell behavior using functionalized alginate, the influence of pacemaker-like exogenous electrical stimulation on the maturation of hiPSC-CM spheroids with endogenous electrically conductive

nanomaterials, and the development of vascularized, functional cardiac organoids by mimicking the coronary vasculogenesis stage of cardiac development. The research established here provided a biomimetic groundwork for future development into in vitro human cardiac tissue models for applications in basic research, drug discovery, and cell therapy.

## ACKNOWLEDGMENTS

I would like to acknowledge Clemson University's Bioengineering Department overall for creating the connection with the Medical University of South Carolina (MUSC), the Department of Cell Biology and Regenerative Medicine at MUSC for providing the training environment for translational bioengineering research, and the Center for Genomic Medicine for helping me to expand my individual pursuit into bioinformatics. I also thank the laboratories in the Gazes Cardiac Research Institute and those supporting the NIH NHLBI T32 Training Grant "Training to Improve Cardiovascular Therapies" for providing mentorship, training courses, and funding for my research. In addition to institutional support, I also acknowledge all of the faculty that taught my courses and helped guide my decision making throughout my doctoral experience. I appreciate all of the guidance and mentor relationship of Dr. Menick throughout my research as he served as my co-mentor while under the T32 grant. I acknowledge my committee members and in guiding and encouraging me throughout each step of my PhD. I would like to acknowledge my advisor, Dr. Mei, for his guidance, funding, mentor relationship, and continual drive to push me to aim for the best research. His support enabled me to freely pursue and hone my best ideas. I thank my fellow classmates and lab mates who worked with me for expanding my own research skills and perspectives, as well as for their honest relationships that extended beyond our daily lab duties into daily life. Most importantly, I would like to thank my wife for her ongoing support along every step and enduring through this part of life with me to the end.

## LIST OF TABLES

Table	Page
1.1 Viability of the alginate samples at day 0, day 4, and day 8.....	39
2.1 Taqman primers used for gene analysis .....	63

## LIST OF FIGURES

Figure	Page
1.1 Schematic representation of biodegradable oxidized alginate as bioink for bioprinting.....	16
1.2 Density-based analysis on printability of different alginate solutions .....	18
1.3 Viscosity-based analysis on printability of different alginate solutions .....	20
1.4 Cell viability assay of density and viscosity criterion-filtered samples .....	22
1.5 Summary table of the preferable range of alginate samples with high printability (green) based on the three established printability criteria (i.e., homogeneous cell suspension, high printing resolution, and high cell viability) .....	23
1.6 Lattice structures printed with bioprinting-compatible materials and their dimensional change in 8 days. ....	25
1.7 hADSC behavior in the lattice structures.....	27
1.8 A computer-rendered 3D picture of a portion of the printed lattice structure made by the best supporting hADSC material, 5% ox.-15% conc. oxidized alginate, showing multiple layers of spreading cells within the hydrogel.....	29
1.9 A proof-of-concept analysis of the necessity of 1% (w/w) RGD peptide-conjugated alginate for changing cell function .....	37
1.10 $\alpha_v\beta_3$ integrin expression of hADSCs in alginate hydrogels with and without RGD conjugation at day 0, day 4, and day 8.....	38

## List of Figures (Continued)

Figure	Page
2.1 Development of electrical stimulation for nanowired hiPSC cardiac spheroid .....	44
2.2 Synergistic contribution of electrical stimulation and nanowires to cellular junction formation .....	46
2.3 Nanowires influence sarcomeric organization in hiPSC cardiac spheroids .....	48
2.4 Nanowires and electrical stimulation affect development of contractile machinery in hiPSC cardiac spheroids.....	50
2.5 Electrical stimulation and nanowires directly affect subpopulation specification and beating properties in hiPSC cardiac spheroids .....	52
2.6 hiPSC cardiac spheroid assembly.....	61
2.7 Gene expression analysis of hiPSC cardiac spheroids .....	62
3.1 Developmental inspiration for organoid fabrication.....	67
3.2 Examination of developmental inspiration for cardiac cell ratio for organoid fabrication .....	69
3.3 The addition of human adipose derived stem cells improves biomimetic formation of functional, lumenized vascular networks in cardiac organoids.....	71
3.4 The addition of human adipose derived stem cells affects biomimetic cellular organization and introduces immunomodulatory effects.....	75
3.5 Human cardiac organoids display organotypic extracellular matrix (ECM) components.....	77



## List of Figures (Continued)

Figure	Page
3.6 Human cardiac organoids support contractile development of hiPSC-CMs .....	79
3.7 Human cardiac organoids display phenotypic channel functionality and organotypic responses to physiological/pathological stimuli .....	83
3.8 Experimental timeline of human cardiac organoids.....	96
3.9 The ratio of cells in cardiac organoids influences contractile development.....	97
3.10 Culture media screening using TUNEL staining (green) for apoptotic nuclei of D0 cardiac organoids .....	98
3.11 Confocal imaging of immunofluorescently stained whole cardiac organoids (D10) show lumenized vascular network.....	99
3.12 Analysis of individual cell types and cardiac organoids regulation of angiogenic gene expression in human cardiac organoids at D10 .....	100
3.13 Evaluation of putative vasculature using an oxygen-reduced environment .....	101
3.14 Evaluation of putative vasculature using macrotissue assembly .....	102
3.15 Endothelial cell source affect structural functionality.....	103
3.16 Both hiPSC-CM spheroids and cardiac organoids showed immunofluorescent expression of laminin that did not change significantly over time.....	104
3.17 Human cardiac organoids support contractile development of hiPSC-CMs.....	105

## List of Figures (Continued)

Figure	Page
3.18 Functional analysis of human cardiac organoids and hiPSC-CM spheroids .....	106
3.19 Response of individual cell types to ischemia on D10.....	107

## TABLE OF CONTENTS

	Page
TITLE PAGE .....	i
ABSTRACT.....	ii
ACKNOWLEDGMENTS.....	iv
LIST OF TABLES.....	v
LIST OF FIGURES.....	vi
CHAPTER	
I. THE NEED FOR BIOMIMETIC CARDIAC MODELS.....	1
Introduction .....	1
Applications in Basic Research.....	2
Applications in Drug Discovery .....	5
Applications in Cell Therapy.....	8
II. UNDERSTANDING THE CELL MICROENVIRONMENT THROUGH BIOINK INK DEVELOPMENT FOR BIOPRINTING .....	14
Introduction .....	14
Results and Discussion .....	16
Conclusions .....	30
Materials and Methods.....	31
Supporting Information .....	37
III. NANOENGINEERED SOLUTIONS TO FACILITATE HUMAN CARDIAC MICROTISSUE DEVELOPMENT .....	40
Introduction .....	40
Results and Discussion .....	43
Conclusions .....	53
Materials and Methods.....	56
Supporting Information .....	61

Table of Contents (Continued)	Page
IV. DEVELOPMENT-DRIVEN INSPIRATION FOR BIOMIMETIC SELF-ASSEMBLY OF HUMAN CARDIAC ORGANIDS.....	64
Introduction .....	64
Results and Discussion .....	67
Conclusions .....	86
Materials and Methods.....	88
Supporting Information .....	96
V. FUTURE DIRECTION AND OUTLOOK .....	108
REFERENCES .....	110

## CHAPTER ONE

### THE NEED FOR BIOMIMETIC CARDIAC MODELS

#### **Introduction**

Cardiovascular disease is the leading cause of death and disability worldwide, claiming more lives than all types of cancers combined.<sup>1</sup> Ischemic heart disease (IHD) and myocardial infarction (MI) are major contributors to cardiovascular morbidity and mortality.<sup>2</sup> The treatment of the heart failure from myocardial infarction has slowly evolved over the past decades. A major turning point for restoring heart function was the scientific evidence that thrombus formation led to myocardial infarction and not vice versa.<sup>3-5</sup> After myocardial infarction, the affected cardiomyocytes begin to die and are replaced with a collagenous scar within weeks. The adjacent myocardium continues to create tension on the scar region with every beat, causing the damaged ventricular wall to thin and dilate. With a larger ventricular volume but less functional myocardium, the heart can no longer maintain cardiac output and eventually leads to heart failure. This led to the, now common, practice of reperfusion therapy upon arriving to the hospital. Despite restored blood flow, the lack of sufficient regeneration to replace damaged tissue and the constant demand to pump blood to the entire body causes the heart to progressively fail.<sup>6</sup>

Today the most common treatment is to reduce demand on the heart with therapeutic strategies (e.g, beta-blockers) or completely replace the heart with either a heart transplant (limited by donor supply) or with a left ventricular assist device (LVAD).

Despite prolonging life, this status quo for heart failure treatment remains limited by not achieving a restoration of heart function through regeneration of myocardium. Presently, the only long-term solution is cardiac transplantation, a procedure severely limited by the shortage of donor heart and by cost.<sup>7,8</sup> Due to the limited regeneration capacity of adult human hearts, the human induced pluripotent stem cell (hiPSC) has emerged as a powerful cell source for cardiac repair due to its proven capacity to produce patient-specific functional cardiomyocytes.<sup>9-13</sup> In addition, recent progress in cardiac differentiation of hiPSCs allows for the derivation of the large amount of patient-specific human cardiomyocytes ( $\sim 1 \times 10^9$  cells/patient), including from heart failure patients, needed for the idealized cardiac repair or large scale drug screening.<sup>14-18</sup> Despite the progress in heart failure treatment in the last 50 years, notably less progress has been made in the last decade to advance the heart failure therapeutic paradigm.<sup>19,20</sup> Development of a biomimetic model to recapitulate the tissue-level dynamics of human ventricular cardiac tissues would provide a valuable tool to further investigate the physiology and pathology of human hearts and their diseases.

### **Applications in Basic Research**

Although hiPSC-CMs provide a human cardiomyocyte model, the complexity of the multi-cellular nature and developmental stage of adult ventricular myocardium has led to significant challenges in modeling human cardiac tissue in vitro. The current cardiomyocytes derived from hESCs and hiPSCs retain an immature phenotype, including

poor contraction, metabolism, structure, and electrophysiology.<sup>21-24</sup> During embryonic development, environmental factors (e.g., extracellular matrix- ECM, growth factors, mechanical and electrical stimulation) have major effects on the maturation of cardiomyocytes. To mimic the maturation process *in vitro*, hESC- and hiPSC-derived cardiomyocytes have been mixed with scaffolding materials (e.g., Matrigel and collagen type I gel) to prepare cardiac tissue-engineered constructs and then conditioned with electrical and/or mechanical stimulation.<sup>21,25-27</sup> While these scaffolds can provide tissue-like 3D microenvironments, current scaffolding materials lack the matched physical/chemical/biological properties with the native extracellular environments during heart development. On the other hand, scaffold-free, 3D cardiac spheroids have emerged as promising model systems to mimic cardiac tissues by providing a consistent, high throughput method to produce microtissue with biomimetic cell densities that rely on self-assembly mechanisms and endogenous scaffolding material production (i.e., ECM).<sup>28,29</sup>

Various tissue-engineering strategies have been utilized to mimic adult host ventricular myocardium to accelerate phenotypic development of hiPSC-CMs.<sup>21,30-36</sup> To this end, several groups have used electrical stimulation as an exogenous approach to recapitulate the natural pacemaker-initiated excitation of cardiomyocyte contraction to advance the function of hESC/hiPSC-CMs.<sup>21,35,37-42</sup> Eng and others demonstrated that electrical conditioning of 3D cardiac embryoid bodies promotes cellular maturity of hiPSC-CMs and affects intrinsic beating characteristics.<sup>39</sup> Likewise, electrical nanomaterials have

provided an endogenous means of improving electrical conductivities of cardiac microtissues.<sup>43-45</sup>

A combination of tissue-engineered strategies may be required to advance the functional assembly of hiPSC-CMs. In vitro methods, including mechanical and exogenous electrical stimulation, 3D microtissue culture, and capillary-like nutrient/drug delivery, have targeted physiologically relevant features that improved in vitro cardiomyocyte development.<sup>25,39,46-49</sup> For example, Thavandiran and coworkers combined the aligned features of the myocardium with electrical stimulation to improve the functional development of cardiac microtissues.<sup>50</sup> To mimic myocardial nutrient exchange, Mathur and coworkers showed that microfabricated channels surrounding CM constructs provided capillary-like diffusion that improved the physiological relevance of drug screening.<sup>46</sup> To improve cell viability and integration after transplantation into infarcted hearts, Stevens and coworkers fabricated pre-vascularized cardiac patches that can connect to the host vasculature.<sup>51</sup> In the most recent pursuit of ventricular cardiac tissue maturation, Ronaldson-Bouchard and others used a fibrin-based anisotropic hiPSC-CM microtissue model with 25% dermal fibroblasts to construct a microtissue that was electrically stimulated at increasing speeds that resulted in major hallmarks in mature ventricular cardiomyocytes including sarcomere M-line ultrastructures, ventricular-like electrophysiology and calcium handling, T-tubules, and oxidative phosphorylation shifts in metabolism.<sup>52</sup> In this study, they provided evidence that earlier hiPSC-CM in vitro age



increased its in vitro maturation potential in a shorter time, suggesting hiPSC-CM development may involve several stages of lineage commitment.

While previous approaches allow for focused study on hiPSC-CM function and maturation, there has been limited progress towards the development of an organotypic functional 3D cardiac model of the working myocardium. The heart is composed of more than simply cardiomyocytes and fibroblasts and independent studies have supported the benefit of additional cell types in improving overall tissue function, such as improved conduction velocity or vascularization.<sup>32,39,51,53-55</sup> The human induced pluripotent stem cell (hiPSC)-enabled development of human organoids has provided a powerful platform for isogenic disease modeling and investigation of developmental biology that inherently contains a variety of cell types.<sup>56-58</sup> To this end, a variety of functional tissue organoids (e.g., kidney, liver, brain) have been developed with the purpose of recapitulating major organ functions and structures, yet few studies have focused on the development of human cardiac organoids. A biomimetic approach for human organoid design may provide an accessible multi-dimensional in vitro model that can give further insight into tissue development without the need for more expensive, less human-specific animal models of heart tissue.

### **Applications in Drug Discovery**

Despite improvements in heart failure therapies in the past 50 years, it was only recently that the PARADIGM-HF trial proved to be the first in 30 years to show a new drug

outperforming treatment developed in the late 1980s.<sup>59,60</sup> From 2003 to 2011, the likelihood of FDA approval of cardiovascular disease therapies from Phase I was 7%, which is below the average likelihood for all major disease categories (10%), and had the lowest success rate from Phase II (26%).<sup>61</sup> In addition to clinical trial design, this has been, in part, attributed to translational discrepancies of preclinical data to outcomes in humans.<sup>62,63</sup> While many single pathways (e.g., B-AR biased ligands) and contributing cell types (e.g., epicardial cell) in heart failure have been thoroughly studied in single cell systems, the tissue-level response is only screened in the context of preclinical/clinical models. Although preclinical models provide a whole-organism context to evaluate novel therapies, tissue-specific characteristics and disease progression have notable differences across species, especially in smaller mammals (e.g. mouse).<sup>64-66</sup>

Given the differences between species, recent progress in human induced pluripotent stem cell-derived cardiomyocyte (hiPSC-CM) technology has aimed to incorporate hiPSC-CM 2D models to drug development/safety pipelines.<sup>67,68</sup> Current standards for drug cardiotoxicity evaluation focus on detection of delayed ventricular repolarization, which is strongly associated with fatal ventricular arrhythmias, including torsades de pointes.<sup>69</sup> hERG channel blockade and QT interval prolongation in electrocardiograms have been used as the industry standard targets for detection. The evaluation methods usually involve overexpressed non-cardiac cell types (e.g., hERG-transfected CHO cells) and electrocardiogram assays in animal models (e.g. Langendorff-perfused rabbit hearts).<sup>70-73</sup> While these methods have successfully reduced drug

withdrawals, they also limited the pace and productivity of drug evaluation by eliminating potentially effective drugs that operate through alternative pathways (e.g., multi-channel effects).<sup>69,74</sup> Developing novel high throughput drug cardiotoxicity screening systems using hiPSC-CMs with the improved clinical relevance would greatly accelerate the pace of therapeutic discovery as it can allow for robust derivation of patient-specific human cardiomyocytes (hiPSC-CMs).<sup>15,16,75-78</sup> To this end, several reports have shown the feasibility of the utilization of the conventional 2D hiPSC-CM culture system for drug arrhythmogenic tests.<sup>79-84</sup> In addition, tissue engineering strategies have been employed to assemble hiPSC-CMs into 3D cardiac (micro-)tissues to mimic structural features of myocardium (e.g., cell alignment, capillary-like media flow) to improve their physiological relevance, drug cardiotoxicity predictability and reduce drug response variation.<sup>26,46,85,86</sup> However, the lack of control in the hiPSC-CM assembly process hinders the formation of proper cell-cell junctions and leads to the compromised cardiac functions (e.g., unsynchronized contraction). Further, the drug response data found in human adult ventricular tissue slices differs significantly from the existing hiPSC-CM systems. This has been, at least partially, attributed to the overall immature phenotype of the current hiPSC-CMs.<sup>87</sup>

This highlights an unmet need to develop a biomimetic in vitro human model that incorporates tissue-level properties to provide a representative screening platform that shares functional and species similarities to humans prior to animal studies. This would reduce novel candidates earlier in the pipeline and thereby accelerate and improve

accuracy of heart failure drug development. Given the patient-specific nature of induced pluripotent stem cell (iPSC) technology, the majority of translational iPSC-based organoid work has focused on genetic disorders to treat with gene-targeted approaches (e.g., CRISPR-Cas9) or to serve as a patient-specific drug screening platform.<sup>88-92</sup> In addition to heart failure, congenital heart disease occurs in ~1% of live births, ~10% of aborted fetuses, and is the leading cause of mortality from birth defects.<sup>93,94</sup> Biomimetic cardiac model design can also contribute to this significant medical need by incorporating patient-specific iPSC-cardiac models to address genetic mutation disorders.<sup>95-101</sup> For example, Wang and others provided new insight into the pathogenesis of Barth syndrome that linked this mitochondrial cardiomyopathy with contractile dysfunction that was facilitated by a tissue-level hiPSC-CM model.<sup>102</sup>

### **Applications in Cell Therapy**

In addition to purely in vitro models, biomimetic human cardiac models also hold promise in the design of advanced cell therapy vehicles to maximize their regenerative capacity. The field of cell therapy provides an injection-based strategy (i.e., intravenous, intracoronary, or intramyocardial delivery) to regenerate lost myocardium that avoids the highly invasive surgery needed for heart transplantation, LVAD insertion, and proposed tissue engineered patch strategies.<sup>103</sup> Traditionally, adult stem cells (e.g., mesenchymal stem cells) have been a common source of exploration due to their multipotency and availability in adults. Additionally, advances in induced pluripotent stem cell (iPSC)

technology has furthered this potential with a patient-specific cell source, avoiding life time immunosuppressant therapy in the case of heart transplants and/or allogeneic cells.<sup>100,104</sup>

The guiding principal for cardiac cell therapy has largely been focused on the pluripotency and proliferative capacity of the injected cells over other strategies, such as mimicking naturally occurring regenerative/survival mechanisms. The initial research evaluation of the efficacy of embryonic stem cells (ESCs) showed a trend of cell survival and modest improved cardiac function in the rat infarct model.<sup>105-108</sup> However, in-depth analysis of ESC transplantation in the uninjured and injured heart has shown teratoma formation in allogeneic and syngeneic recipients and increased immunological response.<sup>109-111</sup> These results indicate that 1) the heart may not provide sufficient signals for in situ differentiation of pluripotent stem cells, 2) an ESC-based method would require a level of immunosuppressant therapy, and 3) a more differentiated cell type may be necessary for successful integration and long term benefits.

Based on the ground work in pluripotent and multipotent stem cell transplantation in infarcted hearts, it can be reasoned that cells with a cardiac-committed lineage may have the most regenerative potential due to their ability to differentiate into cells important for cardiac repair, such as cardiomyocytes and endothelial cells.<sup>112</sup> For the extent of this discussion, cardiac-committed cells will not be fully defined, but include cardiopoietic cell strategies (e.g., c-kit<sup>+</sup> stem cells, cardiosphere-derived cells). To explore the therapeutic benefit of a cardiac-committed stem cell population, Menasche's group

in 2005 conducted a preclinical study using cardiac-committed mouse ESCs in an infarcted sheep model that showed differentiation into cardiomyocytes and an increase in ejection fraction from 39% to 45.6% after 1, whereas media-inject controls decreased from 43% to 33.1%.<sup>113</sup> Marban's group then investigated the efficacy of cardiosphere-derived cells expanded from percutaneous endomyocardial biopsy specimens in a porcine model that showed an increase in ejection fraction from ~41% to 44% after 8 weeks while the PBS injected control changed from 42% to 36%.<sup>114</sup> These studies helped to launch human cardiac-committed cells to human trials to make up the next generation of cell therapy strategies for heart failure.<sup>115</sup>

Most recently, the C-CURE trial investigated the efficacy of cardiopoietic stem cell derived from mesenchymal stem cells in chronic heart failure patients using an endoventricular guided catheter delivery of  $600-1,200 \times 10^6$  cells that can electromechanically map viable and dysfunctional myocardium for precision-mapped injection.<sup>116</sup> This cell therapy resulted in significant improvements in ejection fraction (from ~27% to ~34% in treated) with no improvements in standard-of-care controls. Overall, there seems to be improvements in function with cardiac-committed cell therapy in the short term analysis of these early stage approaches, but more trials on larger populations must be conducted to obtain a more accurate representation of treatment efficacies. Furthermore, the number of cells needed for current cell therapy strategies emphasize the need for improved methods for cell retention.

Heart failure after myocardial infarction is caused in part by the inability of the sufficient force generation due to lack of healthy myocardium. With this aspect of the problem in sight and with improved protocols for cardiomyocyte differentiation, many groups have explored the use of stem cell-derived cardiomyocytes as the cell source for cardiac cell therapy. This method does not depend on in situ differentiation after transplantation and therefore theoretically could accelerate the regeneration of force-generating myocardium. Initial studies using neonatal rat cardiomyocytes results validated the basis for the use of stem cell-derived cardiomyocytes, as they are also not fully matured cardiomyocytes.<sup>24,30</sup> Initial studies of human embryonic stem cell-derived cardiomyocyte (hESC-CM) cell therapy confirmed their survivability and electromechanical integration of after transplantation into uninjured and electrophysiologically silenced.<sup>117-119</sup> Based on the previous research in smaller animal models and the progression of stem cell-derived cardiomyocyte culture (both hESC-CMs and hiPSC-CMs), a large animal model was explored recently to evaluate the feasibility of mass production of stem cell-derived cardiomyocytes and efficacy of intramyocardial delivery in a non-human primate model (macaque, 100-150 BPM), of myocardial ischemia-reperfusion injury.<sup>120</sup> This study involved injection of  $1 \times 10^9$  hESC-CMs that showed substantial remuscularization (averaging 40% of infarct volume), perfusion by host vasculature, and graft-host electromechanical junctions that increased over 84 days after injection. Functional metrics (e.g., ejection fraction) among hearts receiving hESC-CM showed no significant trends given the limited injured after ischemia-reperfusion

compared to an infarction model. However, it must be considered that sample sizes of this study were 1 at 14 days, 2 at 28 days, and 1 at 84 days, statistically limiting any conclusions on efficacy. In regards to the electrophysiology, all animals showed no arrhythmias prior to injection, but all developed arrhythmias after receiving hESC-CMs (i.e., premature ventricular contractions and periods of ventricular tachycardia). Most notably, this data contrasts with the previous work in small animal models and has led to increased discussion about stem cell-derived cardiomyocyte safety concerns.<sup>121</sup> This also emphasizes the need to further understand the capacity of stem cell-derived cardiomyocytes, which may require improved in vitro models to increased understanding of hiPSC-CM maturation prior to injection or other strategies to promote favorable integration.

Given the diverse approaches for cardiac cell and biomaterial therapy with modest improvements, a multi-dimensional approach may be ideal solution. Many groups are exploring combining cell types and technologies to address each obstacle for successful retention and integration. Developmental mechanisms for vascularization of forming heart has inspired the use of epicardial-derived progenitor cells in conjunction with cardiac progenitor cells that has shown to be more angiogenic and resistant to hypoxia leading to improvements ejection fraction in mice.<sup>122</sup> Multicellular aggregates with controlled assembly or hybrid cell types have been more frequent in efforts to take advantage of resistant cell types and pro-angiogenic features for improved integration.<sup>123-</sup>

<sup>126</sup> With enhanced technology and techniques (e.g., RNA-seq, microarrays) to analyze



large amounts of data and combinations of data, the injection-based therapy approach to cardiac repair may not be only dependent on what cell type is best, but what combination of cells, materials, and factors has the strongest biomimetic rationale to withstand and regenerate the harsh cardiac injury environment.

## CHAPTER ONE

### UNDERSTANDING THE CELL MICROENVIRONMENT THROUGH BIOINK INK DEVELOPMENT FOR BIOPRINTING

#### **Introduction**

Three-dimensional (3D) bioprinting technology has provided an enhanced feasibility and precision for tissue engineered construct fabrication.<sup>127-135</sup> Compared with the traditional tissue fabrication methods, 3D bioprinting offers a reproducible, scalable fabrication methodology with precise 3D control. It allows for the fabrication of mechanically supportive 3D structures with bioactive/cellular components for a variety of biomedical applications, including regenerative medicine, in vitro disease models, and the exploration of fundamental cell and tissue-level mechanisms.<sup>136-143</sup> For tissue engineering, the ideal 3D-printed construct would be a growth-directing structure on which cells could migrate and proliferate to form a functional tissue. While genetics can control cell fate, the research in this field has proven to be tedious and rather complex.<sup>144</sup> In addition to the difficulty of using genetic tools to direct cell fate, epigenetics has shown that covalent and noncovalent modifications (e.g., DNA methylation), both to the DNA and histone protein organization in chromatin, act as a liaison between the inherited genotype and resulting phenotype.<sup>145,146</sup> Without diving into the genetic and epigenetic world, the local environment of the cell, or microenvironment, is the natural grounds for influencing cell fate, as seen in developmental biology.<sup>147</sup> It is the extracellular matrix

(ECM) of the cellular microenvironment that serves as a platform for mechanical and chemical cues, which can be created in vitro through 3D printing.

To facilitate tissue formation, alginates have been extensively utilized as bioink to provide a matrix scaffold to direct a specific 3D cell growth because it can robustly form cell-compatible hydrogels in physiological conditions. In addition, it can be modified for a variety of tissue engineering applications, including bone, vascular, and adipose tissue engineering.<sup>127,148-157</sup> However, native alginate is a bioinert material (i.e., lack of cell-adhesive moieties) with limited biodegradation.<sup>135,150,153</sup> Mooney and coworkers have shown that chemical modification of alginate through oxidation allows for controlled degradation.<sup>158-160</sup> Due to this desirable characteristic for tissue engineering applications, oxidized alginate holds great potential as ink for bioprinting. However, little previous research has explored the applications of oxidized alginates in bioprinting.

In this study, we prepared a library of 30 different alginate solutions with varied oxidation percentages and concentrations to develop a tunable bioink platform for bioprinting that can be modified for a wide range of tissue engineering applications. To this end, we have analyzed two key physical properties (i.e., viscosity and density) for the alginate solutions in the library and systematically investigated the effects of those physical properties of the alginates on their printability using a piston-driven, liquid-dispensing system and human adipose-derived stem cells (hADSCs). hADSCs were selected in this study because of their high proliferation rates, a persistent multipotency, and a well characterized morphology in 2D culture.<sup>161</sup> This has allowed for the

identification of a suitable range of material properties of alginates for bioink development. Further, the alginate-based bioinks were shown to be capable of modulating important stem cell behavior, such as proliferation and spreading, without affecting their printability and structural integrity after 8 days in cell culture (Fig. 1.1). The research reported here will accelerate the development of alginate-based bioink for tissue-specific tissue engineering applications.

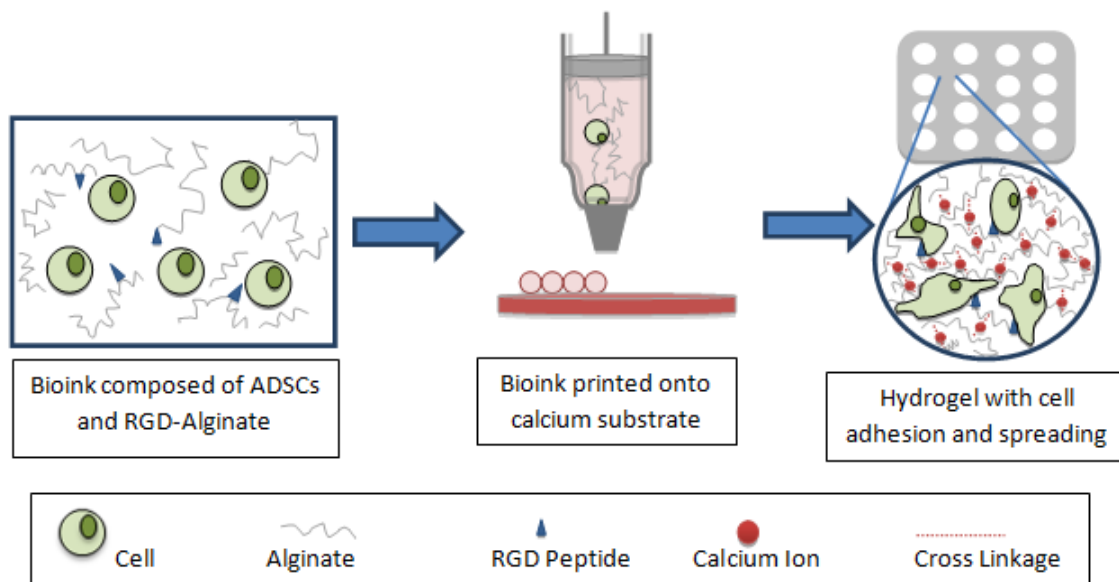


**Figure 1.1** Schematic representation of biodegradable oxidized alginate as bioink for bioprinting. A bioink consisting of RGD-modified oxidized alginate hADSCs was printed in a define lattice structure on a gelatin substrate to crosslink the hydrogel. The constructs were then evaluated over an 8-day period for cellular behavior (i.e., cell proliferation and spreading).

## Results and Discussion

Alginate has been widely used as a cell encapsulation material and in tissue engineering scaffolds.<sup>148,162</sup> However, native alginate is a bio-inert material with limited

biodegradation. To improve this, Mooney's group introduced a controllable degradation process using oxidized alginates reported in Bouhadir et al. 2001, which showed a promising capability as scaffold for tissue engineering applications.<sup>158,160,163</sup> These biodegradable alginates thus have great potential to develop a bioink platform for 3D bioprinting.

In 3D printing, there are multiple, unique dispensing systems to achieve high resolution, and each system has specific requirements for the optimal ink.<sup>164</sup> Among the various liquid-dispensing systems, piston-driven deposition has recently received significant attention because it offers a significantly high fabrication speed and is capable of fabricating anatomically shaped, clinically relevant-sized constructs.<sup>165,166</sup> They require a bioink with a suitable density and viscosity as well as the capability to retain printing fidelity and high cell viability post-printing.<sup>167</sup> In this study, we used a custom-made, piston-driven deposition system, as a test bed to examine the printability of biodegradable alginates. The printability here is defined as having high printing resolution and fidelity, a homogeneous cell distribution, and high cell viability post-printing. In addition, a lattice structure was utilized as our standard to evaluate printing resolution and fidelity in this study because it has been shown to promote cell viability and cell function (i.e. proliferation), offering the possibility of long-term culture *in vitro* without the assistance of a bioreactor.<sup>168</sup>

Initial efforts focused on the oxidized alginate previously utilized for tissue engineering applications, such as 5% ox.-2% conc. (i.e., alginate with 5% oxidation and 2% (w/w) concentration).<sup>158</sup> However, these alginate solutions did not provide sufficient printing resolution for a lattice structure due to its low viscosity (Fig. 1.3b, *top*). Also, alternating the oxidization percentage between 0% (non-degradable), 1%, 3%, 5%, and 10% proved to be inadequate to increase resolution for a 2% concentration solution. Meanwhile, other reported attempts to increase resolution while maintaining high cell viability in literature have used higher concentrations.<sup>168</sup> Therefore, a range of concentrations (2%, 5%, 8%, 10%, 15%, and 20%) mixed with different oxidation levels was designed to create a library composed of 30 different alginates (Fig. 1.2). Using the three criteria for printability evaluation (i.e., homogenous cell distribution, high printing

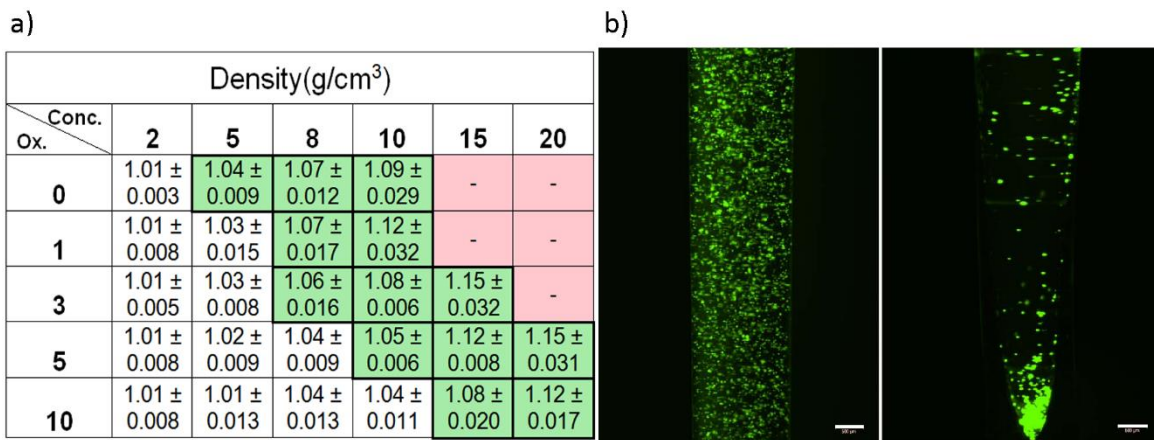


**Figure 1.2.** Density-based analysis on printability of different alginate solutions. (a) Density (mean ± SD) measurements of each sample with successful cell suspension results (green). Red denotes alginate compositions that did not completely dissolve into solution after 2 days. The other materials (white) were unable to maintain a homogenous cell distribution. (b) Calcein-stained hADSCs in the 5% ox.-10% conc. (left) and 5% ox.-2% conc. (right) material with and without successful cell suspension, respectively (scale bar= 500 μm).

resolution, and high cell viability post-printing)<sup>168-170</sup>, we systematically examined the material properties and printability of these alginates with hADSCs as a model cell line using a piston-driven, liquid-dispensing system.

**Density and cell suspension tests of different alginate solutions.** Homogeneity of cell distribution after printing is critical for the ideal bioink. To achieve a homogeneous cell suspension throughout the whole printing process, the density of the biomaterial should be close to or above that of the examined cell type.<sup>171</sup> By altering oxidation and concentration, a matrix of alginate densities was made (Fig. 1.2a). With increasing concentration and decreasing degree of oxidation, the densities of alginates showed an increasing trend. Given a printing operation time of 3 hours, we identified the range of materials that keep cells homogeneously distributed for printing with a piston-driven deposition system (Fig. 1.2a, *green*), which was verified by fluorescently labeled cell suspension tests (Fig. 1.2b). The results of this experiment and density measurements of all 30 materials confirm that a density around 1.05 g/cm<sup>3</sup> can maintain a homogeneous cell suspension for hADSCs. This is in agreement with the study by Lin and others that optimized a polyethylene glycol (PEG)-based hydrogel with 37.5% Percoll to attain the needed density to suspend hADSCs.<sup>171</sup> Density, thus, can define a limit for bioprinting alginate solutions. The individual cell density and biomaterial density must be taken into account when applying a density-based selection to other systems. It is important to note that a wider range of densities around 1.05 g/cm<sup>3</sup> can maintain a hADSC suspension within

a 3 hour printing process time without significant cell movement, due to the relatively high viscosity that slows the process of cell movement.

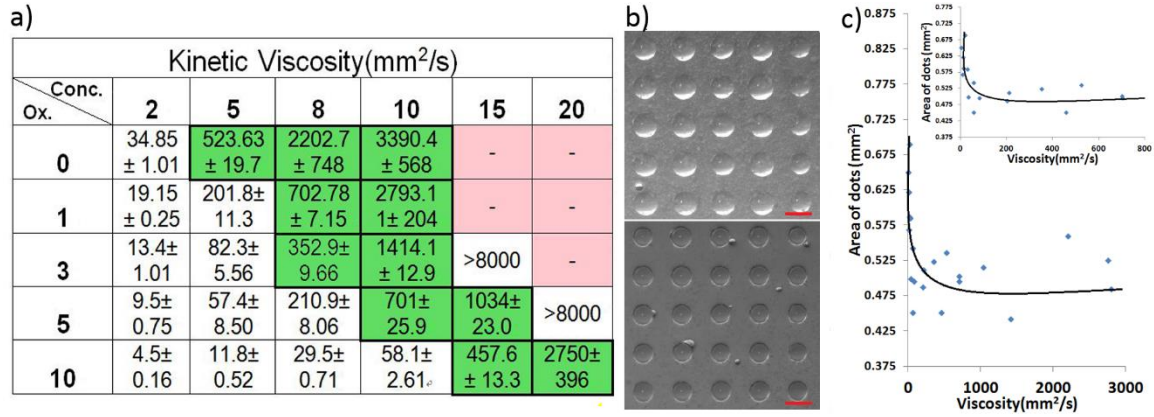


**Figure 1.3.** Viscosity-based analysis on printability of different alginate solutions. (a) Viscosity values of various alginate solutions with a range of concentrations and oxidation levels that passed the density requirement shown with a favorable area for higher resolution bioprinting with hADSCs (green). Red denotes alginate compositions that did not completely dissolved into solution after 2 days. The other materials were either too viscous to prepare for printing or failed the density test (white). (b) Using dots as the functional unit of liquid-dispensing strategies and a representation of resolution, a printed dot array (5×5) shows examples of low printing resolution (top), high printing resolution (low) (scale bar= 1 mm). (c) A plot of areas of dots versus viscosity shows a direct relationship between printability and viscosity of alginate samples. Guiding lines represent general flow of data.

**Viscosities of 30 different alginate solutions.** Given that viscosity plays an important role in a liquid-dispensing printer<sup>164</sup>, its effects on printability (i.e., printing resolution) were examined to determine a viscosity-based range for oxidized alginate ink. We found that altering oxidation and concentration resulted in a practical method of controlling the viscosity of degradable alginates. A similar pattern to the density measurements was observed: as the concentration increased or the degree of oxidation decreased, the viscosity showed an increasing trend (Fig. 1.3a). In addition, we have



printed 5×5 arrays of dots using different biodegradable alginates to examine the effect of viscosity on dot fidelity and size, which determines printing resolution. As shown in Figure 1.3b and Figure 1.3c, there is an optimal range of viscosity (i.e., ~200 mm<sup>2</sup>/s to ~3000 mm<sup>2</sup>/s) for the improved printing resolution independent of concentration and oxidation degree of alginate solution. This indicates the critical role of viscosity in printing resolution for a piston-driven, liquid-dispensing system. At the low viscosity end (i.e., <200 mm<sup>2</sup>/s), low concentration alginates produced larger dots when compared with alginates within the optimal range of viscosities (Fig. 1.3c). On the other hand, an upper threshold (i.e., >3000 mm<sup>2</sup>/s) also exists due to the increased liquid handling difficulty after a certain viscosity value (Fig. 1.3c). It is known that high viscosity can alter liquid-dispensing characteristics of the solution. For example, Schuurman and coworkers reported that high viscosity materials can form filaments rather than droplets when depositing.<sup>172</sup> Notably, alginate solutions with viscosities between ~200 mm<sup>2</sup>/s and ~400 mm<sup>2</sup>/s typically had densities lower than the threshold necessary for maintaining homogenous cell suspension (i.e., <1.05g/mL). The viscosity range suitable for high printability was therefore refined to ~400 mm<sup>2</sup>/s to ~3000 mm<sup>2</sup>/s. The alginate solutions within the optimal range of viscosity are highlighted in green in Figure 1.3a. The data presented in Figure 1.3a will enhance the available viscosity data on alginates used in other bioink development research with liquid-dispensing systems.<sup>173-175</sup>

**hADSC viability in the printed alginate.** Cell viability, as one of the standards of biocompatibility for bioink, was analyzed after printing.<sup>170</sup> To examine the effect of

printing on cells, viabilities were assayed immediately following the printing process (Figs. 1.4a and 1.4b). A compromised cell viability (<90%) was found in the high viscosity alginates (>3000 mm<sup>2</sup>/s), while high cell viability (>90%) was found in the alginate solutions with the optimal/medium viscosity (~400 mm<sup>2</sup>/s to ~3000 mm<sup>2</sup>/s). The decreased cell viability in the high viscosity alginate samples was attributed to the limited

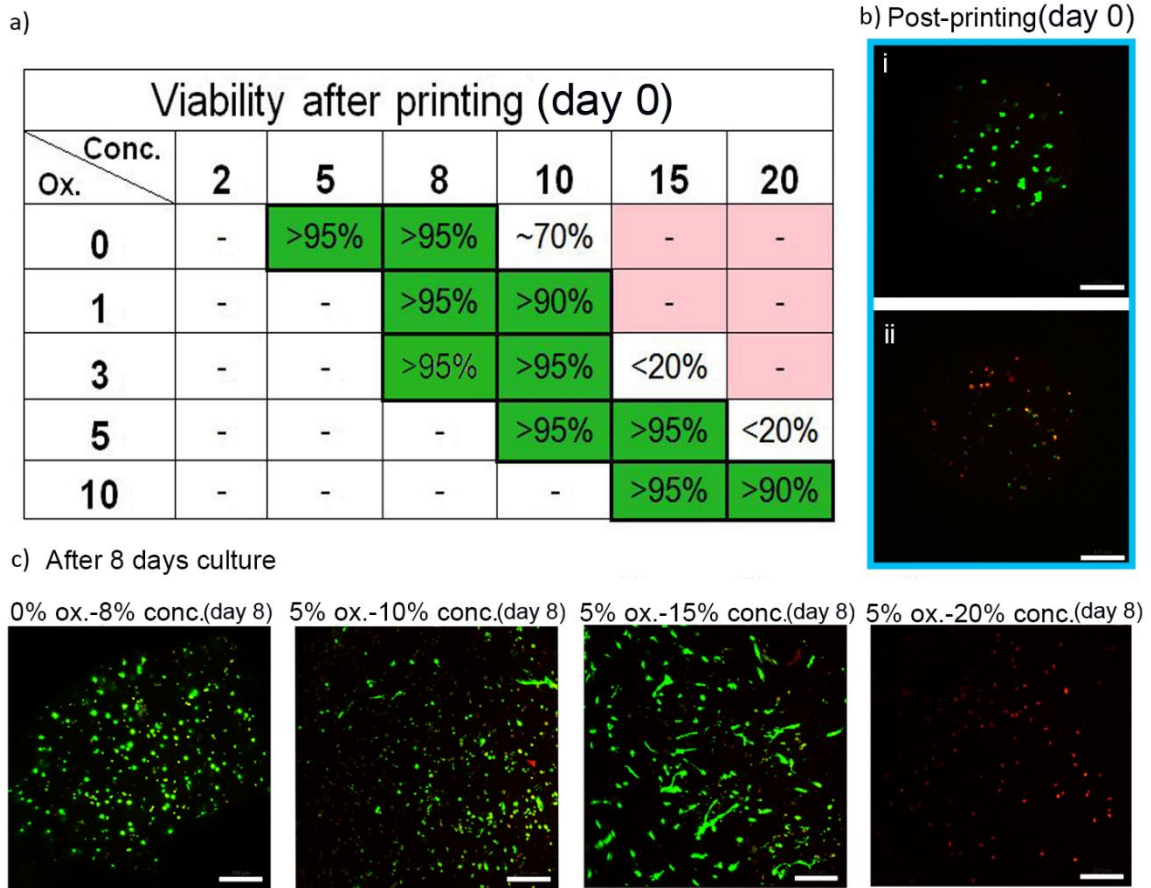


**Figure 1.4.** Cell viability assay of density and viscosity criterion-filtered samples. (a) Samples of high viability (>90%) right after printing (green). (b) The fluorescent pictures of live-dead assay after printing: (i) high cell viability sample (e.g. 5% ox.-15% conc.) and (ii) low cell viability sample (e.g. 5% ox.-20% conc.) (scale bar= 100 μm). (c) Cell viability assay at day 8. Except the 5% ox.-20% conc. sample (0% viability), the remaining four samples showed high viabilities (>95%) after 8 days in culture (scale bar= 100 μm).

nutrient transport (i.e., diffusivity). Viability assays were performed again after 8 days in cell culture, as shown in Figure 1.4c. The alginates with optimal/medium viscosity (i.e.,  $\sim 400 \text{ mm}^2/\text{s}$  to  $\sim 3000 \text{ mm}^2/\text{s}$ ) again exhibited high viability ( $>90\%$ ), whereas the alginates with high viscosity showed a negligible viability (0%). The results indicate that alginates with high viscosity, although printable, may create an environment with poor nutrient transport, resulting in compromised cell viability, in accordance with previous studies.<sup>176,177</sup> Given the importance of maintaining high cell viability post-printing, it is a key parameter to include when defining the range of engineered alginates for bioink.

**Summary of the oxidized alginates based on three printability criteria.** The capacity to maintain homogenous cell suspension (influenced by the densities of alginates samples) and achieving high printing resolution and viability (both influenced by the viscosities of samples) are the three criteria for our bioink selection. Based on these criteria, a new table was assembled to highlight the printable alginate solutions (Fig. 1.5). It is important to note that these highlighted alginates can serve as base materials to

Oxidized alginate bioink selection <sup>o</sup>						
Conc. Ox.	2	5	8	10	15	20
0	-	+	+	-	-	-
1	-	-	+	+	-	-
3	-	-	+	+	-	-
5	-	-	-	+	+	-
10	-	-	-	-	+	+

**Figure 1.5.** Summary table of the preferable range of alginate samples with high printability (green) based on the three established printability criteria (i.e., homogeneous cell suspension, high printing resolution, and high cell viability).

develop bioinks with desired physical/chemical/biological properties for tissue-specific tissue engineering applications.<sup>160</sup> Further, the density, viscosity, and viability analysis allowed for the identification of a suitable range of material properties of alginate solutions to be applied to bioprinting. This can provide a guideline for developing next generation of alginate-based bioink for 3D bioprinting-facilitated tissue engineering. Notably, Mooney and coworkers have demonstrated the independent control of elastic moduli and degradation rates of alginate hydrogels by creating binary alginate hydrogels.<sup>178</sup>

**Printing lattice-structured, cell-laden alginate hydrogels and cell culture.** Lattice structures have been shown to support higher cell viability and proliferation rate because they offer a conducive environment for nutrient supply and waste excretion.<sup>168</sup> In this study, we designed a point-to-point protocol to produce cell-laden hydrogels with a lattice structure of 7 columns and 7 rows. They have optimal expected dimensions of 12.6 mm x 12.6 mm (X, Y) based on a printing design dimension of 12 mm × 12 mm (from the center of dot placement) and a Z dimension limited to one layer (Fig. 1.6a). To examine the effects of the biodegradability of oxidized alginate, we selected samples with

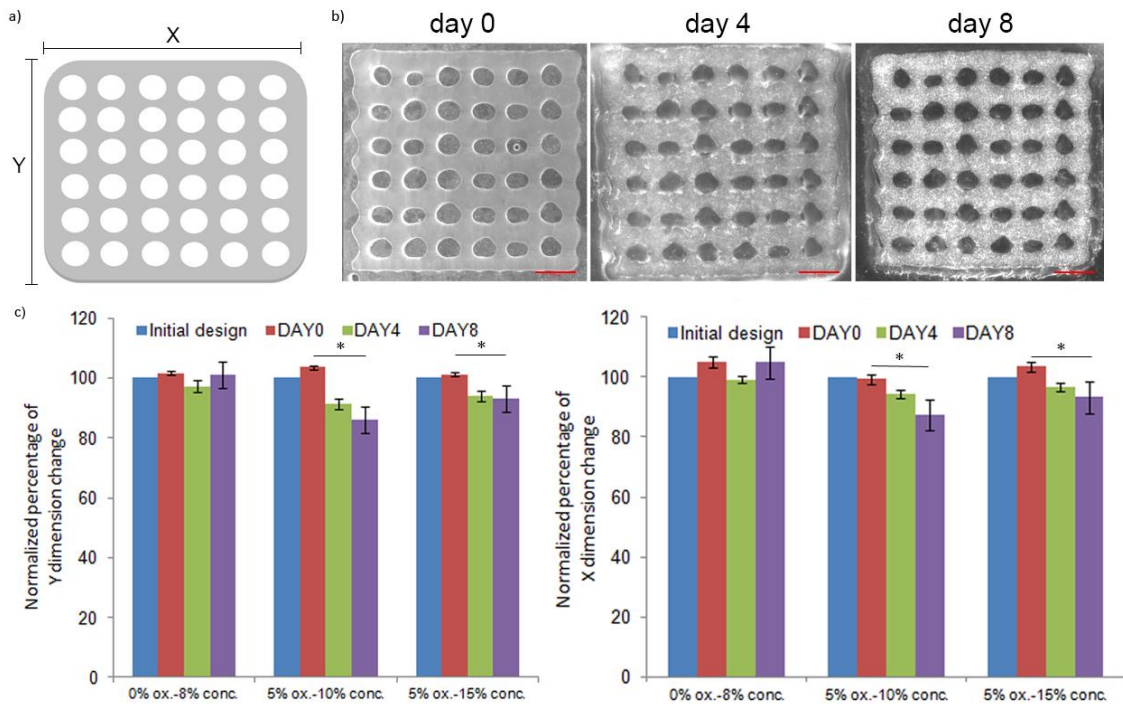


**Figure 1.6.** Lattice structures printed with bioprinting-compatible materials and their dimensional change in 8 days. (a) Initial design of lattice structure. (b) Pictures of printed lattice structures (5% ox.-10% conc. sample) at day 0, day 4, day 8 shows printed structures highly matched the initial design with apparent dimensional changes after 8 days in culture (scale bar= 2 mm). (c) Normalized comparison between the initial design (12.6 mm x 12.6 mm) and the X and Y dimensions of the lattice structures (0% ox.-8% conc., 5% ox.-10% conc., 5% ox.-15% conc. ) after 8 days in culture. All values are mean  $\pm$  SD. Asterisk denotes significant difference between day 0 and day 8.

low degradable (0% ox.), medium degradable (5% ox.), and high degradable (10% ox.) characteristics. The density, viscosity, and viability analysis allow for the selection of the appropriate concentrations for each alginate sample (0% ox.-8% conc., 5% ox. -10% conc., 5% ox.-15% conc., 10% ox.-15% conc.) to be printed with suspended hADSCs. Although these four materials have significant differences in their physical properties (i.e., density and viscosity) (Figs. 1.2 and 1.3), they all can be successfully printed into lattice-structured, cell-laden hydrogels with homogeneous cell distribution (Figs. 1.6 and 1.7a).

Notably, the dimensions of all the printed lattice structures were within 10% of the optimal expected dimensions (i.e., 12.6 mm x 12.6 mm) (Fig. 1.6c), which can be defined as accurately printed structures.<sup>179</sup>

All lattice structures were cultured for 8 days. For the samples that maintained measurable structures, the changes in length and width were measured at day 0, day 4, and day 8, and the extent of dimensional changes were determined (Fig. 1.6c). The 0% ox.-8% conc., 5% ox.-10% conc., and 5% ox.-15% conc. samples remained intact through 8 days in culture, and the rapid degradation of 10% ox.-15% conc. alginate resulted in almost complete fracture of the structure by day 8.<sup>158</sup> Further, no significant change in dimension (Y dimension,  $p=0.10$ ; X dimension,  $p=0.27$ ) was observed in the 0% ox.-8% conc. sample from day 0 to day 8 (Fig. 1.6c), whereas a significant dimensional decrease (Y dimension,  $p<0.05$ ; X dimension,  $p<0.05$ ) was observed in the 5% ox.-10% conc. and the 5% ox.-15% conc. samples from day 0 to day 8. The decrease in dimension of the oxidized alginate samples was attributed to their biodegradation and cell activities. This consistent decrease should be considered, especially for dimension-specific designs when using dynamic or prolonged culture methods.

**hADSC spreading and proliferation assays in printed lattice structures.** In addition to maintaining cell viability, a bioink platform should allow for the modulation of cell behaviors. In this study, proliferation and spreading of hADSCs were examined due to their important roles in tissue engineering applications. In particular, cell spreading can be used to modulate self-renewal and differentiation of hADSCs.<sup>180-182</sup> Cell-adhesive RGD

peptide, a widely known cell attachment promoter molecule<sup>150,183-185</sup>, was conjugated to alginate bioink in this study to promote cell proliferation and spreading (Fig. 1.9). DAPI staining for nuclei and phalloidin staining for actin were used to characterize the cell behavior in each structure (Fig. 1.7a). As shown in Figure 1.7a, 1.7b, and 1.7c, the oxidized

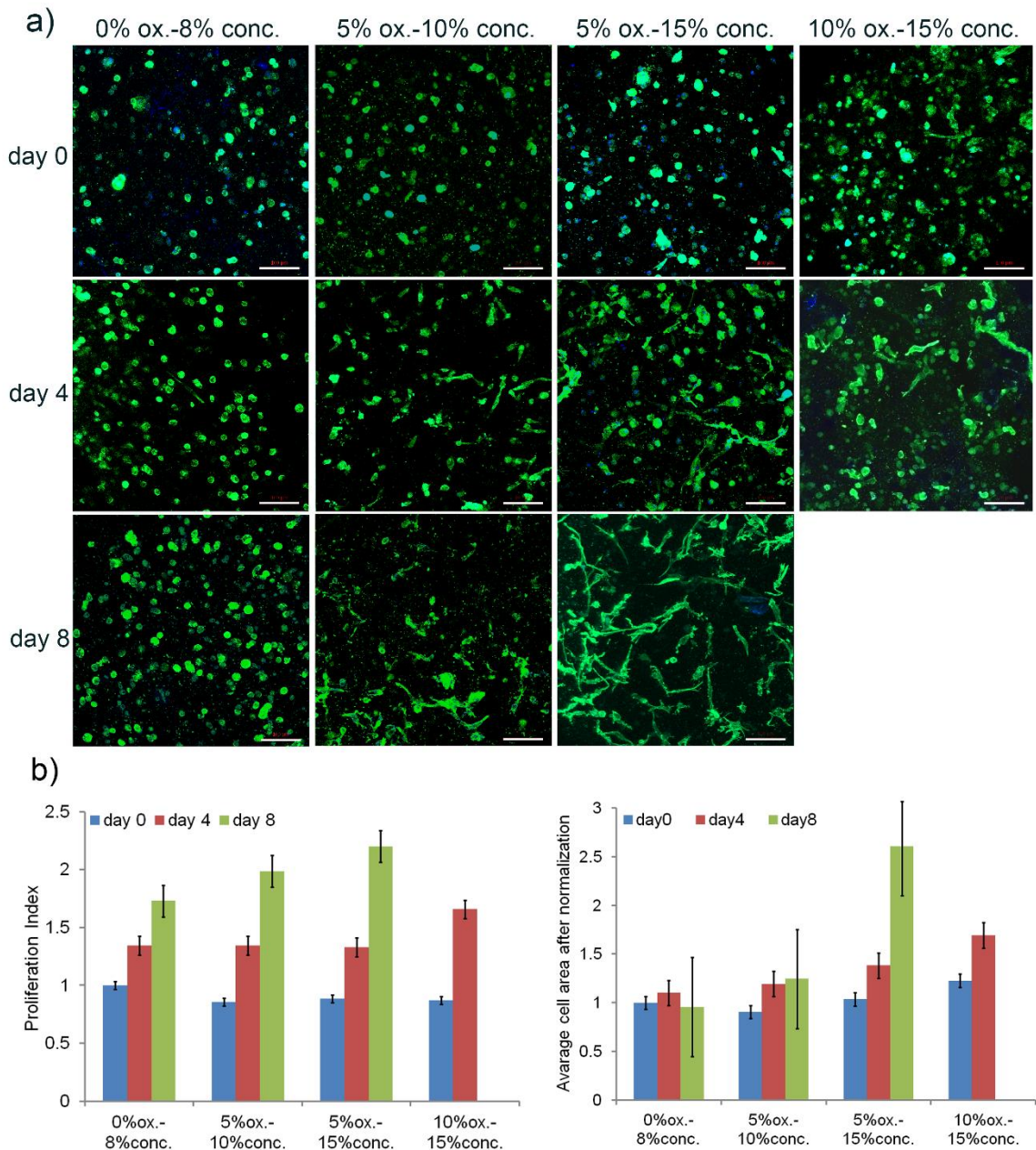




**Figure 1.7** (previous page). hADSC behavior in the lattice structures. (a) Cell spreading with fluorescent staining (phalloidin) for actin at day 0, 4, and 8 (scale bar= 100  $\mu$ m). (b) hADSC proliferation index and spreading assays based on fluorescent staining (phalloidin and DAPI stain) at day 8. Proliferation index was calculated as the cell number of each day divided by the original cell number on day 0 for the 0% ox.-8% conc. alginate sample for relative comparison. Cell area was calculated as total cell area divided by the number of cells normalized over the values at day 0 for the 0% ox.-8% conc. alginate sample. All values are mean  $\pm$  SD.

alginate bioinks (i.e., 5% ox.-10% conc., 5% ox.-15% conc., and 10% ox.-15% conc. samples) can effectively promote cell proliferation and spreading when compared to the non-oxidized alginate bioink (i.e., 0% ox.-8% conc. alginate). Quantitatively, the cell proliferation percentages after 8 days in culture were 173% for the 0% ox.-8% conc. alginate, 232% for the 5% ox.-10% conc. alginate, 248% for the 5% ox.-15% conc. alginate (Fig. 1.7b), and 190% for the 10% ox.-15% conc. alginate at day 4. For cell spreading, the average cell size did not change significantly after 8 days in culture for the 0% ox.-8% conc. alginate, while cell size increased 25% for the 5% ox.-10% conc. alginate, 161% for the 5% ox.-15% conc. alginate at day 8, and 69% for the 10% ox.-15% conc. alginate at day 4 (Fig. 1.7c). The low cell proliferation and cell spreading in the 0% ox.-8% conc. alginate assumed to be attributed to its persistent low porosity given its limited degradability. In contrast, the significant increase in cell proliferation and spreading in the 5% ox.-15% conc. alginate was assumed to be attributed to the increasing porosity associated with its degradation. The vast difference in cell spreading among alginate bioinks with varied oxidation degree and concentration (i.e., 0% ox.-8% conc., 5% ox.-10% conc., and 5% ox.-15% conc. samples) demonstrates their great potential in printing scaffolds tailored for specific tissue engineering applications. For example, the 0% ox.-8% conc. alginate



induced a round cell morphology that can be applied to chondrogenesis, while the 5% ox.-15% conc. alginate was associated with an increased spreading phenotype that could facilitate osteogenesis.<sup>186-191</sup> In addition, the cell-matrix-interactions between hADSCs and alginates were investigated using  $\alpha_v\beta_3$  integrin immunofluorescent staining as shown in Figure 1.10. The RGD conjugation was found to promote integrin expression at all three dates (i.e., day 0, day 4 and day 8). Interestingly, the  $\alpha_v\beta_3$  integrin expression was found on day 8 for alginate samples without RGD conjugation, which was attributed to the ECM secreted by hADSCs, consistent with previous research.<sup>192</sup>

Figure 1.8 is a 3D picture showing a portion of a lattice structure from the 5% ox.-15% conc. oxidized alginate with hADSCs after 8 days in culture. The distribution of the observed spreading cells confirmed that the homogenous cell distribution in the alginate-based bioink pre-printing was maintained in the lattice structure after 8 days in cell culture. Summarizing the results shown in Figure 1.6 and Figure 1.7, the alginate-based bioinks are capable of modulating hADSC proliferation and spreading without affecting

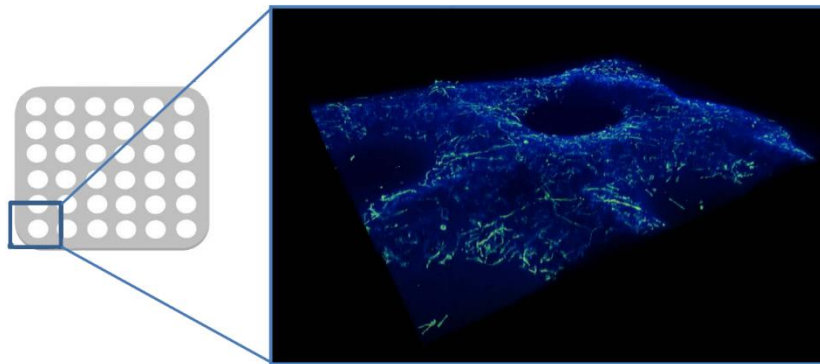


**Figure 1.8.** A computer-rendered 3D picture of a portion of the printed lattice structure made by the best supporting hADSC material, 5% ox.-15% conc. oxidized alginate, showing multiple layers of spreading cells within the hydrogel.

structural integrity after 8 days in culture, apart from the highly degradable alginate sample, 10% ox.-15% conc. This creates a solid foundation for the development of alginate-based bioink for 3D bioprinting-tailored tissue engineering scaffolds.

## **Conclusion**

The primary characteristics influencing the printability of oxidized alginate as ink for bioprinting was defined by its ability to hold a homogeneous cell suspension, have high printing resolution, and support high cell viability. According to these factors, an ideal printable range for using oxidized alginate as a bioink platform was established. Further, by mimicking the adhesive cues (i.e., RGD) present in ECM, these alginate-based bioinks were shown to be capable of modulating hADSC functions without affecting their printability and structure integrity after cell culture. The introduction of oxidized alginate to bioprinting has led to the creation of a tunable bioink platform for a range of tissue fabrications. Based on our findings, the observed functional relationship between the material properties (i.e., viscosity and density) of alginate and its printability allows for an enhanced progression in alginate bioink development for liquid-dispensing printing. When using other cell types, metabolic demands may require an altered density and viscosity of oxidized alginate to allow for optimal diffusion of nutrients. Apart from diffusion limitations, the  $\text{Ca}^{2+}$  concentration used in the gelation process may also affect  $\text{Ca}^{2+}$ -sensitive cell types, such as chondrocytes.<sup>193</sup> This  $\text{Ca}^{2+}$  concentration can be adjusted to achieve higher viability, though a prolonged gelation time may affect the printing

fidelity and total printing time.<sup>194</sup> Future studies in bioprinting technology and a widened understanding of self-assembly mechanisms between cells may reshape the demands for ink printability.

## **Materials and Methods**

*Materials.* Sodium alginate was purchased from FMC BioPolymer (Philadelphia, PA). Ethylene glycol was purchased from Mallinckrodt Baker, Inc. (Phillipsburg, NJ). All other chemicals used for this study were purchased from Sigma-Aldrich (St. Louis, MO) unless otherwise stated.

*Alginate synthesis and oxidation.* Sodium alginate was prepared using the method established by Bouhadir and others.<sup>158</sup> Briefly, 1 g sodium alginate was dissolved in 100 mL of distilled water. Sodium periodate was used as the oxidizing reagent and was added at room temperature in varying quantities, based on the desired percent oxidation (at oxidation percentage of 1%, 3%, 5%, 10%, w/w). The reaction was terminated by the addition of ethylene glycol after 24 hours. Sodium chloride (3 g) was then dissolved in the solution. Excess amount of ethyl alcohol was added to the solution (2:1 ratio), precipitating the oxidized alginates. The solution was centrifuged to collect the precipitates, and the ethanol wash was repeated. The oxidized alginate pellets were then lyophilized and stored at -20°C.

*RGD-alginate conjugation.* To promote cell attachment and spreading, RGD peptides have been conjugated into oxidized alginates using a similar method as

Mooney's group, reported in Rowley et al. 1999: utilizing aqueous carbodiimide chemistry with G<sub>4</sub>RGDSP-OH (International Peptides, Louisville, KY).<sup>150</sup> The final modification percentage of RGD to alginate was 1% (w/w).

*Identification of viscosity and density.* Aqueous alginate solutions (at oxidation percentage of 0%, 1%, 3%, 5%, 10% w/w) of varying concentration (2%, 5%, 8%, 10%, 15%, 20% w/w) were made using a weight to total-weight ratio. To test viscosity, approximately 8 mL of varying alginate solutions were made and tested three times by Cannon-Fenske Opaque Calibrated viscometers (Cannon® Instrument Company, Inc, USA) at 40 °C. Viscosity values were calculated according to Poiseuille's law associated with the calibrated viscometers and then converted to kinematic viscosities by dividing by density. The density of the alginate solutions were calculated by measuring the mass of 1 mL of alginate aqueous solution three times and then averaged.

*Preparation of Ca<sup>2+</sup>-containing gelatin substrate for 3D-printing alginate hydrogels.* To avoid reduced viability with high Ca<sup>2+</sup> concentration solutions, a calcium substrate was prepared for alginate, as done previously.<sup>194</sup> Briefly, a 100 mM CaCl<sub>2</sub> gelatin solution was prepared by combining calcium chloride dehydrate, sodium chloride (0.9 wt%), and porcine gelatin (2 wt%) in distilled water and boiled for 2 minutes. Aliquots of 5 mL of gelatin were put into standard petri dishes to gel in a refrigerator overnight. Titanium dioxide (0.3% wt%) was added to the same solution and stirred for 10 min to increase the opacity of the resulting surface. 3 mL of the gelatin/TiO<sub>2</sub> mixture was spread

evenly across the surface of the previously prepared gelatin plates and put in the refrigerator overnight to be used within 3 days.

*Printing process of alginate hydrogels.* Aqueous alginate samples were prepared according to a weight to total-weight ratio using either distilled water (for density and viscosity tests) or cell medium (for dot analysis and cell studies) using the same preparation protocol. The bioink (with cells for cell study) were then loaded into a printer-compatible syringe. All printing was performed on the Palmetto Printer, a custom-made, piston-driven deposition system, on a temperature-controlled plate at 4 °C. Droplet volume was maintained at 230 nL with a dispensing speed of 10  $\mu$ L/sec.

For dot analysis, a 5×5 dot array was printed for each sample and left to gel for 40 min before macroscopic imaging with the Olympus SZX16 stereomicroscope.

For lattice structure fabrication, single layer, cell-laden, lattice structures were printed with 7 columns and 7 rows using a point-to-point strategy to print every other dot with optimal expected dimensions of 12.6 mm x 12.6 mm (X, Y), which is a result of a printing design with dimensions of 12 mm x 12 mm (from the center of dot placement) (Fig. 1.3a). In liquid-dispensing printing, the point-to-point method allows for accurate control of design-specific structures. The bioink used for the structures were alginate solutions of 0% ox.-8% conc., 5% ox.-10% conc., 5% ox.-15% conc., 5% ox.-20% conc., 10% ox.-15% conc. Following printing, 8 mL of media was added to the gelatin plate and put in the incubator for approximately 30 min, melting the Ca<sup>2+</sup>-containing gelatin to maximize alginate crosslinking. Lattice structures were then transferred to individual wells in a 6-

well plate for extended culture. Macroscopic pictures were taken with the Olympus SZX16 stereomicroscope, and media was changed every 4 days for 8 days.

*Cell culture and cell behavior studies.* Human adipose-derived stem cells (hADSC) (Lonza, Basel, Switzerland) were used to investigate the effects of the alginate gel's oxidation and concentration on cell viability, attachment, and proliferation. The cells were cultured in low glucose DMEM with 10% FBS and 1% penicillin-streptomycin, 1% glutamine, and 1% antimycin (Gibco Life Technologies, Grand Island, NY). At >80% confluency, cells were detached using tryPLE Express (Gibco Life Technologies) and passaged. All experiments were conducted using passage 5 (P5) hADSCs. Aqueous alginate solutions of varying oxidation and concentration were prepared using the cell culture medium and mixed with detached cells at a concentration of 1.3 million cells per mL. The samples were loaded into printer syringes, transported to the printer, and then printed as described in the previous section.

hADSC suspension tests were performed by mixing aqueous alginate samples (made with media) of varying concentrations with live cells (1 mL of 1.3 million cells per mL) labeled with Calcein, AM (Gibco Life Technologies). The samples were loaded into NMR tubes and were left stationary for 3 hours. Then, each solution was partitioned from top to bottom into 5 parts, and the number of cells in each part was counted microscopically and analyzed. The macroscopic images were taken with the Olympus SZX16 stereomicroscope.

The cell-seeded hydrogels were assessed for cell viability post-printing using the live/dead cell viability assay kit from Invitrogen Life Technologies (Grand Island, NY) following the protocol of the kit. The cell viability percentage was calculated as the number of live cells (green-stained) over the total number of cells (green and red). Viability assays were performed for the printed structures again after 8 days of culture using portions of each structure. High viscosity samples of each oxidation (0% ox.-10% conc., 1% ox.-10% conc., 3% ox.-15% conc., 10% ox.-20% conc.) were later tested using the same post-printing method. All the fluorescent pictures were taken by Leica TCS SP5 AOBS Confocal Microscope System.

The lattice structures of five samples (0% ox.-8% conc., 5% ox.-10% conc., 5% ox.-15% conc., 5% ox.-20% conc., 10% ox.-15% conc.) were printed with hADSCs following the protocol above. Cell proliferation and morphology for these samples were assessed at day 0, day 4, and day 8 using portions of each structure with a fluorescent DAPI and phalloidin staining kit from Invitrogen Life Technologies (Grand Island, NY) by following the kit protocol. For cell proliferation analysis, the following cell counting method was utilized on each of the given days. At least 3 different pictures (600  $\mu\text{m}$  x 600  $\mu\text{m}$ , z-layer thickness  $\approx$  100  $\mu\text{m}$ ) were taken of the respective hydrogel samples, and the cell number in 3 random areas (200  $\mu\text{m}$  x 200  $\mu\text{m}$ , >10 cells/area) of each picture were manually counted based on DAPI and phalloidin staining. Proliferation index was calculated as the cell number of each day of each sample divided by the original cell number on day 0 for the 0% ox.-8% conc. alginate sample. For cell morphology, fluorescent images of each sample

(at least 4 random pictures per sample, 600  $\mu\text{m}$  x 600  $\mu\text{m}$  per picture) were taken by the Leica TCS SP5 AOBS Confocal Microscope System using Z-stack parameters of 30 optical slices over a 300  $\mu\text{m}$  depth. Cell sizes were measured through ImageJ threshold-based edge detection tools as a total cell area divided by the number of cells normalized over the values at day 0 for the 0% ox.-8% conc. alginate sample (Fig. 1.4c). The cell-matrix interactions between hADSCs and alginates were studied using mouse primary antibody for  $\alpha_v\beta_3$  integrin (Abcam, Cambridge, MA) and rat (anti-mouse) secondary antibody, Alexa Fluor 546 (Invitrogen, Carlsbad, CA), both at 1:200 ratio.

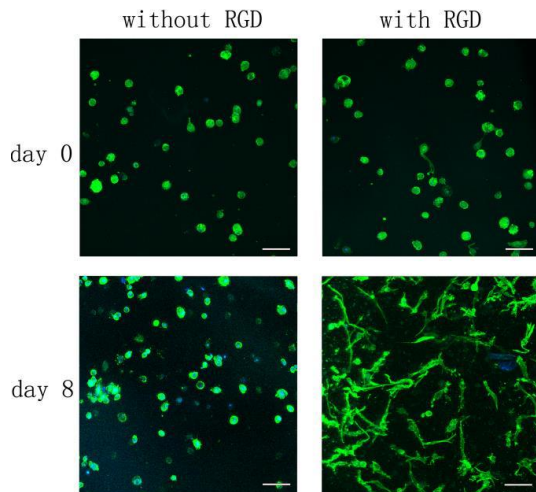
*Rebuilt 3D image for printed lattice structure.* The cells in the printed lattice structure were stained with fluorescently labeled phalloidin and imaged by Leica TCS SP5 AOBS Confocal Microscope System. These images were rebuilt into a 3D rendering using Amira software.

*Statistical analysis.* The results were expressed as the mean  $\pm$  standard deviation (SD) and analyzed using JMP 11 and Excel statistical software. Lattice dimensions were compared between day 0, day 4, and day 8 by a Student's *t*-test. Dot analysis, viscosities, and densities were analyzed separately using unpaired Student's *t*-tests. A confidence interval of 95% was used.



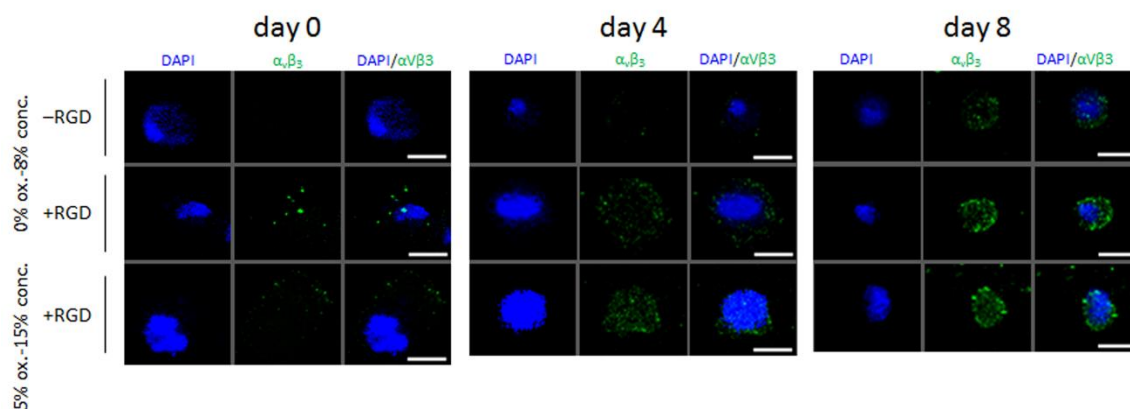
## Supporting Information

Figure 1.9



**Figure 1.9.** A proof-of-concept analysis of the necessity of 1% (w/w) RGD peptide-conjugated alginate for changing cell function. In 5% ox.-10% conc. alginate hydrogel, hADSCs exhibited higher spreading after 8 days of culture. Scale bar = 100  $\mu\text{m}$ .

Figure 1.10



**Figure 1.10.**  $\alpha_v\beta_3$  integrin expression of hADSCs in alginate hydrogels with and without RGD conjugation at day 0, day 4, and day 8. Samples include 0% ox.-8% conc. without RGD conjugation, 0% ox.-8% conc. with RGD conjugation, and 5% ox.-15% conc. with RGD conjugation oxidized alginates. Blue – DAPI nuclear stain; Green –  $\alpha_v\beta_3$  integrin (scale bars= 15  $\mu\text{m}$ ).

Table 1.1.

Viability of the alginate samples at day 0, day 4, and day 8.

Sample name Time point	0% ox.- 8% conc.	5% ox.- 10% conc.	5% ox.- 15% conc.	5% ox.- 20% conc.	10% ox.- 15% conc.
Day 0	96%	98%	98%	19%	96%
Day 4	93%	92%	96%	3%	92%
Day 8	92%	90%	95%	0%	-

## CHAPTER THREE

### NANOENGINEERED SOLUTIONS TO FACILITATE HUMAN CARDIAC MICROTISSUE DEVELOPMENT

#### Introduction

While biomaterials can provide molecular/mechanical signals to promote cell adhesion, proliferation, and enhance extracellular matrix (i.e., ECM) protein deposition and tissue formation<sup>195,196</sup>, scaffold-based approach faces numerous challenges. Apart from potential biocompatibility issues, one of the key challenges of using engineered biomaterials (e.g., functionalized alginate) is that identification of the ideal material depends on a sufficient understanding of the role of targeted processes in directing cell behavior.<sup>197</sup> In the context of cardiac embryonic development, environmental factors (e.g., extracellular matrix, growth factors, mechanical and electrical stimulation) have major effects on the maturation of cardiomyocytes. To mimic the maturation process *in vitro*, stem cell-derived cardiomyocytes have been mixed with scaffolding materials (e.g., Matrigel and collagen type I gel) to prepare cardiac tissue-engineered constructs and then conditioned with electrical and/or mechanical stimulation.<sup>21,25-27</sup> While these scaffolds can provide tissue-like 3D microenvironments, current scaffolding materials lack the matched physical/chemical/biological properties with the native extracellular environments during heart development. On the other hand, scaffold-free, 3D cardiac spherical microtissues (i.e., spheroids) have emerged as promising model systems to

mimic cardiac tissues by leveraging the ability of cells to self-assemble into microtissues at a high cell density with endogenous ECM production.<sup>28,29</sup>

As physiological cardiac microtissue maturation depends on synchronized contractile activity, we previously developed a method to incorporate a trace amount of electrically conductive silicon nanowires (e-SiNWs) into otherwise scaffold-free, human induced pluripotent stem cell-derived cardiomyocyte (hiPSC-CM) spheroids that significantly advanced the structural and contractile maturation of the cardiomyocytes across a range of viable sizes.<sup>45,198</sup> This approach has a distinct advantage of only using a minimal amount of e-SiNWs (0.004% w/v), minimizing the adverse effects of traditional scaffolds, such as the unmatched physical/chemical/biological properties with the native extracellular environments during heart development. e-SiNWs were selected because of their controllable electrical conductivity, tunable dimensions, and convenient surface tailorability.<sup>199,200</sup> In this study, n-type SiNWs (Diameter  $\approx$  100 nm; length  $\approx$  10  $\mu$ m; Silane/Phosphane = 500) were prepared according to the previously established protocol<sup>201</sup> to obtain a high conductivity (150 - 500  $\mu$ S/ $\mu$ m) and to avoid cell internalization.<sup>44,202</sup> Although SiNWs might not be well known as biocompatible materials, *in vitro* biocompatibility studies have shown no significant cytotoxic effects for both undoped and n-type SiNWs<sup>203,204</sup>. Further, the recent research showed SiNWs are biodegradable, and their degradation products are found mainly in the form of Si(OH)<sub>4</sub> and are metabolically tolerant *in vivo*<sup>205-209</sup>. This makes them advantageous over other non-biodegradable, electrically conductive nanomaterials (e.g., gold nanowires, carbon

nanotubes and nanofibers), especially for potential *in vivo* applications. We reasoned that the incorporation of e-SiNWs in cardiac spheroids facilitated the formation of an electrically conductive network, and provided synchronized and improved electrical/mechanical signals to advance structural and contractile maturation of the cardiomyocytes.

While nanowired spheroid culture of hiPSC-CM significantly improved the contractile development, extended culture did not further improve cardiac maturation.<sup>45</sup> Enhanced maturation of hiPSC-CMs *in vitro* is a critical barrier for understanding the translational potential of patient-specific hiPSC-CMs for drug screening and/or cell therapy strategies to repair the damaged heart. To derive hiPSC-CMs suitable for cell transplantation, various tissue-engineering strategies have been utilized to mimic adult host ventricular myocardium to accelerate phenotypic development of hiPSC-CMs.<sup>21,30-36</sup> Particularly, several groups have used electrical stimulation as an exogenous approach to recapitulate the natural pacemaker-initiated excitation of cardiomyocyte contraction to advance the function of hESC/hiPSC-CMs.<sup>21,35,37-42</sup>

We reasoned that exogenous electrical stimulation could synergize with the endogenous benefits of nanowired spheroids to improve the functional development of hiPSC-CMs in cardiac spheroids. To this end, we developed a viable strategy to electrically stimulate nanowired hiPSC cardiac spheroids and examined the effects of electrical stimulation and silicon nanowires on the functions of spheroids. Herein, for the first time, we show that the synergy of exogenous electrical stimulation and nanowires to hiPSC

cardiac spheroids 1) enhanced microtissue development through formation of functional cell-cell junctions, 2) improved development of contractile properties of hiPSC-CMs, and 3) decreased the endogenous spontaneous beat rate for reduced arrhythmogenic potential. Through tissue- and cell-level examination of cardiac spheroids, the progress here contributes to the fundamental understanding of hiPSC cardiac microtissue development and addresses the need for an advanced, functional cardiac cell therapy vehicle for future cardiac tissue repair.

## Results and Discussion

**Development of electrically stimulated, nanowired hiPSC-CM spheroids.** In the adult heart, ventricular cardiomyocytes contract regularly due to the depolarizing electrical propagation originating in the sino-atrial node of the heart. To mimic this stimulation for contraction, cardiac tissue engineering strategies have utilized electrical pacing to develop and maintain cardiomyocyte function.<sup>35,38,39,41,210-212</sup> During our previous development of nanowired cardiac spheroids, electrical stimulation (3.75 V/cm, 1 Hz, 2 ms) successfully maintained contractile function when applied to scaffold-free spheroids composed of enriched neonatal rat cardiomyocytes (i.e., <25% fibroblasts).<sup>45</sup> Based on electrical stimulation protocols for human cardiac tissue constructs established in previous studies and a spheroid size within the diffusional limit (i.e., 150  $\mu\text{m}$  radius), we empirically developed a viable electrical stimulation protocol (2.5 V/cm, 1 Hz, 5 ms) that supports optimal hiPSC cardiac spheroid viability and function (Figure 2.1, 2.6).<sup>40,41</sup>

Compared to unstimulated and unwired spheroids at Day 0 (NC-D0), treatment groups consisted of spheroids in prolonged culture (Day 19 - D19): unstimulated and unwired

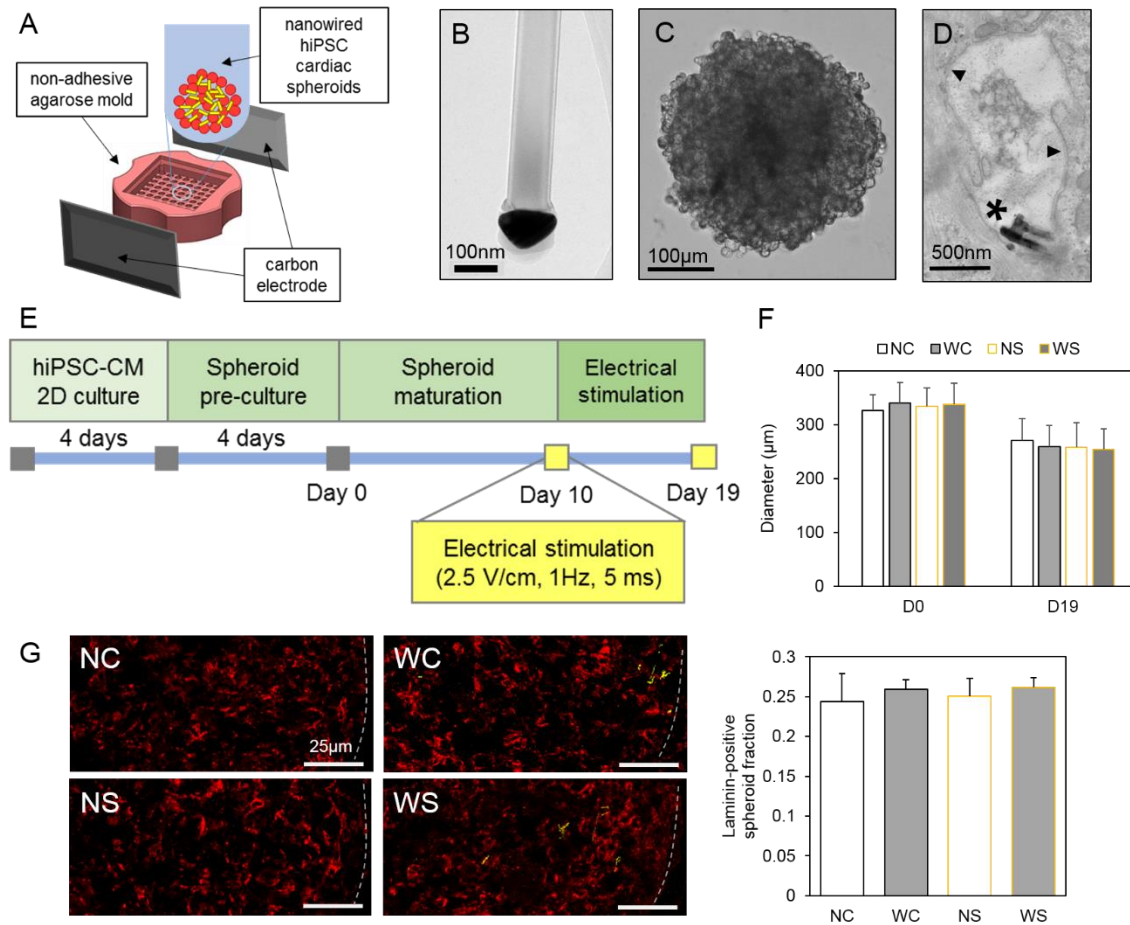


**Figure 2.1.** Development of electrical stimulation for nanowired hiPSC cardiac spheroids. (A) The schematic diagram of the stimulation setup shows cardiac spheroids cultured in non-adhesive agarose molds between carbon electrodes. (B) Transmission electron micrograph details the structure of n-type doped silicon nanowires. (C) Nanowired hiPSC cardiac spheroids assemble by Day 0 in non-adhesive agarose molds. (D) Transmission electron micrograph of spheroid section depicts nanowire location in extracellular space; asterisk - nanowire location, triangle – cell membrane. (E) The timeline of in vitro conditioning indicates specified electrical stimulation parameters and time points. Electrical stimulation and nanowires do not significantly change spheroid assembly indicated by consistent (F) spheroid size and (G) laminin expression; dotted line represents spheroid edge; red-laminin, yellow-silicon nanowires. NC-D0 - unwired and unstimulated at Day 0; NC – unwired and unstimulated at Day 19; WC – wired and unstimulated at Day 19; NS – unwired and stimulated at Day 19; WS – wired and stimulated at Day 19.



(NC) spheroids, unstimulated and wired (WC) spheroids, stimulated and unwired (NS) spheroids, and stimulated and wired (WS) spheroids. The nanowired hiPSC cardiac spheroids were prepared as described in our previous study.<sup>45</sup> Briefly, n-type SiNWs (Diameter  $\approx$  100 nm; length  $\approx$  10  $\mu$ m; Silane/Phosphane = 500) were mixed with hiPSC-CMs at a ratio 1:1 and seeded into agarose microwells to prepare nanowired spheroids (Figure 2.1A-2.1C). The length of the e-SiNWs was selected to inhibit cell internalization (Figure 2.1D), and the doping ratio and diameter of the e-SiNWs were chosen to obtain a high conductivity (150 - 500  $\mu$ S/ $\mu$ m) to create highly electrically conductive microenvironments within spheroids.<sup>44,202</sup> While unstimulated (i.e., NC and WC) spheroids showed spontaneous beating, stimulated (i.e., NS and WS) spheroids displayed successful pacing throughout the entirety of the experiment. High viability validated the biocompatibility of silicon nanowires and electrical stimulation condition for prolonged spheroid culture (Figure 2.6A, 2.6B). Constant decrease in spheroid size and uniform laminin production indicated similar microtissue formation processes among each condition (Figure 2.1F, 2.1G, 2.6C).

**Electrical stimulation and nanowires improve cell-cell junctions.** Proper propagation of electrical and mechanical signals in the heart is a tightly regulated process dependent on functional cell-cell junctions between cardiomyocytes. Functionally mature human cardiomyocyte junctions develop throughout postnatal childhood and are characterized by localized expression of electrically conductive channel proteins, such as connexin-43 (Cx43), supported by mechanical junction proteins, such as N-cadherin (N-

cad) and Zonula Occludens-1 (ZO-1).<sup>213-216</sup> As shown in the Figure 2.2A-E, all the treatment groups showed significantly improved expression of cellular junctions (i.e., Cx-43 and N-cad) than NC-D0 spheroids, which indicates the benefits of prolonged microtissue culture. In addition, WC and NS spheroids showed the enhanced expression of phenotypic immunofluorescent Cx43 punctii per nuclei when compared with unwired, unstimulated NC spheroids at D19 (Figure 2.2A, 2.2B), indicating the beneficial role of nanowires and electrical stimulation in the formation of electrically conductive cellular junctions.

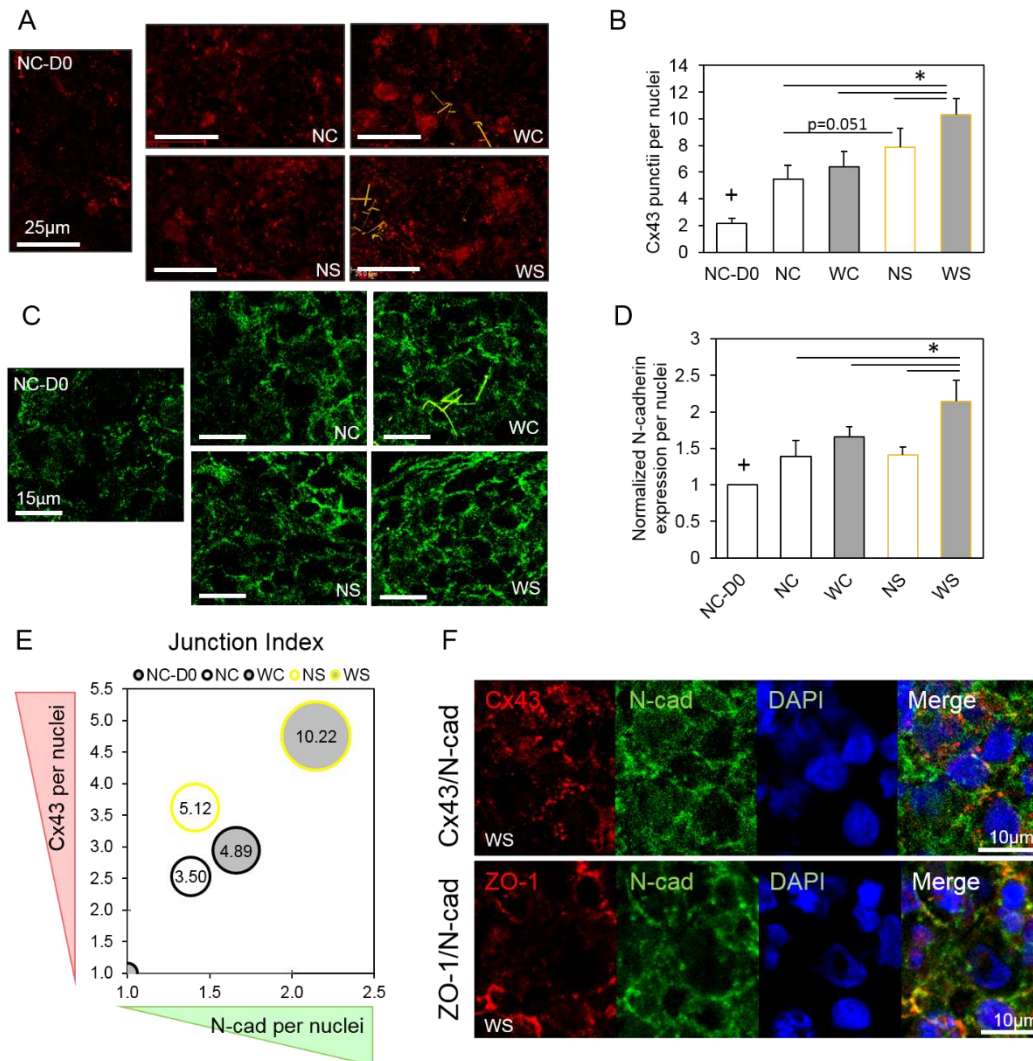


**Figure 2.2** (previous page). Synergistic contribution of electrical stimulation and nanowires to cellular junction formation. (A and B) Connexin-43 (Cx43) immunofluorescent staining shows an increased number of phenotypic puncta per nuclei in stimulated conditions; red-Cx43, yellow-nanowires; + = significant difference with NC-D0, \* = significant difference with unstimulated spheroids ( $p < 0.05$ ). (C and D) N-cadherin (N-cad) expression shows significantly higher staining per nuclei at the intercellular border in WS spheroids; green-N-cad, yellow-nanowires; \* - significant difference ( $p < 0.05$ ). (E) The junction index is the product (i.e., size of the circle) of the normalized (to NC-D0) Cx43 and N-cad expression per nuclei and represents the synergistic benefit in WS for cellular junction formation. (F) Representative staining for WS spheroids shows colocalization of Cx43 with N-cad and ZO-1 (Zonula Occludens-1), suggesting formation of functional cardiomyocyte junctions. NC-D0 - unwired and unstimulated at Day 0; NC - unwired and unstimulated at Day 19; WC - wired and unstimulated at Day 19; NS - unwired and stimulated at Day 19; WS - wired and stimulated at Day 19.

Further, significantly more Cx43 expression was found in the WS spheroids than both WC and NS spheroids and demonstrated the synergy between nanowires and electrical stimulation. Also, the WS spheroids showed a significant increase in N-cad expression per nuclei when compared with the remaining groups (Figure 2.2C, 2.2D). The expression of Cx43 and N-cad per nuclei allowed for the development of a cellular junction index that supports the synergy of electrical stimulation and nanowires in WS spheroids for cardiomyocyte junction formation (Figure 2.2E). Colocalized staining of Cx43 with N-cad and ZO-1 in WS spheroids showed not only expression of key junction proteins but also suggests functional cardiomyocyte junctions for enhanced electrical and mechanical coupling (Figure 2.2F). Enhanced junction formation seen in WS spheroids may facilitate their stable integration upon coupling with the host myocardium after transplantation.

**Enhanced contractile development in electrically stimulated, nanowired spheroids.** Improved junction formation supports cardiomyocyte coupling for contractile signal propagation. Spheroids were sectioned and stained with alpha sarcomeric actinin

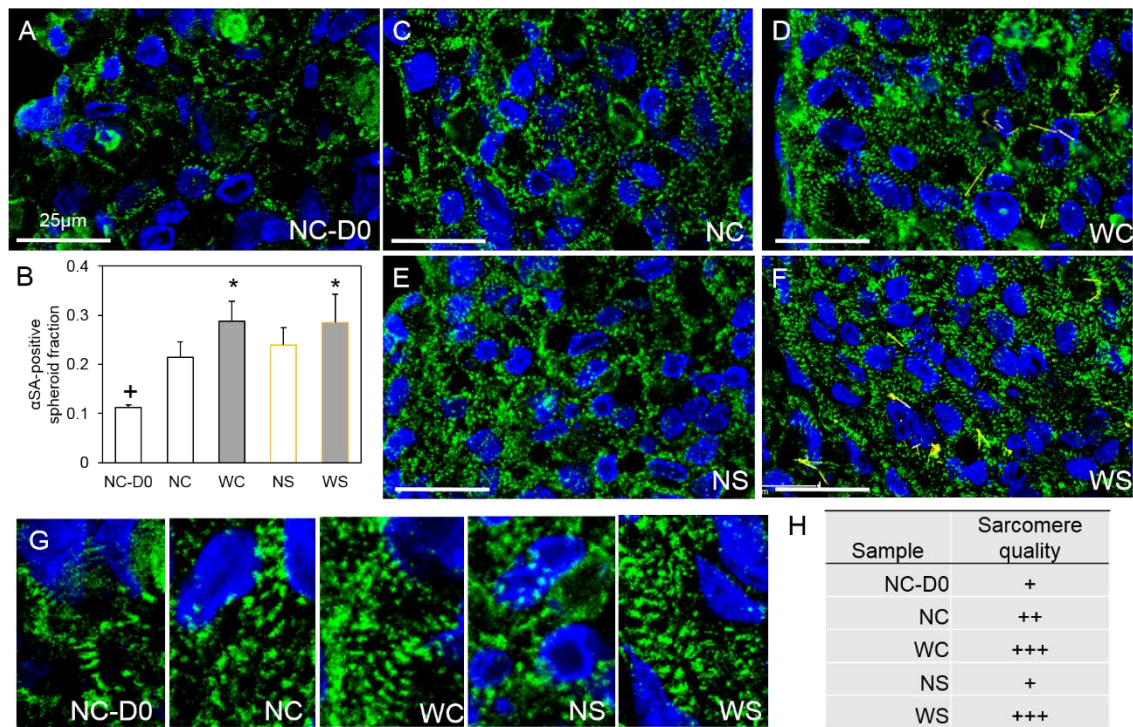


**Figure 2.3.** Nanowires influence sarcomeric organization in hiPSC cardiac spheroids. (A)  $\alpha$ SA immunofluorescent staining shows minimal sarcomeric organization at Day 0. (B-F) All conditions showed significantly increased  $\alpha$ SA-stained structures at Day 19 compared to NC-D0. The addition of nanowires further increases  $\alpha$ SA expression based on  $\alpha$ SA-positive area per spheroid area. green-  $\alpha$ SA, blue-DAPI nuclear stain. (G and H) High magnification  $\alpha$ SA-stained images and qualitative scoring show highest quality of sarcomere formation in WC and WS spheroids. + = significantly different from other groups; \* = significantly different from unwired groups ( $p < 0.05$ ). NC-D0 - unwired and unstimulated at Day 0; NC – unwired and unstimulated at Day 19; WC – wired and unstimulated at Day 19; NS – unwired and stimulated at Day 19; WS – wired and stimulated at Day 19.

( $\alpha$ SA) to visualize the sarcomeric organization, the structural units that support cardiomyocyte contraction. Consistent with the cell-cell junction staining, all the treatment groups showed significantly more  $\alpha$ SA-stained structures than that of NC-D0 spheroids (Figure 2.3). In addition, WC and WS spheroids showed enhanced  $\alpha$ SA-positive structures compared to NC and NS spheroids, while electrical stimulation alone (i.e., NS) did not change the amount of  $\alpha$ SA-positive structures significantly from NC spheroids

(Figure 2.3A-F). Further, high magnification  $\alpha$ SA images showed visible formation of sarcomeric banding in WC and WS spheroids and a lack of sarcomeric banding in NS spheroids (Figure 2.3G, 2.3H). This finding supported the critical role of e-SiNWs to improve contractile protein organization in electrically stimulated hiPSC-CM spheroids. This was further supported by the significant increases in expression of the sarcoplasmic reticulum ryanodine receptor (RYR2) in the WC and WS spheroids (Figure 2.7), which regulates intracellular calcium release required for cardiomyocyte contraction.

The benefits of nanowires for improved contractile characteristics were consistent with the genotypic and phenotypic characterization of treated hiPSC-CM spheroids. Genetically, the nanowired spheroids (i.e., WC, WS) exhibited increased ratio of beta myosin heavy chain ( $\beta$ -MHC; MYH7) to alpha myosin heavy chain ( $\alpha$ -MHC; MYH6) (Figure 2.4A). Individually,  $\beta$ -MHC expression increases significantly compared to Day 0 in nanowired groups, while  $\alpha$ -MHC did not change significantly (Figure 2.7). This isoform trend is consistent with in vivo maturation of human cardiomyocytes and the nonfailing adult human heart.<sup>24,217</sup> The increase in  $\beta$ -MHC/ $\alpha$ -MHC gene ratio has been reported to translate to the myosin protein shift and favors lower cellular ATPase activity.<sup>218-220</sup> This property may be an energetically favorable condition for transplanting cells into the energy-limited conditions of a damaged heart. In contrast, the NS group showed significantly lower  $\beta$ -MHC/ $\alpha$ -MHC ratio compared to the other groups. This suggests a limitation of electrical stimulation alone for contractile development of hiPSC cardiac spheroids. These findings were supported by immunofluorescent analysis of cardiac

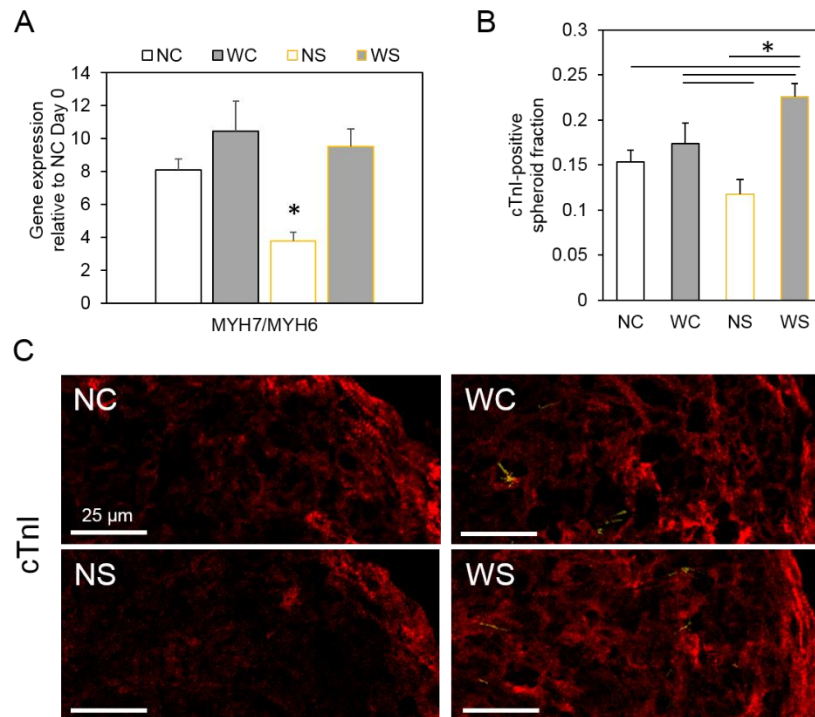


**Figure 2.4.** Nanowires and electrical stimulation affect development of contractile machinery in hiPSC cardiac spheroids. (A) Nanowires increase the ratio of beta myosin heavy chain (MYH7) to alpha myosin heavy chain (MYH6) expression, and NC, WC, and WS show statistical significance compared to NS. (B and C) Immunofluorescent expression of cardiac troponin I (cTnI) shows significant increases in nanowired conditions, indicating signs of contractile machinery maturation; red-cTnI. \* = significant difference from marked or remaining groups ( $p < 0.05$ ). NC-D0 - unwired and unstimulated at Day 0; NC – unwired and unstimulated at Day 19; WC – wired and unstimulated at Day 19; NS – unwired and stimulated at Day 19; WS – wired and stimulated at Day 19.

troponin I (cTnI), a key indicator of contractile protein maturation (Figure 2.4B, 2.4C).

While nanowired spheroids showed the improvement in cTnI expression when compared with their unwired spheroids, the electrical stimulation alone lead to the reduced cTnI expression. The significantly higher density of cTnI in the WS spheroids indicated a critical role of nanowires in promoting contractile development of hiPSC cardiac spheroids under electrical stimulation.<sup>221,222</sup>

### **Subtype specification of hiPSC-CM using electrical stimulation and nanowires.**

While current hiPSC-CMs are composed of heterogeneous subpopulations (i.e., ventricular-like, atrial-like, nodal-like cardiomyocytes), the observed improved contractile machinery suggests a shift towards a working myocardial phenotype. Specifically, electrical stimulation of hiPSC cardiac spheroids significantly increased ventricular myosin light chain (MYL2) over unstimulated spheroids (Figure 2.5A, left). No change was observed in atrial myosin light chain (MYL4), indicating an increase in overall ventricular-like contractile genotype of stimulated spheroids (Figure 2.5A). This was further supported with ventricular myosin light chain immunofluorescent staining (MLC-2v), showing significantly higher density of MLC-2v expression per spheroid in the WS condition (Figure 2.5B, 2.5C). This suggests that exogenous electrical stimulation may override the endogenous spontaneous electrical signals in hiPSC-CMs to regulate contraction in a pacemaker-like manner and promote the ventricular-like shift.

The observed shift in cardiomyocyte subpopulation characterization was further explored using beat rate analysis to examine hiPSC-CM spheroid function. Each spheroid condition was characterized by spontaneous beating throughout the entirety of the experiment. While the newly formed NC-D0 spheroids had an average beat rate ( $\pm$  s.e.m.) of  $35.5 \pm 3.0$  beats per minute (bpm), all the treatment groups showed a reduced spontaneous beat rate. With the 1 Hz stimulation treatment, the spontaneous beat rate of NS and WS spheroids significantly decreased to  $24.5 \pm 2.4$  and  $25.6 \pm 2.8$  bpm in comparison with NC and WC spheroids ( $30.4 \pm 3.4$  and  $29.2 \pm 3.9$  bpm, respectively) (Figure



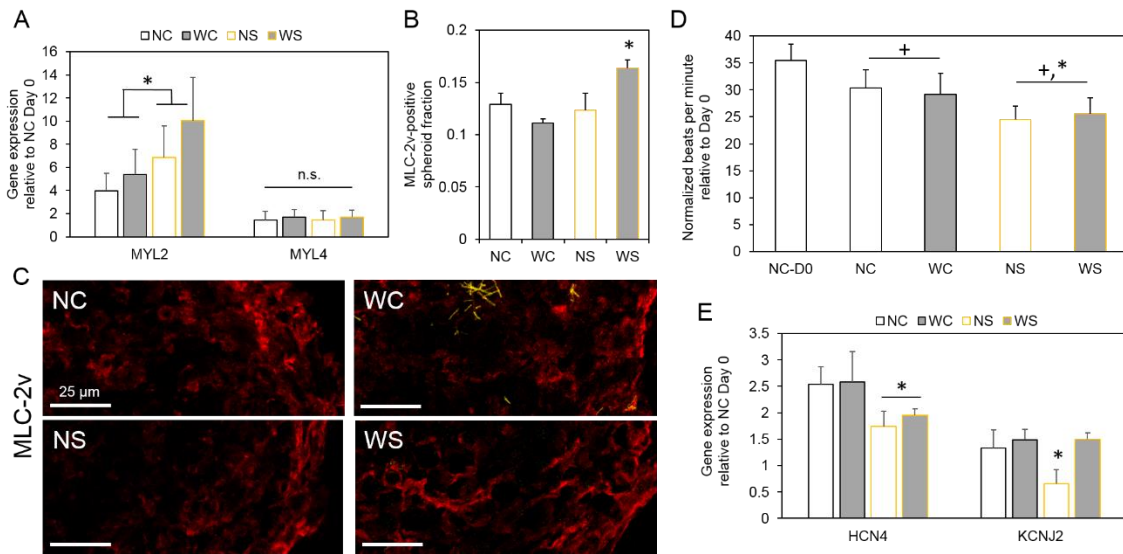


**Figure 2.5.** Electrical stimulation and nanowires directly affect subpopulation specification and beating properties in hiPSC cardiac spheroids. (A) Electrical stimulation significantly improves gene expression of ventricular myosin light chain (MYL2), while atrial myosin light chain (MYL4) is unchanged. (B and C) Immunofluorescent staining of the MYL2 protein, MLC-2v, supports genetic trend with significantly more expression per area in WS; red-MLC-2v. (D) Electrical stimulation significantly reduced the spontaneous beat rate of hiPSC cardiac spheroids compared to unstimulated and NC-D0 spheroids. + = significantly different from NC-D0; \* = significantly different from unstimulated groups ( $p < 0.05$ ). (E) Electrical stimulation significantly reduced the mRNA expression of HCN4, a pacemaker gene in the adult heart. The presence of nanowires preserved KCNJ2 expression when under stimulation, an important gene to prevent spontaneous contraction in adult ventricular cardiomyocytes. \* = significantly different from unmarked groups. NC-D0 - unwired and unstimulated at Day 0; NC – unwired and unstimulated at Day 19; WC – wired and unstimulated at Day 19; NS – unwired and stimulated at Day 19; WS – wired and stimulated at Day 19.

2.5D). The potential mechanism of this functional change due to an exogenous electrical field was explored using genetic analysis of ion channels known to be related to the spontaneous beating of hiPSC-CMs.<sup>24,223</sup> HCN4 is the dominant form of the HCN protein in nodal cells and contributes to the pacemaking mechanism of the sino-atrial node.<sup>24</sup> HCN4 is expressed during fetal ventricular expression but is down-regulated in the working myocardium during development and virtually absent in adults.<sup>224</sup> When



compared with unstimulated spheroids, electrical stimulation significantly reduced HCN4 expression, suggesting a shift away from a pacemaker-like genotype (Figure 2.5E, left). This decrease in HCN4 expression combined with a functional decrease in beat rate indicates a critical role of electrical stimulation in the regulatory mechanism governing hiPSC-CM spheroid electrical properties. Furthermore, the lack of inward rectifying channel (KCNJ2) expression has been shown to contribute to the spontaneous beating phenomenon in hiPSC-CMs.<sup>23,225</sup> Notably, under electrical stimulation, the addition of e-SiNWs to hiPSC cardiac spheroids was critical to preserve inward rectifying channel (KCNJ2) gene expression (Figure 2.5E, right). Interestingly, the significant decrease in KCNJ2 gene expression in NS is in line with the limited contractile development of NS discussed above. Nevertheless, electrical stimulation can synergize with e-SiNWs to provide exogenous and endogenous cues to affect the cardiomyocyte subpopulation specification and significantly decrease the spontaneous beat rate of hiPSC-CM spheroids. Notably, HERG (KCNH2) showed no significant changes with electrical stimulation at 1 Hz, which is consistent with the recent studies conducted by Eng and coworkers (Figure 2.7). They reported an up-regulated HERG expression with a 2 Hz stimulation treatment and un-changed HERG expression with 1 Hz stimulation.<sup>39</sup>

## **Conclusion**

To date, transplantation of hiPSC-CMs into damaged hearts have led to limited improvements in heart functions and increased risk of arrhythmia.<sup>115,226-228</sup> These results

alongside recent research showing enhanced cell retention using cellular aggregates indicate that hiPSC-CM microtissues with advanced cellular development provide an attractive cell delivery system for transplantation.<sup>114,229,230</sup> Our previous research showed that addition of e-SiNWs to hiPSC cardiac spheroids creates an electrically conductive microenvironment and significantly improves the structural and functional development of hiPSC cardiac spheroids.<sup>45</sup> In this study, we demonstrated that the addition of nanowires to the spheroids is essential for the utilization of electrical stimulation to improve the functions of hiPSC cardiac spheroids. With nanowires, exogenous electrical stimulation increases cell-cell junction formation (i.e., Cx-43 and N-cad), improves development of contractile machinery (i.e., sarcomeric structure,  $\beta$ -MHC/ $\alpha$ -MHC gene ratio and cTnI expression), and preserves KCNJ2 gene expression. In contrast, electrical stimulation alone (i.e., NS) showed increased Cx43 yet lower N-cad along with reduced sarcomere development, cTnI expression,  $\beta$ -MHC/ $\alpha$ -MHC gene ratio, and KCNJ2 gene expression. Although it has been reported that electrical stimulation alone can advance cardiomyocyte development in vitro, the data presented here suggests potential limitations of the use of electrical stimulation without nanowires in hiPSC cardiac spheroids for ventricular applications.

Remarkably, electrical stimulation of nanowired spheroids also resulted in a significant reduction in endogenous, spontaneous beat rate and shifts in cardiomyocyte subpopulation characterization. These phenomena point to the beneficial functional and genomic effects of exogenous electrical stimulation to affect the endogenous electrical

properties of nanowired hiPSC cardiac microtissues. The observed reduction of spontaneous beat rate and pacemaker-like genotype clearly demonstrates tissue level functional development that would be beneficial for reduced pacemaking/arrhythmic risk after transplantation.

In conclusion, we demonstrated, for the first time, that the combination of e-SiNWs and electrical stimulation synergistically improves cell junction formation, increases contractile properties, and reduces the endogenous spontaneous beat rate of hiPSC-CM spheroids. Enhancing the cell-cell junctions of hiPSC cardiac spheroids in vitro may lead to improved cellular integration and functional contribution after transplantation. The increased expression of contractile machinery in vitro indicates an increased cardiomyocyte developmental age, which has been shown to be advantageous for transplantation.<sup>31,231</sup> Given that many cardiac cell therapies target ventricular myocardial repair, the observed expression shift towards the ventricular isoform of myosin light chain shows promise for improved functional integration. Likewise, by decreasing the spontaneous beat rate in hiPSC cardiac spheroids and directly effecting genes that regulate the spontaneous beating of hiPSC-CMs, we propose that this in vitro conditioning model will reduce the arrhythmogenic risk of hiPSC-CMs. In addressing these underdeveloped properties of hiPSC-CMs with the combination of endogenous nanomaterials and exogenous stimuli, we hope to contribute to the next generation of cell therapy approaches for cardiac repair.

## Materials and Methods

*Electrically conductive silicon nanowire fabrication and harvesting.* Consistent with our previous work, single-crystalline SiNWs were synthesized using the nanocluster-catalyzed vapor-liquid-solid method described previously in a quartz tube connected to a gas manifold and vacuum pump and heated by a temperature controlled tube furnace.<sup>232</sup> Monodisperse gold nanoparticles (100 nm, Ted Pella) were dispersed on SiO<sub>2</sub>/silicon substrates, which were placed within the central region of the quartz tube reactor. The SiNWs were synthesized at 470-485 °C using silane (SiH<sub>4</sub>) as the silicon reactant source, H<sub>2</sub> as the carrier gas, and phosphine (PH<sub>3</sub>, 1000 ppm in H<sub>2</sub>) as the n-type dopants, according to the previously established protocol.<sup>201</sup> The length and diameter of the e-SiNWs were selected to inhibit cell internalization. The doping ratio with a silane/phosphine ratio of 500 was chosen to obtain a high conductivity (150 - 500  $\mu\text{S}/\mu\text{m}$ ) compared to cell culture medium ( $\sim 1.75 \mu\text{S}/\mu\text{m}$ ) and myocardium ( $\sim 0.1 \mu\text{S}/\mu\text{m}$ ) to create highly electrically conductive microenvironments within spheroids.<sup>44,202</sup> In a typical synthesis of uniform n-type, 100 nm SiNWs, the flow rates of SiH<sub>4</sub>, PH<sub>3</sub> and H<sub>2</sub> were 1-2, 2-4 and 60 standard cubic centimeters per minute, respectively, and the total pressure 40 torr. The nanowires were collected from the oxidized silicon substrates by sonication in isopropanol for 1 min followed by centrifugation to obtain SiNWs with an average dimension of 100 nm diameter and 10  $\mu\text{m}$  length. The electrical conductivity of the SiNWs were measured by using four-probe transport measurement.

*hiPSC-CM cell culture.* Human induced pluripotent stem cell-derived cardiomyocytes (hiPSC-CMs) (iCell Cardiomyocytes, Cellular Dynamics International-CDI, Madison, WI, USA) were cultured according to the manufacturer's protocol. Briefly, hiPSC-derived cardiomyocytes were plated on 0.1% gelatin coated 6-well plates in iCell Cardiomyocyte Plating Medium (CDI) at a density of about  $3 \times 10^5$  to  $4.0 \times 10^5$  cells/well and incubated at 37 °C in 5% CO<sub>2</sub> for 4 days. Two days after plating, the plating medium was removed and replaced with 4 mL of iCell Cardiomyocytes Maintenance Medium (CDI). After 4 days of monolayer pre-culture, cells were detached using trypLE Express (Gibco Life Technologies, Grand Island, NY) and prepared for spheroid fabrication.

*Spheroid fabrication and electrical stimulation.* As described in our previous publication,<sup>45</sup> the agarose hydrogel molds were prepared using autoclaved 2% agarose (Sigma Aldrich, St. Louis, MO) and commercial master micro-molds from Microtissues, Inc (Providence, RI) as negative replicates to create non-adhesive agarose hydrogels molds containing 35 concave recesses with hemispheric bottoms (800 µm diameter, 800 µm deep) to facilitate the formation of tissue cell spheroids. A suspension of hiPSC-derived cardiomyocytes were mixed with e-SiNWs in media at a 1:1 ratio (number of cells:number of SiNWs) for a final concentration of  $2.0 \times 10^6$  cells/mL. Approximately 75 µl of the cell/e-SiNW suspension was pipetted into each agarose mold. After the cells settled into the recesses of the mold (10 min), additional media was added to submerge the molds in an 8-well plate and exchanged every 2 days for the length of the experiment. Day 0 of the experiment was marked after 4 days of spheroid assembly. Electrical stimulation (C-Pace

unit, Ion Optix, Milton, MA) was started on Day 10 (2.5V/cm, 5 ms). A ramp-up method (Day 1 – 0.5 Hz, Day 2 – 0.75 Hz) was used to bring the frequency of stimulation to 1 Hz for the remainder of the experiment. Here, Day 19 represents  $7 \pm 1$  days of stimulation at 1 Hz. A scheme of the experimental setup is found in Figure 2.1A and 2.1B.

*Beat rate analysis of beating spheroids.* Videos of spontaneously beating spheroids from each group were recorded at room temperature (after temperature stabilization) without stimulation for each condition starting on Day 0 using Zen 2011 software (Zeiss, Göttingen, Germany). Videos were converted to a series of TIFF format pictures by Adobe Premiere (Adobe, San Jose, CA). Threshold edge-detecting in ImageJ software (National Institutes of Health) was used on high contrast spheroid picture series and graphed to realize beating profiles, from which beats per minute was calculated (n=15-50 spheroids). Diameter of each spheroid was calculated from the threshold-based area of high contrast spheroid images (n=15-50 spheroids).

*Immunofluorescent analysis.* Freshly collected spheroids were flash frozen in Tissue-Tek OCT compound (Sakura, Torrance, CA). Embedded spheroids were cryosectioned into 7  $\mu$ m thickness layers onto glass slides for immunohistochemistry. The sections were fixed with pre-cooled acetone ( $-20^{\circ}\text{C}$ ) for 10 min. After washing (2 times at 5 min) in PBS with 0.1% Triton X-100 (PBST) (Sigma), blocking buffer was made with 10% serum corresponding to host species of secondary antibody in PBST and added to sections for 1 hr at room temperature. Sections were incubated with primary antibody diluted in PBST (1:200): laminin (Sigma), connexin-43 (Sigma), N-cadherin (BD Biosciences, San Jose,

CA), ZO-1 (Thermo Fisher Scientific, Waltham, MA), alpha sarcomeric actinin (Abcam, Cambridge, UK), cardiac troponin I (Abcam), MYL2 (Abcam) overnight at 4 °C or 2 hrs at room temperature. After washing in PBST (2 times at 5 min), tissues were incubated with complement secondary antibodies diluted in PBST for 1 hr at room temperature. After washing in PBST (2 times at 5 min), nuclei were counterstained with DAPI (Molecular Probes/Invitrogen, Eugene, OR) diluted in PBST for 15 min at room temperature. Following the final wash procedure (PBST, 2 times at 5 min), glass cover slips were added to the slides using Fluoro-Gel (Electron Microscopy Sciences, Hatfield, PA) and slides were stored in 4 °C. TCS SP5 AOBS laser scanning confocal microscope (Leica Microsystems, Inc., Exton, PA) was for imaging. Fluorescent protein expression was calculated as the antibody-positive fluorescence area coverage divided by the number of nuclei or spheroid area. Each analysis consisted of 2-3 high resolution images at 400X total magnification of 3-5 spheroids to obtain an accurate representation of the entire spheroid.

*TUNEL staining for frozen spheroids section.* Roche In Situ Cell Death Detection Kit (Sigma) was used to determine the viability of cells in the frozen sections of spheroids based on the Roche protocol. Briefly, the frozen sections of spheroids were fixed with 4% paraformaldehyde in PBS for 20 min at room temperature. Following washing in PBS for 30 minutes, samples were incubated in a permeabilization solution (0.1% Triton X-100 and 0.1% sodium citrate in PBS) for 2 minutes on ice. Then 50 µl of the TUNEL reaction mixture were added to samples and incubated at 37 °C for 1 hr. After washing in PBS (2 times at 5 min), nuclei were counterstained with DAPI (Molecular Probes/Invitrogen)

diluted in PBS for 15 min at ambient temperature. Following the final wash procedure (PBS, 2 times at 5 min), glass cover slips were added to the slides using Fluoro-Gel (Electron Microscopy Sciences). TCS SP5 AOBS laser scanning confocal microscope (Leica Microsystems) was used for imaging.

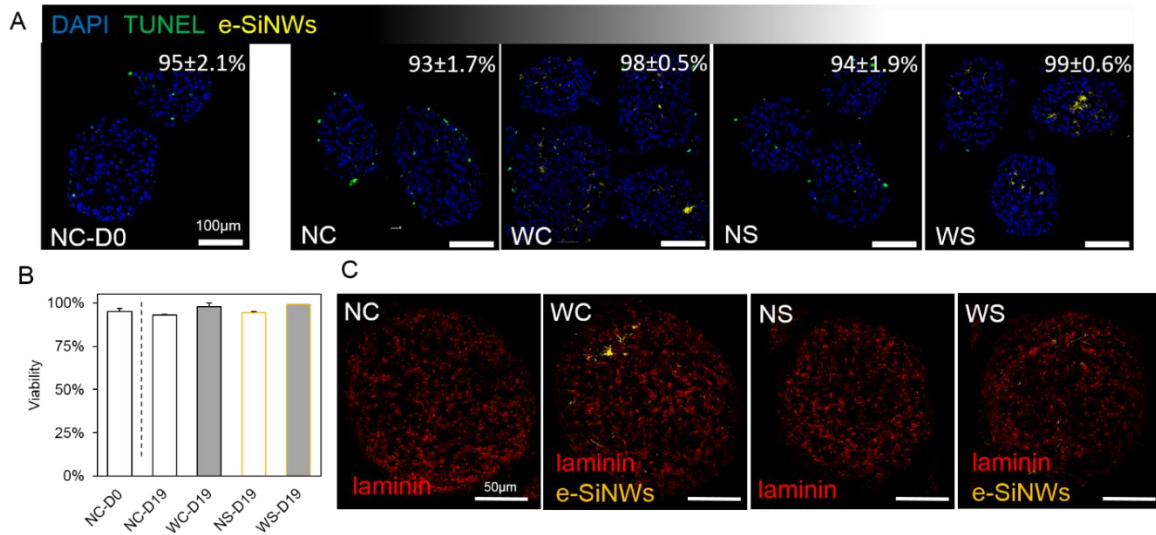
*Gene expression with qRT-PCR.* Total RNA was isolated according to the kit and protocol of an RNeasy Micro Kit (Qiagen, Vinlo, Netherlands) with the addition of the Homogeneizer Columns (Omega Biotek, Norcross, GA) during the homogenization step for spheroids. For each group, a minimum of 15 spheroids were used for RNA isolation. At least 25 ng of total RNA for each group was subjected to cDNA synthesis using the Bio-Rad (Hercules, USA) iScript cDNA synthesis kit. qRT-PCR step was performed using validated Life Technologies Taqman primers (Thermo Fisher Scientific) in 10 µl reactions for the targeted genes listed in Table S1. Data was normalized as the change in cycle threshold (Ct) to the geometric mean of GAPDH and ACTB (dCt) and analyzed using, mRNA expression =  $2^{-dCt}$ . Data was then normalized to NC-D0 gene expression and averaged across n=3 experiments.

*Statistics Analysis.* Differences between experimental groups were analyzed using one-way and two-way ANOVA and Tukey's post-hoc test, and  $p < 0.05$  was considered significantly difference for all statistical tests.



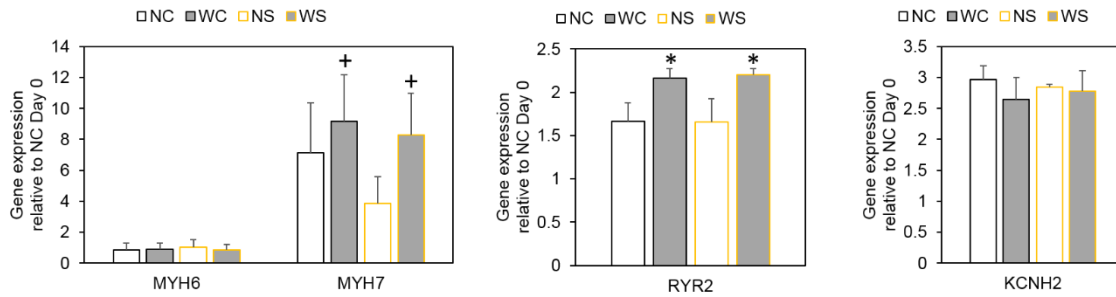
## Supporting Information

Figure 2.6.



**Figure 2.6.** hiPSC cardiac spheroid assembly. (A) TUNEL staining of frozen spheroid sections show high viability; blue-DAPI nuclear stain, green-TUNEL apoptotic nuclei. (B) Quantification of TUNEL-based viability shows high viability among all groups. (C) Laminin immunofluorescent staining reveals consistent laminin production throughout the whole spheroid in each condition; red-laminin, yellow-nanowires. NC-D0 - unwired and unstimulated at Day 0; NC – unwired and unstimulated at Day 19; WC – wired and unstimulated at Day 19; NS – unwired and stimulated at Day 19; WS – wired and stimulated at Day 19.

Figure 2.7.



**Figure 2.7.** Gene expression analysis of hiPSC cardiac spheroids. The analyzed genes correspond to the following aliases: MYH6 – alpha myosin heavy chain; MYH7 – beta myosin heavy chain; RYR2 – ryanodine receptor; KCNH2 – HERG channel. + = significantly different with Day 0; \* = significantly different from remaining groups ( $p < 0.05$ ). NC – unwired and unstimulated at Day 19; WC – wired and unstimulated at Day 19; NS – unwired and stimulated at Day 19; WS – wired and stimulated at Day 19.

Table 2.1

Taqman primers used for gene analysis.

Gene symbol	Primer ID
ACTB	Hs01060665_g1
GAPDH	Hs02758991_g1
GJA1	Hs00748445_s1
HCN4	Hs00975492_m1
KCNH2	Hs04234270_g1
KCNJ2	Hs01876357_s1
MYH6	Hs01101425_m1
MYH7	Hs01110632_m1
MYL2	Hs00166405_m1
MYL4	Hs04187281_m1
RYR2	Hs00181461_m1

## CHAPTER FOUR

### DEVELOPMENT-DRIVEN INSPIRATION FOR BIOMIMETIC SELF-ASSEMBLY OF HUMAN CARDIAC ORGANIDS

#### **Introduction**

With the advancement of human induced pluripotent stem cell technologies, the emerging human organoids have provided a powerful platform to model human organ development and pathologies, as well as provide cell delivery systems for regenerative therapy.<sup>57,58</sup> Organoids are 3D structures based on the self-organization of stem cell-derived organ-specific cell types to recapitulate major tissue/organ structures and functions. To this end, the development of a variety of functional human organoids (e.g., lung, liver, brain) has given novel insight into developmental and pathological processes.<sup>56,89,233-235</sup> Despite the increasing progress in other organ systems, few studies have focused on the development of a human cardiac organoid.<sup>236,237</sup> Recapitulation of the 3D multicellular structure and function of the developing myocardium remains a challenge for the development and application of human cardiac organoids.<sup>238</sup>

Significant advancements, however, have been made in the utilization of human induced pluripotent stem cell derived-cardiomyocytes (hiPSC-CMs) at the cellular and genetic level for the development of disease models and drug screening systems.<sup>96,239,240</sup> In addition to 2D culture systems, significant resources have been devoted to developing 3D myocardial constructs to support cardiomyocyte development and improve viable transplantation approaches.<sup>241</sup> Strategies have been engineered to target specific

physiologically relevant features (e.g., multicellular, capillary-like diffusion, electrical stimulation) in the myocardium to improve cardiomyocyte functions and development.<sup>39,46,48-51,242,243</sup> To this end, early cardiac tissue engineering efforts, such as the work of Kelm and others, demonstrated that cardiac spheroids made from a mixed cell population derived from neonatal/fetal rodent hearts supported myocardial extracellular matrix profile and cardiomyocyte sarcomere development.<sup>29,244</sup> This has been supported further by several hiPSC-CM-based studies showing that supporting cell types provide extracellular matrix microenvironment, incorporate angiogenic signaling, enhance microtissue assembly, and improve maturation of cardiac microtissues.<sup>53-55,245-248</sup> Furthermore, the addition of vascular cell types to cardiac microtissues can model aspects of coronary angiogenesis and provide a functional benefit in heart repair by connecting to the host vasculature after transplantation.<sup>51,244,248,249</sup> By targeting specific hiPSC-CM functions/properties, tissue-engineered cardiac systems have been advantageous for the development of more sensitive drug testing models and improved cell delivery strategies. However, by using “output” structures/functions as the input design principle, these platforms can exclude tissue/organ-level intricacies that are critical for modeling cardiac development and pathologies.

While cardiac differentiation of embryoid bodies holds great potential for cardiovascular organoid production<sup>236,237</sup>, the intramyocardial organization events in coronary vasculogenesis provides the biological inspiration for a method of controlled, scaffold-free human cardiac organoid fabrication using defined cell types. In

development, after the 4-chamber heart structure has formed, the formation of the epicardium involves a dynamic process of epithelial-mesenchymal transition of epicardium-derived cells that migrate into the myocardium and differentiate into vascular and cardiac interstitial cell types.<sup>250-252</sup> Subsequently, the developing ventricular myocardium undergoes the intramyocardial organization events of coronary vasculogenesis where a diverse, yet defined, mixture of cardiac cell types (e.g., cardiomyocytes, cardiac fibroblasts, vascular cell types) organize into functional myocardium before anastomosis to the aorta (Figure 3.1A, 3.1B).<sup>253-256</sup> At this point in development, the cardiomyocytes also retain a spontaneous beating property, in part, due to incomplete sub-type specification of the cardiomyocytes, similar to hiPSC-CMs.<sup>24,30</sup> Inspired by these events and the developing/immature characterization of hiPSC-CMs, we have established a defined, scaffold-free fabrication strategy to assemble vascularized human cardiac organoids in vitro that recapitulate an array of structural, genetic, and functional cardiac tissue-level characteristics of the developing myocardium. Through incorporation of the events of coronary vasculogenesis as the major design principle in human cardiac organoids, the technology described here provides a powerful platform to incorporate and investigate the cellular, matrix/material and additional factors required to promote tissue/organ-level heart development. Furthermore, this platform lays down the foundation for the development of functional cardiac tissues for tissue-/organ-level drug screening and advanced cell therapy for heart repair.

## Results and Discussion

**Developmental inspiration for cardiac organoid fabrication.** The dynamic cellular organization events of coronary vasculogenesis during heart development (after the 4-chamber structure as formed) provided a developmental basis for the fabrication of cardiac organoids, represented in Figure 3.1A. To prepare human cardiac organoids, we

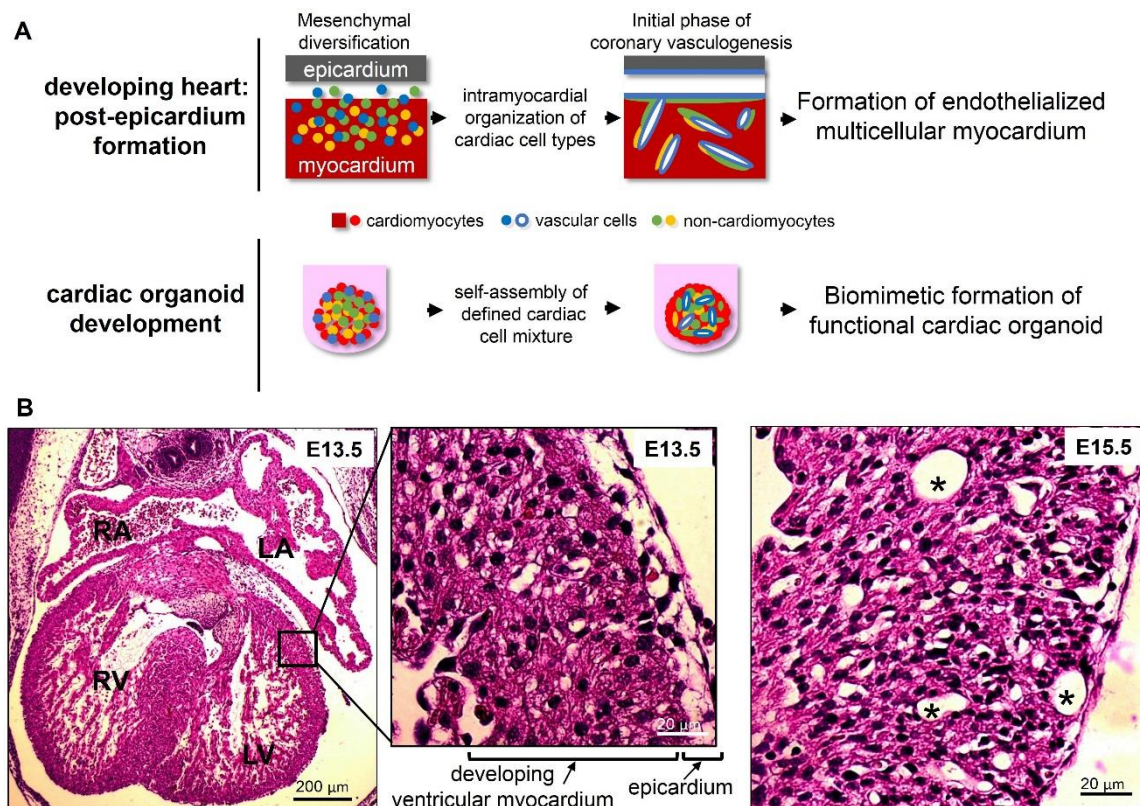


**Figure 3.1.** Developmental inspiration for organoid fabrication. (A) In the developing heart after the 4-chamber structure has formed, the epicardium and subsequent epithelial-to-mesenchymal transition give rise to a diverse mixture of cardiac cell types. This stage of intramyocardial organization marks the initial phase of coronary vasculogenesis. The self-assembly process surrounding this intramyocardial organization served as inspiration for analogous, self-assembled cardiac organoids from a defined mixture of cardiac cells prior to blood flow. (B) Hematoxylin and eosin-stained mouse embryonic heart sections at embryonic day 13.5 (E13.5) show the 4-chamber structure and the epicardium adjacent to the developing ventricular myocardium (inset). By E15.5 (right), evidence of preliminary coronary vessels

utilized hiPSC-CMs, human ventricular cardiac fibroblasts (cFBs) and human umbilical vein endothelial cells (HUVECs) to represent the major cardiac cell types in the developing myocardium. Due to their immature characteristics, hiPSC-CMs served as an appropriate cell type to represent cardiomyocytes in the developing myocardium.<sup>24</sup> While aligned cardiac microtissue research has significantly enhanced the understanding of stem cell-derived cardiomyocyte mechanical/electrical properties (e.g., contraction force, conduction velocity)<sup>21,48,243,257,258</sup>, the cardiac organoid system does not incorporate an aligned cardiomyocyte design to resemble the developing heart at the stage of coronary vasculogenesis, in which significant anisotropic cardiomyocyte organization has not been established (Figure 3.1B). During the spheroid fabrication, the ratio between different cardiac cells was selected to approximate cell ratios in developing hearts (5:4:1, hiPSC-CMs:cFBs:HUVECs).<sup>259-261</sup> As an alternate rationale, human cardiac organoids were also fabricated using the ratio of cells corresponding to adult hearts (3:6:1, hiPSC-CMs:cFBs:HUVECs) (Figure 3.2A-C).<sup>259-261</sup> The experimental timeline can be seen in Figure 3.8.

By experimental Day 10 (D10), the developing stage ratio cardiac organoids showed significantly higher contraction amplitude (i.e., fractional area change) and regularity of beating than adult ratio organoids, which was attributed in part to the higher hiPSC-CM composition in the developing stage ratio organoids (Figure 3.2D, 3.2E). In addition, the difference in the contraction profiles was supported by enhanced sarcomere development (e.g., Z-line formation) in developing stage ratio organoids at D10 when



compared to adult ratio organoids, which have minimal Z-line formation despite still having alpha sarcomeric actinin ( $\alpha$ -SA)-positive regions (Figure 3.9). This suggested that the developing stage ratio provided a favorable microenvironment for hiPSC-CM

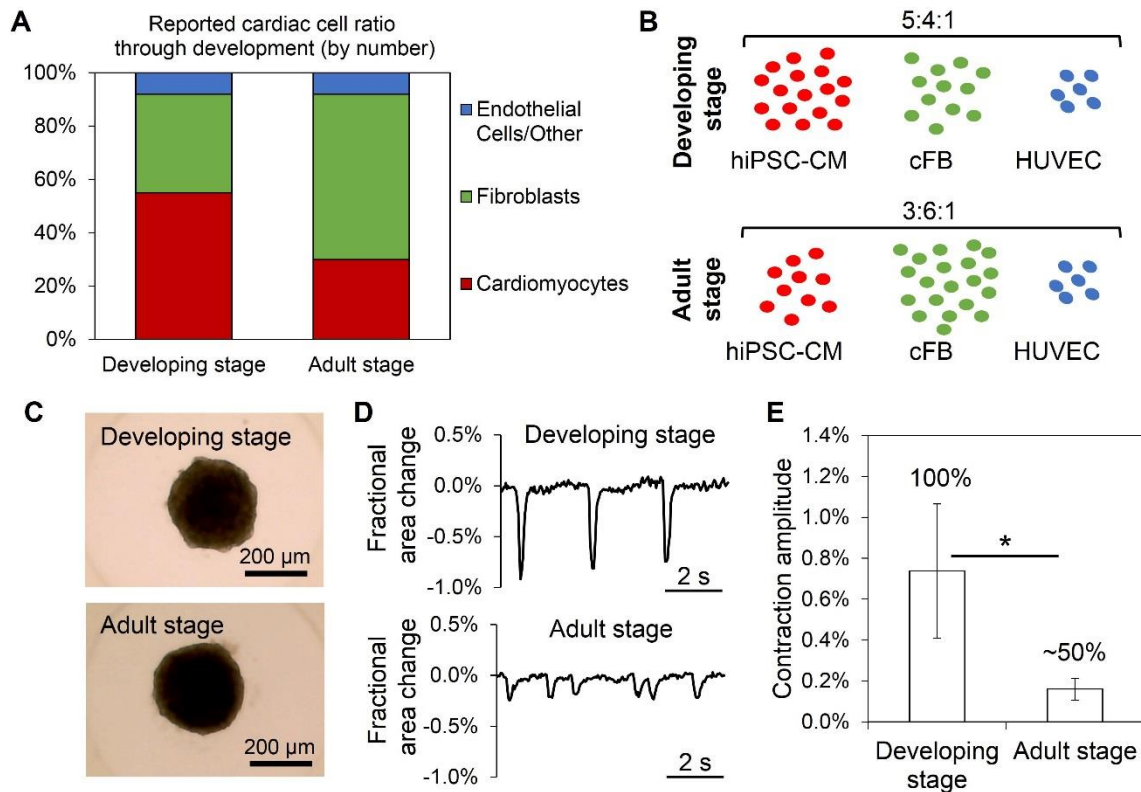


**Figure 3.2.** Examination of developmental inspiration for cardiac cell ratio for organoid fabrication. (A) The ratio of cardiac cell types (by number) changes throughout development, based on reported literature ref. 259-261. (B, C) A developing stage and adult stage cell ratios of cardiac cell types represent two organoid fabrication rationales to support cardiomyocyte development, seen in bright-field images at D0; n=human induced pluripotent stem cell-derived cardiomyocytes (hiPSC-CM), human cardiac ventricular fibroblasts (cFB), human umbilical vein endothelial cells (HUVEC). (D) Representative contraction profiles for developing stage and adult stage ratio organoids were constructed from video analysis of spheroid fractional area change. (E) Analysis of average ( $\pm$ SEM) contraction amplitude (i.e., fractional area change) showed significant differences at D10; n=8-12 organoids. Developing stage ratio organoids showed 100% of organoids beating at D10, while adult stage ratio organoids had only ~50% beating. Asterisk represents significant difference,  $p < 0.05$ .

development and supported the developmental basis for cardiac organoid fabrication. This finding is consistent with previous engineered findings showing that cardiac constructs containing a majority of cardiomyocytes of the construct supports increased hiPSC-CM functions.<sup>32,39,48,243</sup> The developing stage cell ratio for cardiac organoids was used for the remainder of the experiments.

To examine the effects of media components on organoid formation and maturation, DMEM/F12 media with varying amounts of FBS was prepared and compared to a ratiometric combination of cardiomyocyte media (DMEM/F12, 10% FBS), fibroblast media (FGM-3, defined growth factors, 10% FBS), and endothelial cell media (EGM-2, defined growth factors, 2% FBS) corresponding to the cell ratio (Figure 3.10). After 4 days of organoid formation, the cardiac organoids with the ratiometric combination showed significantly better viability index (i.e., reduced TUNEL-positive apoptotic nuclei) and was used for the remainder of the experiments.

**Phenotypic cellular behavior in human cardiac organoids.** Immunofluorescent analysis using von Willebrand factor (vWF) and CD31 endothelial markers of the cardiac organoids revealed limited staining and spreading of HUVECs at D0 through D10 (Figure 3.3A). Human adipose-derived stem cells (hADSCs) were added to the cardiac organoid system to promote endothelial function based on their pericyte-like function and pro-angiogenic properties.<sup>161,262-267</sup> Cardiac organoids with hADSCs were fabricated with 50% hiPSC-CMs, 29% cFBs, 14% HUVECs, and 7% hADSCs. The relative amount of hADSCs reflects the limited amount of pericytes in the heart, supported by previous research in

endothelial-ADSC co-culture systems (Figure 3.3B).<sup>245,262</sup> The effects of hADSCs were noticeable from D0 by enhanced organization of vWF-positive cells (i.e., HUVECs) in a circular pattern surrounding the inner portion of the organoid (Figure 3.3A). By D10, the addition of hADSCs increased indications of enhanced endothelial function and/or viability, described by the increased covered area of vWF-positive structures, and

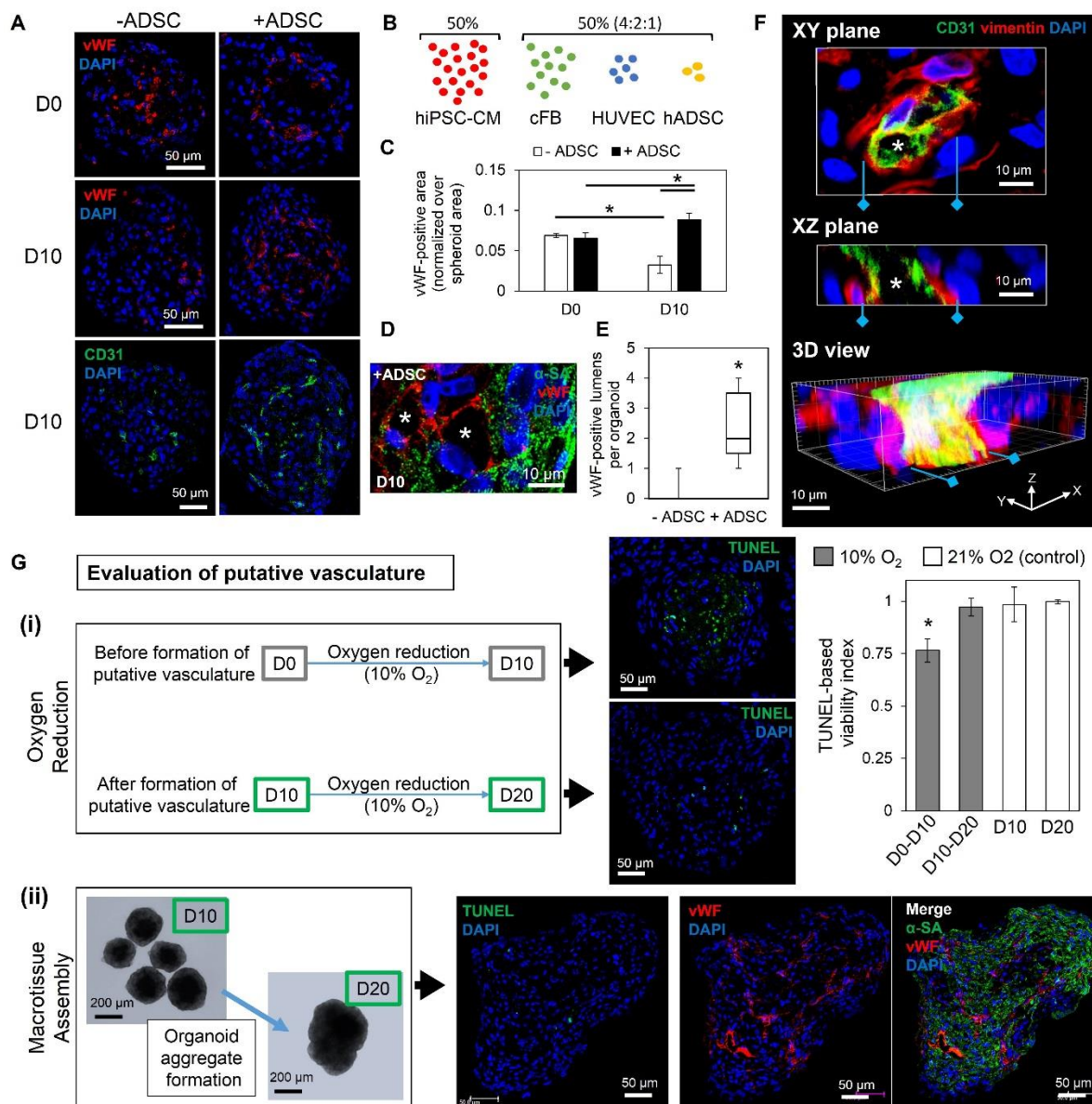


**Figure 3.3** (previous page). The addition of human adipose derived stem cells improves biomimetic formation of functional, lumenized vascular networks in cardiac organoids. (A) The addition of adipose-derived stem cells (+ADSC) led to increased vWF- and CD31-positive endothelial network formation by D10. Without human adipose-derived stem cells (-hADSC), cardiac organoids showed limited endothelial staining; n=3 organoids/group per endothelial stain. (B, C) The addition of hADSCs to the developmentally inspired cardiac organoid fabrication significantly improved the vWF-positive area over spheroid area by D10; n=3 organoids. (D) Lumen-like structures (asterisk) were observed in D10 cardiac organoids with hADSCs with vWF-positive (red) endothelial cells within  $\alpha$ -SA-positive (green) hiPSC-CMs areas; blue-DAPI. (E) Significantly more vWF-positive lumen structures were observed per organoid in D10 organoids with hADSCs in comparison to without hADSCs; n=10 organoids per group. (F) 3D reconstruction of thick sections of D10 cardiac organoids with hADSCs show 3D structure of a CD31-positive (green) vessel with open lumens (asterisk) supported by vimentin-positive (red) support cells; blue-DAPI. (G) Evaluation of putative vasculature showed (i) that culturing cardiac organoids from D0-D10 (before putative vasculature formation) in an oxygen-reduced environment (10% O<sub>2</sub>) for 10 days resulted in a significant decrease in viability in the center, indicated by TUNEL apoptosis assay, compared to cardiac organoids with formed lumenized vascular networks (D10-D20) and D10 and D20 controls (21% O<sub>2</sub>); n=4-7 organoids. (ii) Macrotissue assembly using five D10 cardiac organoids cultured 10 days (D10-D20) showed minimal TUNEL expression and displayed extensive vWF-positive endothelial networks across the whole macrotissue (n=3 macrotissues). Cardiac organoids were fabricated using a developing stage cell ratio. Asterisk represents significant difference, p<0.05.

promoted EC network formation in cardiac organoids compared to without hADSCs, as shown by vWF and CD31 staining (Figure 3.3A, 3.3C).

As in coronary vasculogenesis, where vascular cell types and cardiac interstitial cells form the endothelial plexus in the beating myocardium before connecting to the future coronary artery<sup>253</sup>, lumen-like structures with vWF-positive cells were found within the cardiac organoids bordered by  $\alpha$ -SA-positive hiPSC-CMs, although not every vWF-positive cell participated in the lumen formation (Figure 3.3D). Notably, cardiac organoids with hADSCs showed significantly more vWF-positive lumen structures than without

hADSCs (Figure 3.3E). 3D reconstruction of thick cardiac organoid sections revealed CD31-positive vessel structures supported by vimentin-positive cells (Figure 3.3F). Serial images of confocal imaging of vWF-stained whole organoids further confirmed the formation of multiple areas with lumen-like regions in X, Y, and Z perspectives connected by vWF-positive ECs (Figure 3.11). The increase in vWF- and CD31-positive structures and lumen formation demonstrated the structural functionality of the HUVECs and was largely attributed to the pro-angiogenic role of hADSCs. This is supported by a growing amount of research indicating a perivascular origin and properties of mesenchymal stem cells (e.g., hADSCs), which is consistent with other studies showing the pro-angiogenic properties of hADSCs <sup>262-266</sup>. In addition, the organizational changes seen after the addition of hADSCs is consistent with other multicellular research that indicates a higher order level of self-organization beyond differential cell adhesion dynamics.<sup>237,268</sup> Furthermore, vascular endothelial growth factor (VEGF) signaling plays an important role during coronary vasculogenesis.<sup>269</sup> Gene expression of vascular endothelial growth factor A (VEGFA) and the main VEGF-A receptor 2 (VEGFR2) in cardiac organoids and spheroids of each individual cell type indicated the potential role in angiogenic signaling within cardiac organoids between the major VEGF providers (hiPSC-CMs, cFB, hADSCs) and VEGF receiver (HUVECs) (Figure 3.12).

To evaluate the functionality of the putative vasculature, cardiac organoids were placed in an oxygen-reduced environment (10%) before (D0) and after (D10) putative vasculature had formed for 10 days. Cardiac organoids cultured at 10% O<sub>2</sub> from D0 (before

putative vasculature formation) showed a significant increase in TUNEL expression at the organoid center when compared to cardiac organoids cultured at 10% O<sub>2</sub> from D10 (Figure 3.3G(i), 3.13). This strongly indicates the formation of putative vasculature reduces cell apoptosis in the organoids center, suggesting their function to improve nutrient transport within the organoids. In addition, we examined whether the putative vasculature in the cardiac organoids can allow for the fabrication of large viable cardiac tissue engineering constructs, as oxygen diffusion in the engineered cardiac tissue is limited to a 100-200  $\mu$ m range.<sup>270,271</sup> To this end, cardiac organoids were cultured for 10 days to form putative vasculature and then placed in groups of five to form organoid aggregates. Macrotissue assembly was observed until D20, where the aggregates had formed large macrotissues (>200  $\mu$ m radius) with observable increased Z-dimension. TUNEL analysis showed no significant changes in viability by D20 and immunofluorescent staining revealed large regions of connected, vWF-positive endothelial cells (i.e., networks) across the organoid macrotissues (Figure 3.3G(ii), 3.14). The observed enhanced viability in both cases strongly indicates a functional benefit of putative vasculature, which is consistent with previous studies incorporating vascular networks in rodent-cell based and scaffold-based engineered cardiac constructs for improved viability/integration after transplantation and evident from cardiovascular tissue engineering studies showing large necrotic core in large scaffold-free constructs without pre-established vasculature.<sup>236,272-274</sup> This improvement may be attributed to the enhanced passive transport of nutrients whereby the presence of lumens creates a porous construct that increases diffusivity to the center

of the micro-/macrotissues.<sup>275</sup> These data support the functional benefit of recapitulating the lumenized vascular network of the developing myocardium in the cardiac organoids.

To explore the effects of endothelial cell source on the vasculature formation in the organoids, we substituted HUVECs with human adipose-derived microvascular endothelial cells (HAMECs) to fabricate cardiac organoids due to their microvascular/capillary origin *in vivo*.<sup>276</sup> HAMEC cardiac organoids showed some evidence of network formation but overall showed less vWF-positive cells than HUVEC cardiac organoids on D10, while the cardiomyocyte organization was similar in both cases (Figure 3.15). This is consistent with reduced *in vivo* vascular network density observed in

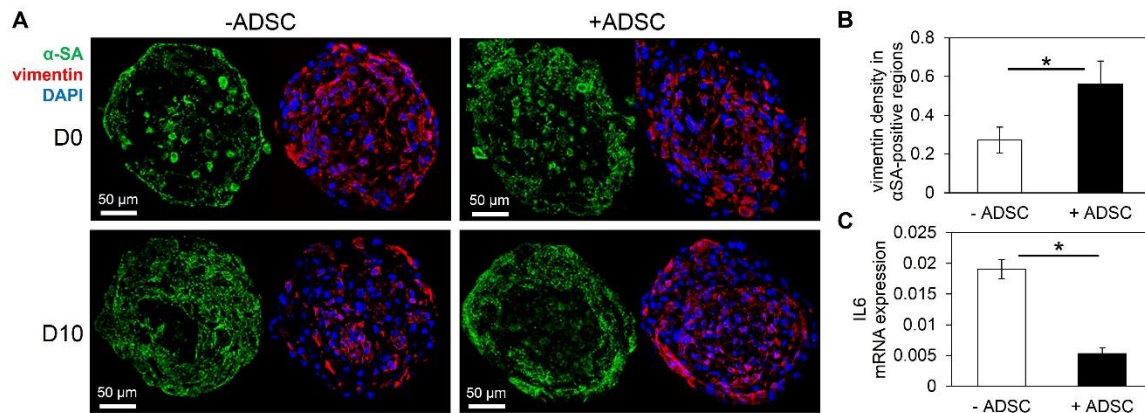


**Figure 3.4.** The addition of human adipose derived stem cells affects biomimetic cellular organization and introduces immunomodulatory effects. (A) α-SA-positive (green) hiPSC-CMs were mainly located in the outer region of spheroid cross-sections with or without hADSCs. The addition of hADSCs showed more homogeneous distribution of vimentin-positive (red) cells by D10; blue-DAPI. (B) The density of vimentin-positive staining area within α-SA regions significantly increased in cardiac organoids with hADSCs; n=3-4 organoids. (C) hADSCs demonstrated immunomodulatory role by significantly decreasing the expression of IL6 in cardiac organoids with hADSCs; n=3 experiments, 10-15 organoids/experiment. Cardiac organoids were fabricated using a developing stage cell ratio. Asterisk represents significant difference,  $p < 0.05$ .

transplanted human dermis-derived microvascular endothelial cells compared to HUVECs.<sup>277</sup> These results may reflect tissue-specific and/or developmental age properties of the cell source that influence their angiogenic/vasculogenic and structural functionality.<sup>278-281</sup> However, given their facile, readily expandable culture properties and consistent vasculogenic characteristics in cardiac organoids, HUVECs were used for the remainder of the experiments.

As for the hiPSC-CM, cFB, and hADSC organization, D0 cardiac organoids with or without hADSCs showed heterogeneous populations of vimentin-positive cells (i.e., cFBs and hADSCs) throughout the microtissue (Figure 3.4A). The majority of  $\alpha$ -SA-positive hiPSC-CMs with or without hADSCs organized in the outer regions of the cardiac organoids. In the native myocardium, adjacent fibroblast-cardiomyocyte interactions are critical for cardiac development.<sup>282</sup> By D10, cardiac organoids with hADSCs displayed an increased density of vimentin-positive cells in the  $\alpha$ -SA-positive (i.e., hiPSC-CMs) regions of the cardiac organoid (Figure 3.4A, 3.4B). Furthermore, the immunomodulatory potential of hADSCs was supported by a significant reduction in the pro-inflammatory interleukin IL6 gene expression in cardiac organoids, compared to organoids without hADSCs (Figure 3.4C).<sup>283</sup>

**Extracellular matrix (ECM) protein production in human cardiac organoids.** In addition to the phenotypic cellular distribution throughout the cardiac organoid, the extracellular matrix proteins in the cardiac organoids supported the development of an organotypic microenvironment. One limitation in hiPSC-CM spheroids (i.e., microtissues



composed of 100% hiPSC-CMs) is the lack of collagen in the microtissue. While hiPSC-CM spheroids showed limited collagen I expression throughout the experiment with disconnected, dotted structures, the cardiac organoids expressed significantly more collagen I-positive, connected structures indicative of mature, stable collagen fibril formation (Figure 3.5A). This difference was attributed to the presence of cardiac fibroblasts in the organoids, as collagen is maintained by the cardiac fibroblasts in the

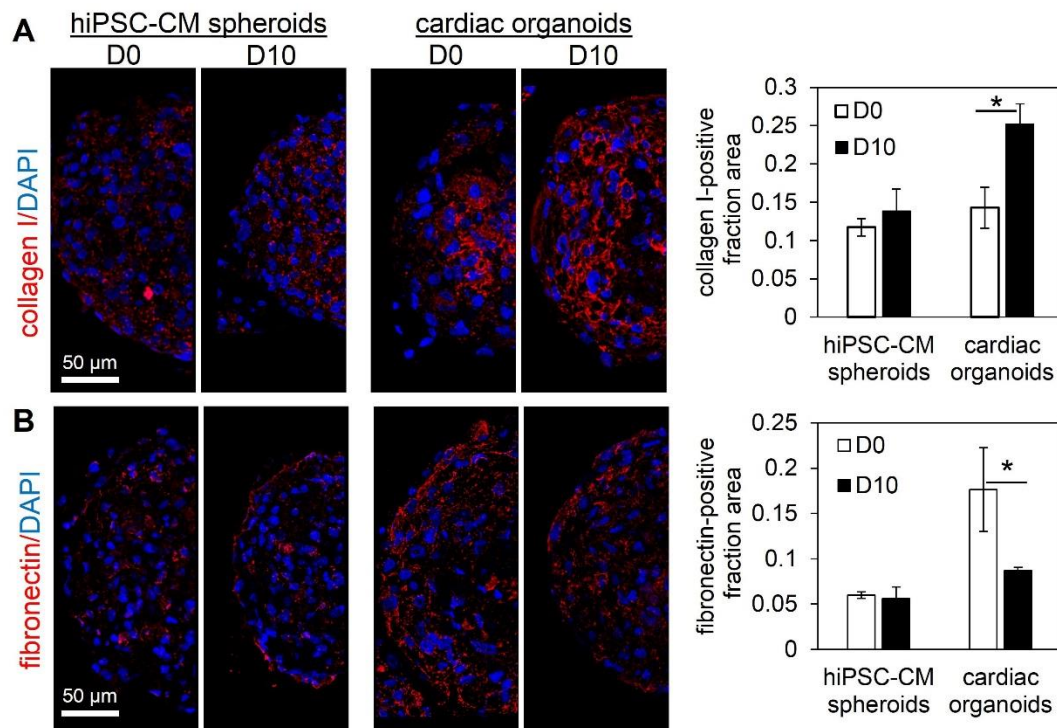


**Figure 3.5.** Human cardiac organoids display organotypic extracellular matrix (ECM) components. (A) Spheroids comprised of 100% hiPSC-CMs (hiPSC-CM spheroids) showed limited, dotted collagen I immunofluorescent staining, while cardiac organoids showed significantly increased, connected collagen I structures by D10. (B) hiPSC-CM spheroids showed overall low levels of fibronectin expression, while cardiac organoids decreased significantly by D10. Quantification of ECM components was based on the ratio of ECM-positive covered area divided by total spheroid area. hiPSC-CM-human induced pluripotent stem cell-derived cardiomyocyte. Cardiac organoids were fabricated using a developing stage cell ratio; n=3-6 microtissues. Asterisk represents significant difference,  $p < 0.05$ .

native myocardium.<sup>282</sup> As shown in the Figure 3.5A, collagen I expression in the organoids increased from D0 to D10, consistent with results from developing hearts.<sup>284</sup>

Notably, in cardiac organoids, fibronectin-positive spheroid area decreased significantly from D0 to D10, while hiPSC-CM spheroids showed overall low levels of fibronectin-positive structures at D0 and D10 (Figure 3.5B). This may suggest the formation of non-pathological, ventricular-like extracellular microenvironment to support development of hiPSC-CMs, as fibronectin has been shown to be more abundant in atrial than ventricular myocardium, and increased ventricular fibronectin is associated with pathological cardiac hypertrophy.<sup>285,286</sup> The changes in fibronectin in cardiac organoids (high to low from D0 to D10) may also indicate the increased role of fibronectin during microtissue formation evidenced by the high levels at D0 and/or the observed role of fibronectin in myofibril organization in cardiac development.<sup>287-290</sup> In addition, the basement membrane protein (laminin) is produced by hiPSC-CMs and showed strong immunofluorescent expression in both hiPSC-CM spheroids and cardiac organoids throughout the experimental timeline (Figure 3.16). Cardiac organoids provide a biomimetic matrix environment that supports cardiac function and can serve as a model for biomaterial/construct design in exploring the necessary material components for cardiac development.

**Enhanced cardiomyocyte development within cardiac organoids.** Previous work using hiPSC-CM spheroids has indicated conditioning approaches and extended culture are required to enhance the contractile properties toward physiological relevance.<sup>45,241</sup>

We next explored the effect of cellular and matrix microenvironment as a biomimetic stimulus in the organoids to promote the contractile properties of hiPSC-CM. During the

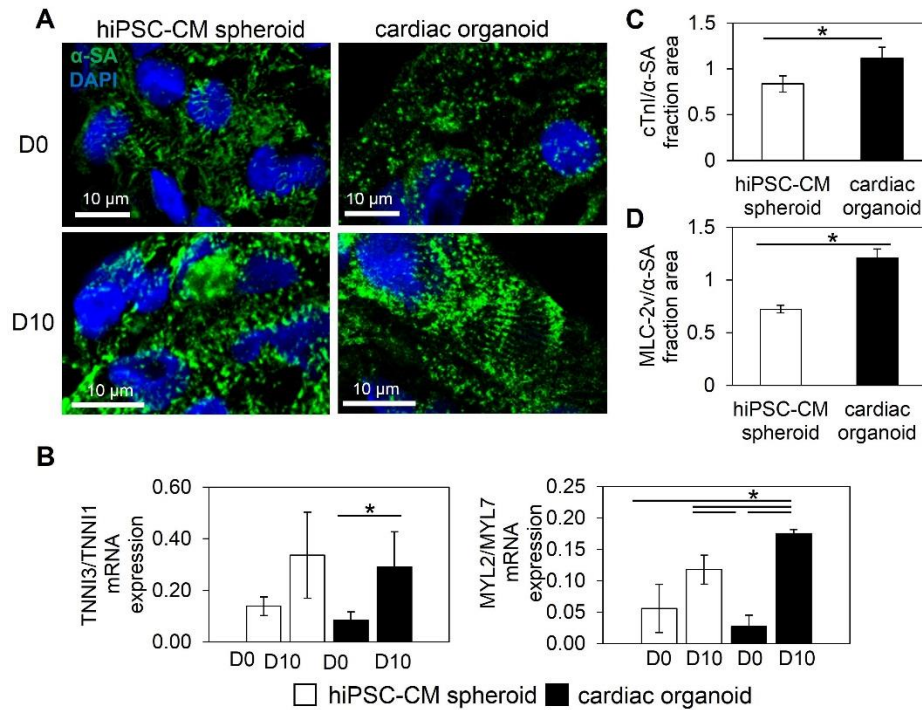


**Figure 3.6.** Human cardiac organoids support contractile development of hiPSC-CMs. (A) Cardiac organoids showed signs of improved sarcomere development (e.g., Z-line width) by D10 in comparison to hiPSC-CM spheroids. (B) Ratiometric gene expression of hiPSC-CM spheroids and cardiac organoids reveal improvements in hiPSC-CM development within microtissues. Gene expression of cardiac troponin I (TNNI3) over slow, skeletal troponin I (TNNI1) showed greater significant increases in cardiac organoids, indicating improved contractile maturation of hiPSC-CMs by D10. Ratiometric expression of myosin light chain ventricular isoform (MYL2) over atrial isoform (MYL7) showed more significant increases by D10 in cardiac organoids, indicating improved ventricular specification of hiPSC-CMs; n=3 experiments, 10-15 microtissues/experiment. (C,D) Shifts in gene ratios were supported by increased cardiac troponin I (cTnI)-positive and ventricular myosin light chain (MLC-2v)-positive fraction area over  $\alpha$ -sarcomeric actinin ( $\alpha$ -SA)-positive area (hiPSC-CM-specific areas), represented by low and high magnification immunofluorescent images; n=3 microtissues. Cardiac organoids were fabricated using a developing stage cell ratio. hiPSC-CM- human induced pluripotent stem cell-derived cardiomyocyte. Asterisk represents significant difference,  $p < 0.05$ .

process of self-assembly, hiPSC-CM spheroid spontaneous beating started after two days of spheroid assembly (D-2), while cardiac organoid spontaneous beating started after four days of spheroid assembly (D0). hiPSC-CM spheroids at D0 showed more phenotypic banding of  $\alpha$ -SA-positive Z-lines than cardiac organoids, however, by D10 the cardiac organoids showed more enhanced organization (e.g., Z-line width) of sarcomeres than hiPSC-CM spheroids (Figure 3.6A). Particularly, the presence of Z-line widths greater than 10  $\mu$ m was observed more frequently among different cardiac organoids (13 out of 19; n=5 experiments) than in hiPSC-CM spheroids (1 out of 10; n=3 experiments) seen in Figure 3.17A, supporting the reproducibility of human cardiac organoids.

To further evaluate contractile improvements in cardiac organoids, contractile maturation and cardiomyocyte subtype specification (i.e., ventricular) were examined. As an indicator of contractile maturation<sup>221</sup> and to evaluate hiPSC-CM-specific development, ratiometric gene expression of adult cardiac troponin I and immature troponin I (i.e., TNNI3/TNNI1) revealed a significant increase in TNNI3/TNNI1 in cardiac organoids and an insignificant increase in hiPSC-CM spheroids from D0 to D10 (Figure 3.6B). This was further supported by significantly higher density of cardiac troponin I (cTnI) expression in the cardiac organoids than hiPSC-CM spheroids, when normalized to the  $\alpha$ -SA-positive area of stained spheroid sections (Figure 3.6C, 3.17B). To examine the cardiac organoids for working myocardium development, ventricular myosin light chain (protein:MLC2v, gene:MYL2) and atrial myosin light chain (protein:MLC2a, gene:MYL7) were used for ratiometric gene expression. At D10 both cardiac organoids and hiPSC-CM spheroids

showed increased ventricular/atrial (i.e., MYL2/MYL7) expression, though cardiac organoids showed a significantly greater shift toward ventricular gene expression (Figure 3.6B). In addition, the immunofluorescent expression of MLC2v showed increased staining density per  $\alpha$ -SA-positive regions in cardiac organoids over hiPSC-CM spheroids (Figure 3.6D, 3.17C). Although both groups show spontaneous beating throughout the experiment, the observed enhanced sarcomere development, increased adult cardiac troponin I expression, and a greater ventricular shift in expression supports the development of hiPSC-CMs in cardiac organoids.

Interestingly, the contraction amplitude of cardiac organoids is significantly lower than hiPSC-CM spheroids ( $0.61 \pm 0.25\%$  vs.  $1.98 \pm 1.2\%$ ), despite having similar spontaneous beat rates (cardiac organoids:  $36.9 \pm 8.0$  beats per minute (bpm) vs. hiPSC-CM spheroids:  $33.8 \pm 3.4$  bpm) (Figure 3.18). The low contraction amplitude of cardiac organoids is possibly due to the increased extracellular matrix components (e.g., collagen) and interstitial cell types, resulting in a denser/stiffer construct that creates an increased load for cardiomyocyte contraction. This was supported by the improved contractile structure and gene profile in cardiac organoids despite low contraction amplitude, highlighting the importance of the multicellular and matrix environment for hiPSC-CM maturation and ventricular lineage specification seen by others.<sup>245,291</sup> It is worth noting that the observed relationship between cardiomyocyte function and changes in cellular/ECM components is equally important to cardiac development and maturation as it is to cardiac pathophysiology, such as in chronic cardiac fibrosis.<sup>292,293</sup> The previously

mentioned data from Figure 3.2D and 3.2E (showing decreased contraction amplitude with increased fibroblast number) also supports these tissue-level dynamics and offers evidence of possible pathological applications within a tunable cardiac organoid system.

**Human cardiac organoids display phenotypic responses to pharmacological compounds.** For a functional cardiac organoid, the observed phenotypic structure, organization, and contractile development in D10 cardiac organoids must also be supported by demonstrated functions of fundamental characteristics of cardiac tissue. Given that calcium handling in cardiomyocytes is involved in electrical signal generation and propagation and is intimately involved in the contractile apparatus<sup>24</sup>, the explored improvements in contractile characteristics of cardiac organoids suggested functioning calcium-handling properties. Membrane calcium channels (e.g., L-type calcium channel) contribute to the initiation of the calcium-induced calcium-release (CICR) phenomenon in cardiomyocytes. Verapamil is a multi-channel blocker that causes a decreased calcium transient peak due to a large calcium L-type channel blockade. However, it has served as a false-positive arrhythmogenic drug in hERG channel based arrhythmogenic drug screening.<sup>69</sup> Administration of 500  $\mu$ M of verapamil resulted in a significant decrease in peak fluorescence and no observed arrhythmogenic activity (Figure 3.7A). This response validates the phenotypic functionality of L-type calcium channels to support CICR dynamics for contraction. The initial inward flux of calcium then binds to ryanodine receptors on the sarcoplasmic reticulum that release the intracellular stores of calcium located in the sarcoplasmic reticulum to provide enough calcium for contraction. To

examine the calcium release functionality of cardiac organoids, the ryanodine receptor

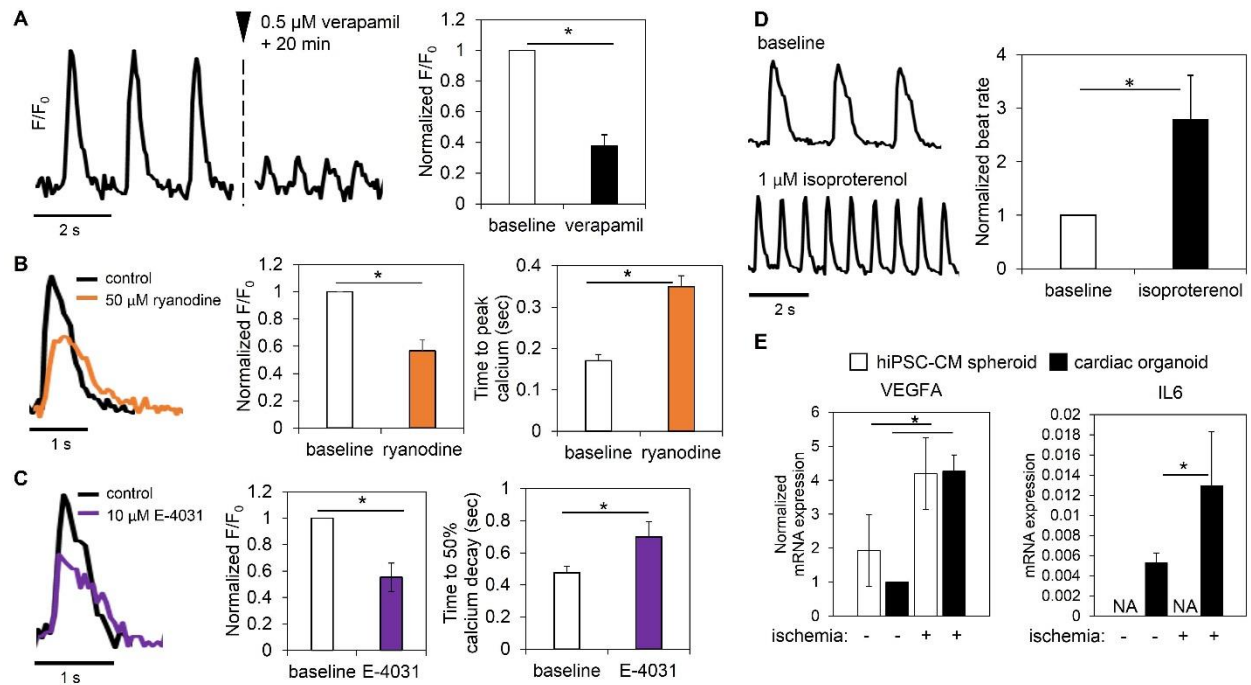


**Figure 3.7.** Human cardiac organoids display phenotypic channel functionality and organotypic responses to physiological/pathological stimuli. Cardiac organoids showed functional calcium handling. (A) Verapamil, which blocks the L-type calcium channel, displayed significant phenotypic reduction of calcium transient amplitude without inducing arrhythmia in cardiac organoids; n=4 organoids. (B) The use of ryanodine, known to block the ryanodine receptor of the sarcoplasmic reticulum and reduce endogenous calcium release, showed a significant decrease in calcium transient amplitude and a significant increase time to peak calcium; n=3 organoids. (C) Blockade of the hERG potassium channel using E-4031 showed a significant drop in calcium transient peak and a significant increase in time to 50% calcium decay; n=3 organoids. (D) A significant increase in beat rate after application of isoproterenol indicated intact  $\beta$ -adrenergic signaling in cardiac organoids; n=5 organoids. (E) Cardiac organoids showed organotypic transcription responses to ischemic stimuli; n=3 experiments; 10-15 microtissues/experiment. Cardiac organoids and hiPSC-CM spheroids showed increased VEGFA expression in response to ischemic stimulus. IL6 expression, a prominent interleukin in ischemic heart failure, increased in cardiac organoids in ischemia, while it was not detected in hiPSC-CM spheroids. hiPSC-CM-human induced pluripotent stem cell-derived cardiomyocytes. Cardiac organoids were fabricated using a developing stage cell ratio and were used at D10. Asterisk represents significant difference,  $p < 0.05$ .

was blocked using 50  $\mu$ M ryanodine. Ryanodine receptor blockade resulted in a significant decrease in peak calcium transient (Figure 3.7B). Also, ryanodine administration significantly increased time to peak calcium, indicating proper function of the ryanodine receptor to regulate the intracellular flux of calcium required for contraction. These results demonstrated the cardiac organoids recapitulate important calcium handling properties of working human myocardium.

To counter the flux of calcium during contraction, potassium channels, such as the hERG potassium channel, play a large role in repolarization phase of the cardiac action potential.<sup>24</sup> To examine the repolarization functionality of cardiac organoids, hERG potassium channels were blocked with 10  $\mu$ M E-4031. By blocking a major potassium channel, repolarization is slowed, indicated by an extension in calcium transient decay time. Blockade of the hERG channel resulted in significantly decreased peak calcium and a significant phenotypic extension of the time to 50% calcium decay (Figure 3.7C). Together with calcium handling results, these data showed the cardiac organoids supported the proper development of tissue-level channel functions.

**Human cardiac organoids display phenotypic functionality under physiological and pathological stimuli.** A series of physiologically relevant stimuli showed indications of a wider range of tissue-level functionality of cardiac organoids beyond drug screening and electrical property development. Beta-adrenergic signaling is a physiological process of beat rate regulation by the autonomic nervous system by catecholamines.<sup>294</sup> Using video analysis of the beating rate of cardiac organoids, a beta-adrenergic agonist,



isoproterenol (1  $\mu$ M), showed a significant increase in beat rate (Figure 3.7D). This validates the intact beta-adrenergic signaling pathways in hiPSC-CMs within the cardiac organoids for physiologically relevant stimulation.

Despite immature characteristics of cardiac organoids compared to adult ventricular tissue, the presence of fundamental physiological cardiac functions provided a basis for exploring critical pathways involved in cardiac pathologies, supported by recent progress using hiPSC-CMs for cardiac pathophysiology insights.<sup>102,240,295-297</sup> Particularly, cardiac organoids have potential to serve as an in vitro cardiac model for ischemic heart failure, which makes up the majority of cardiovascular-related disorders.<sup>298</sup> To evaluate the initial response to a pathological stimulus, cardiac organoids and hiPSC-CM spheroids were cultured for 6 hrs in ischemia. While the VEGFA expression in cardiac organoid is lower than the hiPSC-CM spheroids in a normoxia environment, ischemic stimulus led to a significant increase in VEGF-A gene expression in the cardiac organoids to similar levels to that of hiPSC-CM spheroids (Figure 3.7E). Spheroids of each cell type all showed increases in VEGFA expression under ischemic conditions (Figure 3.19A). hiPSC-CMs and cFBs showed the highest levels of ischemic VEGFA expression, suggesting their dominant role in VEGF signaling during ischemic stress. This trend is analogous to increases in VEGF expression in ischemic cardiac tissue and further supports the biomimetic regulation of VEGFA expression in cardiac organoids.<sup>299</sup> Furthermore, the addition of non-cardiomyocytes into the cardiac organoids system incorporated an extended inflammatory response, namely, IL-6 gene expression, a prominent interleukin up-

regulated in heart failure. After ischemic insult, IL6 expression increased significantly in cardiac organoids and was absent in CM spheroids (Figure 3.7E). This was attributed the presence of cFB in the organoids as single cell spheroid evaluation showed cFBs with the highest levels of IL-6 gene expression in response to ischemic stimuli (Figure 3.19B). Drug-based and biomimetic stimulation of cardiac organoids can provide a fundamental and potentially clinically relevant platform to explore the critical pathways involved in cardiac pathophysiology.

## **Conclusion**

With inspiration from major events in coronary vasculogenesis and a defined method of microtissue fabrication, we have developed a robust platform to fabricate vascularized human cardiac organoids that recapitulated the lumenized vascular network of the developing myocardium, supported hiPSC-CM development and demonstrated fundamental cardiac tissue-level functions. In contrast to the common organoid fabrication approach of directed differentiation of embryoid bodies (EBs), the dynamic cellular organization surrounding coronary vasculogenesis provided the developmental basis for the use of defined cell types to develop a tunable cardiac organoid system. This platform provides a consistent and efficient method of human cardiac organoid fabrication (e.g., 100% beating, consistent cellular organization, and minimal size variability) that supports high throughput applications (e.g., drug testing) in comparison to cardiovascular EB differentiation, where there is high variability in size and morphology

with only ~2%-15% of EBs showing contractile beating.<sup>236</sup> Furthermore, while hiPSC-CMs have been extensively used to model cardiac disorders, other cardiac cell types, such as cardiac fibroblasts and endothelial cells, are involved in many cardiac pathologies.<sup>300,301</sup> The use of a defined cardiac cell mixture for cardiac organoid formation is advantageous by providing an adaptable system to incorporate and investigate the contribution of each cardiac cell type, matrix materials, additional factors, and other physiological system relationships (e.g., immunological cell types) to cardiac developmental/pathological dynamics at a tissue/organ level.

In addition, similar to developing cardiomyocytes, the spontaneous beating property of hiPSC-CMs supports contractile development and provided the source of pacing in the cardiac organoids. To obtain adult stage ventricular maturation, in which cardiomyocytes do not beat spontaneously, exogenous pacing may be required. Interestingly, recent optimizations in stem cell-derived cardiomyocyte media suggest that mature contractile characteristics, such as positive force-frequency, can be achieved through the supply of defined growth factors.<sup>243</sup> Looking toward future applications, cardiac organoids with lumenized vascular networks provide a tunable foundation to develop future pre-vascularized, injectable vehicles for regenerative cell therapy to treat heart failure. In summary, the human cardiac organoid technology presented here provides a robust platform for the development of the next generation of hiPSC-based cardiac organoids in pursuit of developmental and pathological insight for regenerative medicine applications.

## Materials and Methods

*Cell culture.* Human induced pluripotent stem cell-derived cardiomyocytes (hiPSC-CMs) (iCell Cardiomyocytes, Cellular Dynamics International-CDI, Madison, WI, USA) were cultured according to the manufacturer's protocol. Briefly, hiPSC-derived cardiomyocytes were plated on 0.1% gelatin coated 6-well plates in iCell Cardiomyocyte Plating Medium (CDI) and incubated at 37 °C in 5% CO<sub>2</sub> for 4 days. Two days after plating, the plating medium was removed and replaced with 4 mL of iCell Cardiomyocytes Maintenance Medium (CDI). After 4 days of monolayer pre-culture, cells were detached using trypLE Express (Gibco Life Technologies, Grand Island, NY) and prepared for spheroid/organoid fabrication. Human cardiac ventricular fibroblasts (cFBs) (Lonza, Basel, Switzerland) were cultured in FGM-3 media (Lonza) were used at passage 3-4 for spheroid/organoid fabrication. Human umbilical vein endothelial cells (HUVECs) (Lonza) were cultured in EGM-2 media (Lonza) and were used at passage 2-3 for spheroid/organoid fabrication. Human adipose-derived microvascular endothelial cells (HAMECs) (kind gift from Dr. Michael Yost) and were cultured in EGM-2 media (Lonza) and were used at passage 5-6 for organoid fabrication. Human adipose-derived stem cells (hADSCs) (Lonza) were cultured in low glucose Dulbecco's modified Eagle's medium with 10% fetal bovine serum (FBS) and 1% penicillin-streptomycin, 1% glutamine and 1% antimycin (Gibco Life Technologies, Grand Island, NY). hADSCs were used at passage 3-4 for spheroid/organoid fabrication. For cFBs, hADSCs, and HUVECs, media was changed every 2 days and were

passaged using tryPLE Express (Gibco) at >80% confluency. An array of media were evaluated to best support consistent organoid formation and culture, shown in Figure 3.17. The optimal culture media for viable cardiac organoids was comprised of a ratiometric combination of cell-specific media reflecting the cell ratio of the organoid. In organoid media, CDI hiPSC-CM Maintenance Media (supplied without glucose) was substituted with glucose-containing DMEM/F12 media with 10% FBS and 1% non-essential amino acids (Gibco).

*Organoid and spheroid fabrication.* As described in our previous publication<sup>45</sup>, the agarose hydrogel molds were prepared using 2% agarose (Sigma Aldrich, St. Louis, MO) and master micro-molds from Microtissues, Inc (Providence, RI) as negative replicates to create non-adhesive agarose hydrogels molds containing 35 microwells with hemispheric bottoms (800  $\mu\text{m}$  diameter, 800  $\mu\text{m}$  deep) to facilitate the formation of spherical microtissues. Molds were soaked in cell/organoid specific media prior to microtissue fabrication. Working cell suspensions of each cell type were used at  $\sim 4.0 \times 10^6$  cells/mL to make organoid cell ratio mixtures and mixed with 1 volume media for a final concentration of  $\sim 2.0 \times 10^6$  cells/mL. Approximately 75  $\mu\text{L}$  of the cell suspension was pipetted into each agarose mold. After the cells settled into the recesses of the mold (10 min), additional media was added to submerge the molds in an 8-well plate and exchanged every 2 days for the length of the experiment (10 days). Day 0 (D0) of the experiment was marked after 4 days of spheroid assembly. A scheme of the experimental

timeline can be found in Figure 3.8. TUNEL staining for apoptotic nuclei revealed that D0 cardiac organoids maintained high viability throughout the microtissue (Figure 3.10).

*Contraction analysis of beating spheroids.* Videos of spontaneously beating spheroids from each group were recorded at ~37 °C for each condition using a Carl Zeiss Axiovert A1 Inverted Microscope and Zen 2011 software (Zeiss, Göttingen, Germany). Videos were converted to a series of TIFF format pictures by Adobe Premiere (Adobe, San Jose, CA). Threshold edge-detecting in ImageJ software (National Institutes of Health) was used on high contrast spheroid picture series and graphed to realize beating profiles of fractional area change (i.e., contraction amplitude), from which beats per minute and contraction amplitude was calculated. Contraction amplitudes were calculated as the percent change in fractional area change amplitude between contraction and relaxation.

*Immunofluorescent analysis.* Freshly collected spheroids were flash frozen in Tissue-Tek OCT compound (Sakura, Torrance, CA). Embedded spheroids were cryosectioned into 7 µm sections onto glass slides. The sections were fixed with cooled acetone (-20 °C) for 10 min. After washing (2 times at 5 min) in PBS with 0.1% Triton X-100 (PBST) (Sigma), blocking buffer was made with 10% serum corresponding to host species of secondary antibody in PBST and added to sections for 1 hr at room temperature. Sections were incubated with primary antibody diluted in PBST (1:200) overnight at 4 °C or 2 hrs at room temperature: rabbit anti-laminin (Sigma), rabbit-anti collagen type I (Abcam), rabbit anti-fibronectin (Abcam), mouse anti-alpha sarcomeric actinin (Abcam), rabbit anti-cardiac troponin I – cTnI (Abcam), rabbit anti-MYL2 (MLC-2v)

(Abcam), rabbit anti-vimentin (Abcam), mouse anti-CD31 (BD Biosciences, San Jose, CA), rabbit anti-von Willebrand factor (vWF) (Abcam). After washing in PBST (2 times at 5 min), sections were incubated with complement secondary antibodies diluted in PBST for 1 hr at room temperature: goat anti-mouse Alexa Fluor 546 (Thermo), goat anti-rabbit Alexa Fluor 647 (Jackson ImmunoResearch, West Grove, PA). After washing in PBST (2 times at 5 min), nuclei were counterstained with DAPI (Molecular Probes/Invitrogen, Eugene, OR) diluted in PBST for 15 min at room temperature. Following the final wash procedure (PBST, 2 times at 5 min), glass cover slips were added to the slides using Fluoro-Gel (Electron Microscopy Sciences, Hatfield, PA). TCS SP5 AOBS laser scanning confocal microscope (Leica Microsystems, Inc., Exton, PA) was used for imaging. Imaris software (Bitplane, Zurich, Switzerland) was used to reconstruct z-stacked confocal images for 3D visualization. Fluorescent protein expression was calculated as the antibody-positive fluorescence area coverage: endothelial density was calculated as vWF-positive covered area divided by spheroid area, lumens per organoid was calculated as the number of vWF-positive ring-shaped structures with adjacent DAPI-stained nuclei per organoid, vimentin density was the ratio of vimentin-positive area within the  $\alpha$ -SA-positive area, ECM fraction area was calculated as the ECM-stain positive area divided by the spheroid area, and the relative contractile protein amount was calculated as the ratio of cTnI or MLC-2v area to total  $\alpha$ -SA covered area. Each analysis consisted of high resolution images at 400X total magnification of 3-5 spheroids. Hematoxylin and eosin-stained embryonic mouse heart sections were a kind gift from the lab of Dr. Russell Norris.

*TUNEL staining for apoptosis.* Roche In Situ Cell Death Detection Kit (Sigma) was used to visualize the viability of cells in frozen sections of cardiac organoids based on the Roche protocol. Briefly, cardiac organoid frozen sections were fixed with 4% paraformaldehyde in PBS for 20 min at room temperature. Following washing in PBS for 30 minutes, samples were incubated in a permeabilization solution (0.1% Triton X-100 and 0.1% sodium citrate in PBS) for 2 minutes on ice. Then 50 µl of the TUNEL reaction mixture were added to samples and incubated at 37 °C for 1 hr. After washing in PBS (2 times at 5 min), nuclei were counterstained with DAPI (Molecular Probes/Invitrogen) diluted in PBS for 15 min at ambient temperature. Following the final wash procedure (PBS, 2 times at 5 min), glass cover slips were added to the slides using Fluoro-Gel (Electron Microscopy Sciences). TCS SP5 AOBS laser scanning confocal microscope (Leica Microsystems) was used for imaging. TUNEL-based viability index was calculated as  $[1 - (\text{TUNEL-positive area} / \text{DAPI-positive area})]$ .

*Gene expression with qRT-PCR.* Total RNA was isolated according to the kit and protocol of an RNeasy Micro Kit (Qiagen, Vinlo, Netherlands) with the addition of the Homogenizer Columns (Omega Biotek, Norcross, GA) during the homogenization step for spheroids. For each group, a minimum of 10 spheroids were used for RNA isolation. At least 25 ng of total RNA for each group was subjected to cDNA synthesis using the Bio-Rad (Hercules, USA) iScript cDNA synthesis kit. qRT-PCR step was performed using validated Life Technologies Taqman primers (Thermo Fisher Scientific) in 10 µl reactions for targeted genes: ACTB (Hs01060665\_g1), GAPDH (Hs02758991\_g1), IL6



(Hs00985639\_m1), KDR (VEGFR2, Hs00911700\_m1), MYL2 (Hs00166405\_m1), MYL7 (Hs01085598\_g1), TNNT1 (Hs00913333\_m1), TNNT3 (Hs00165957\_m1), VEGFA (Hs00900055\_m1). Data was normalized as the change in cycle threshold (Ct) to the geometric mean of GAPDH and ACTB (dCt) and analyzed using, mRNA expression =  $2^{(-dCt)}$ . Data was then averaged across n=3 experiments.

*Calcium transient imaging.* Life Technologies's Fluo-4 Direct Calcium Assay Kit (Life Technologies, Carlsbad, CA) was used to label calcium in the whole organoids based on the manufacturer protocol. Briefly, organoids stained with a working solution of 1:1 calcium dye solution to media and incubated at 37 °C, 5% CO<sub>2</sub>, 20% O<sub>2</sub> for 30 min. Carl Zeiss Axiovert A1 Inverted Microscope completed with GFP fluorescence imaging capacity (Zeiss) was used to collect the videos of the calcium transient of whole spheroids with a capture rate of 20 frames per second. Finally, we used Zen 2011 software (Zeiss) to convert videos to a series of TIFF format pictures. Mean gray value of the whole organoid calcium transient (controlled for area for pre- and post- treatment) was measured using ImageJ software (National Institutes of Health) to construct calcium transient profiles. Normalized  $F/F_0$  was calculated as the peak calcium fluorescence (F) divided by the start fluorescence level ( $F_0$ ), then divided by the  $F/F_0$  of the baseline transient before treatment. Time to peak calcium (sec) was calculated as the difference in time between the peak calcium and the start of the calcium transient. Time to 50% calcium decay (sec) was calculated as the difference in time between the start of the calcium transient and the half-peak ( $F_{50}$ ) of the calcium decay.

*Evaluation of putative vasculature.* Oxygen reduction studies were performed at 10% O<sub>2</sub> in a hypoxia chamber (C-Chamber, BioSpherix, Parish, NY) for a duration of 10 days. Media was exchanged every 2 days. Microtissues were embedded in OCT, cryosectioned, and Roche In Situ Cell Death Detection Kit (Sigma) was used to visualize the viability of cells in frozen sections of cardiac organoids based on the Roche protocol. Macrotissue assembly was performed in agarose-coated (non-adhesive) 96-well plates. Five cardiac organoids (developing stage cell ratio) were placed in each well and culture for 10 days until the macrotissues had an appreciable Z-dimension, observed by pipette agitation. Organoid aggregate macrotissues were embedded in OCT and cryosectioned for immunofluorescent analysis. Media was exchanged every day.

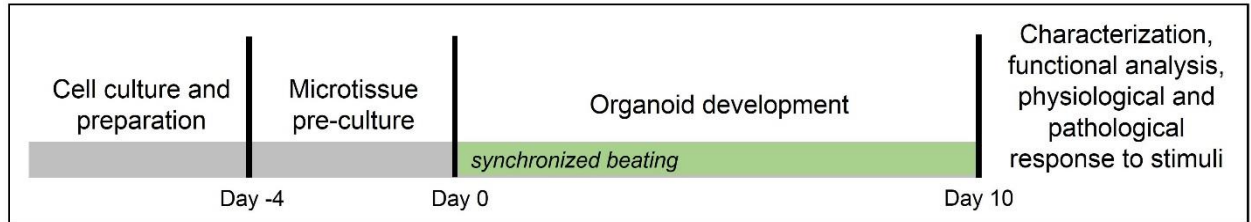
*Pharmacological, physiological, and pathological stimulus.* Pharmacological compounds were used to block channels of human cardiac organoids and were performed on single organoids in ultra low-adhesive GravityTRAP Plates (InSphero, Schlieren, Switzerland) at 37 °C. Freshly prepared stock solutions of verapamil (Sigma), ryanodine, and E-4031 were diluted in the calcium buffer provided in the calcium staining kit (Life Technologies). Verapamil (0.5 µM), ryanodine (50 µM), and E-4031 (10 µM) added to the organoids and calcium signal was video captured after 20 mins. Isoproterenol (1 µM) was added for 10 mins before bright field videos were captured. For ischemic stimulus, microtissues were rinsed in low glucose DMEM (1 g/L) (Gibco) and placed in agarose molds in serum-free, low glucose (1 g/L) DMEM and 1% O<sub>2</sub> (BioSpherix) for 6 hrs

to examine the initial response. Controls were cultured at normoxia in cell/organoid-specific media.

*Statistics Analysis.* Differences between experimental groups were analyzed on JMP Pro 12 Statistical software (SAS, Cary, NC) using Student's t-test, matched pairs comparison, one-way ANOVA, and two-way ANOVA with Tukey's post-hoc test, and  $p < 0.05$  was considered significantly difference for all statistical tests.

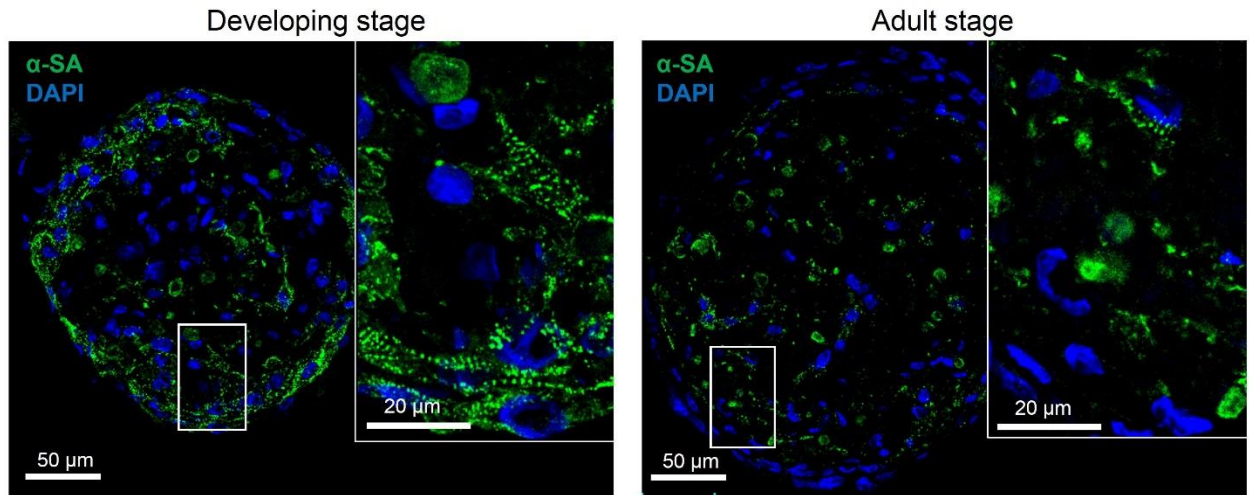
## Supporting Information

Figure 3.8.



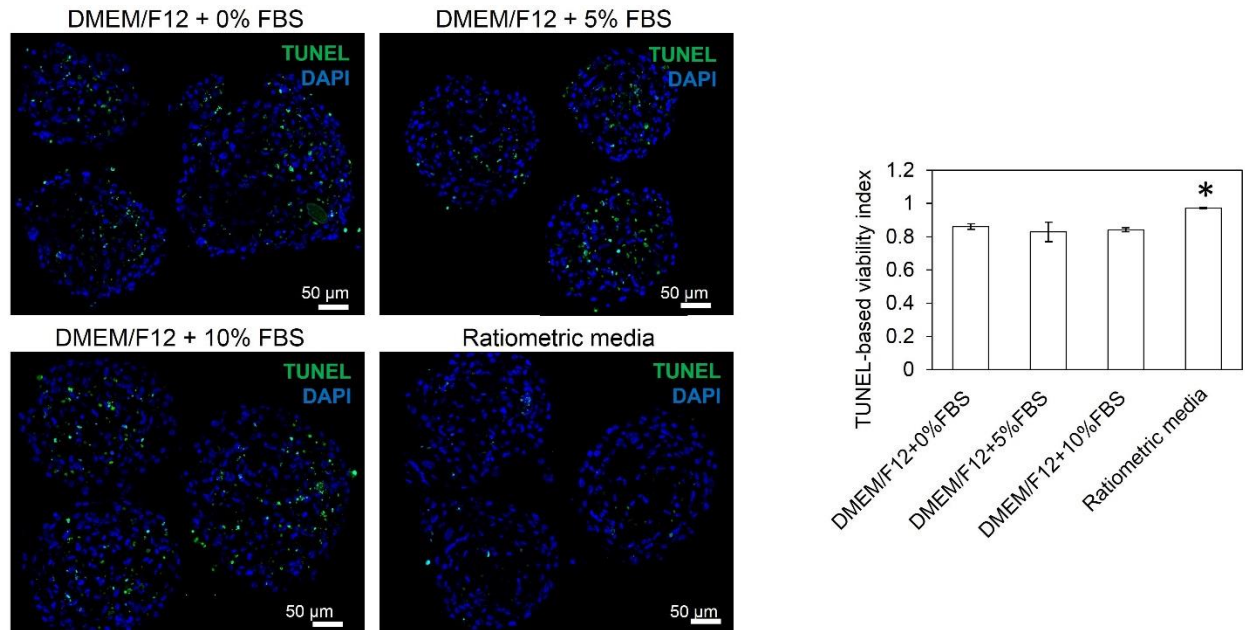
**Figure 3.8.** Experimental timeline of human cardiac organoids. Microtissues (cell type-specific spheroids and cardiac organoids) were pre-cultured for 4 days until experimental Day 0 (D0). Human cardiac organoids began synchronized, spontaneous beating on D0 and continued throughout the length of the experiment. Microtissues were collected for analysis on D10.

Figure 3.9.



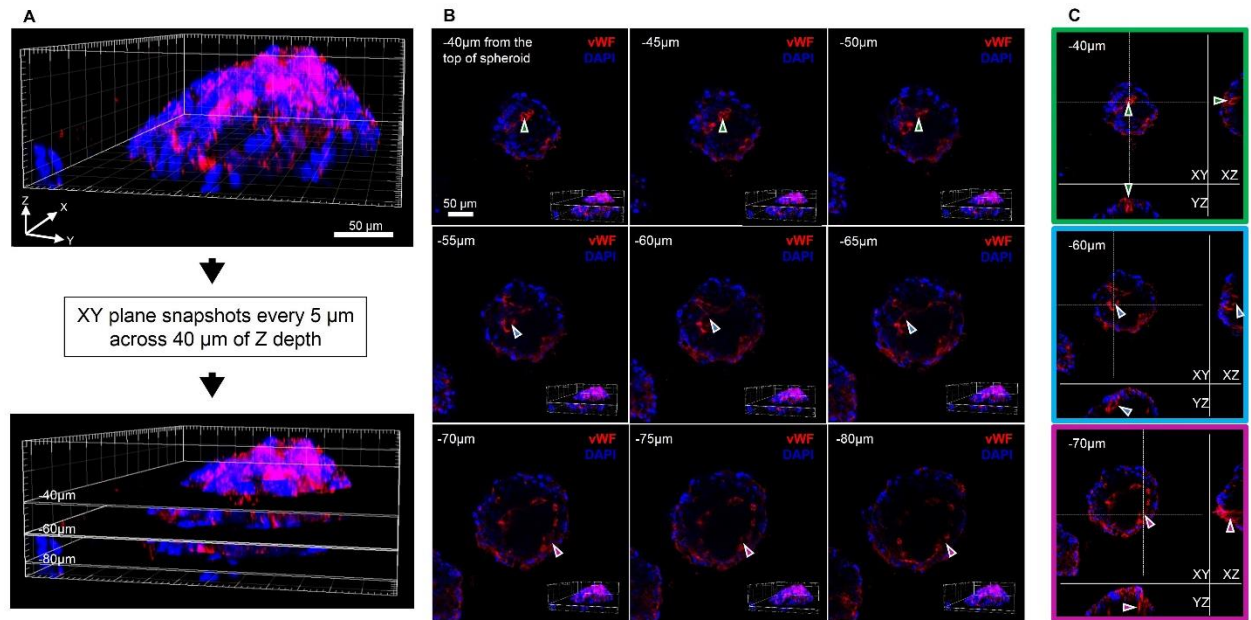
**Figure 3.9.** The ratio of cells in cardiac organoids influences contractile development. Developing stage ratio organoids, which contains more cardiomyocytes, supported improved sarcomere formation ( $\alpha$ -SA-positive with sarcomeric banding) in contrast to adult stage ratio organoids at D10 ( $\alpha$ -SA-positive without sarcomeric banding); green-alpha sarcomeric actinin ( $\alpha$ -SA), blue-DAPI.

Figure 3.10.



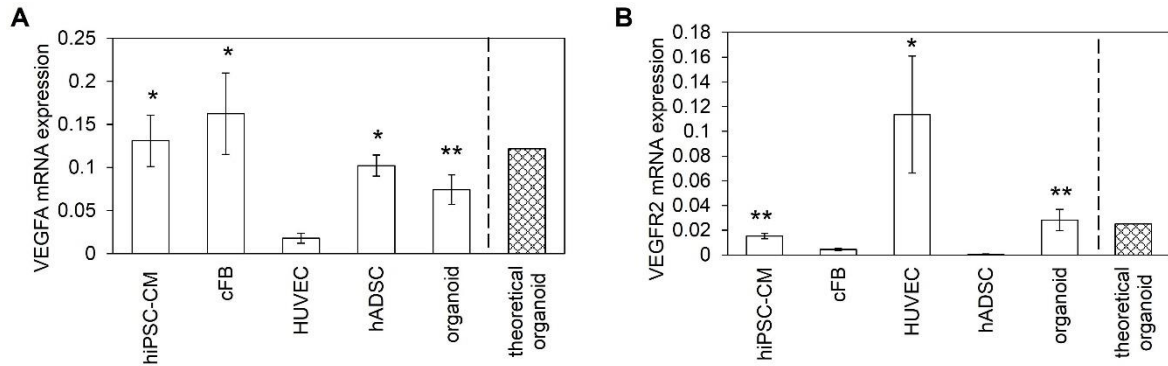
**Figure 3.10.** Culture media screening using TUNEL staining (green) for apoptotic nuclei of D0 cardiac organoids showed significantly better viability index throughout the microtissues using ratiometric media compared to DMEM/F12 with FBS cultured; n=3-4 organoids. The ratiometric media was a combination of cardiomyocyte media (DMEM/F12, 10% FBS, 1% non-essential amino acids), fibroblast media (Lonza FGM-3), and endothelial cell media (Lonza EGM-2) corresponding to the developing cell ratio. Blue – DAPI nuclear stain. Cardiac organoids with a developing stage cell ratio were used for media screening. Asterisk represents significant difference with control,  $p < 0.05$ .

Figure 3.11.



**Figure 3.11.** Confocal imaging of immunofluorescently stained whole cardiac organoids (D10) show lumenized vascular network. (A) Method schematic shows that large Z-stack confocal images were collected; serial images were taken every 5 µm across 40 µm of Z depth. (B) Serial vWF (red) and DAPI (blue) images (XY plane) every 5 µm starting at 40 µm from the top of the spheroids show endothelial cell organization. Arrows indicate regions showing lumen-like structures in X, Y, and Z perspectives seen in (C). Cardiac organoids were fabricated using a developing stage cell ratio.

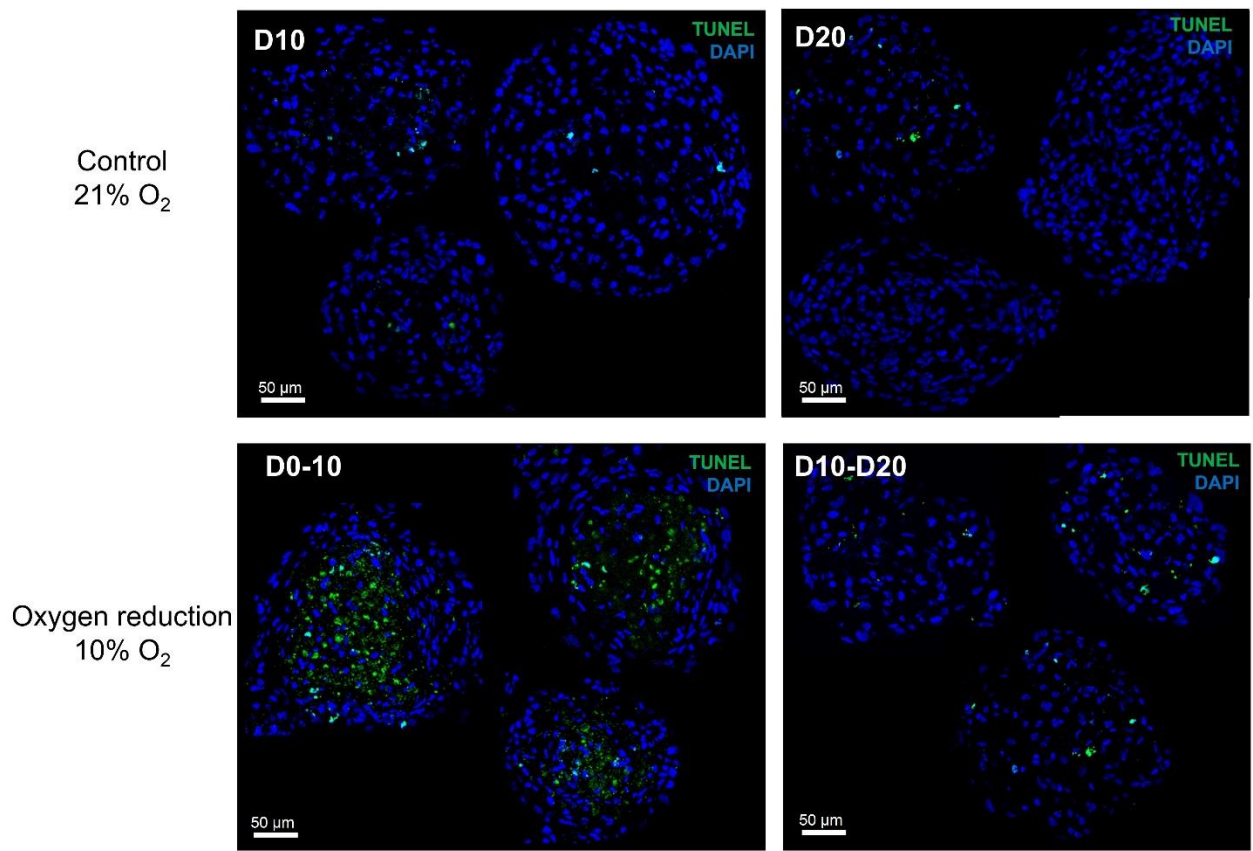
Figure 3.12.



**Figure 3.12.** Analysis of individual cell types and cardiac organoids regulation of angiogenic gene expression in human cardiac organoids at D10. (A) VEGFA gene expression in cardiac organoids was significantly lower than spheroids of hiPSC-CMs, cFBs, and hADSCs alone, and significantly higher than that of HUVECs. (B) HUVECs showed significantly higher levels of VEGFR2 gene expression than all other groups, while cardiac organoids and hiPSC-CMs showed higher expression than cFBs and ADSCs. Differences in VEGFA expression between organoids and a ratiometric theoretical organoid suggested self-regulation of VEGFA signaling between VEGF providers (hiPSC-CMs, cFBs, hADSCs) and VEGF receivers (HUVECs). Theoretical organoid expression levels were calculated based on ratiometric combination of gene expression of the organoid ratio of cell types (50% hiPSC-CM, 29% cFBs, 14% HUVECs, and 7% hADSCs). Cardiac organoids were fabricated using a developing stage cell ratio; n=3 experiments; 10-15 microtissues/experiment. hiPSC-CM-human induced pluripotent stem cell-derived cardiomyocyte, cFB-human adult ventricular cardiac fibroblast, HUVEC-human umbilical vein endothelial cell, hADSC-human adipose-derived stem cell. \* significantly higher than remaining, \*\* significantly different than remaining,  $p < 0.05$ .

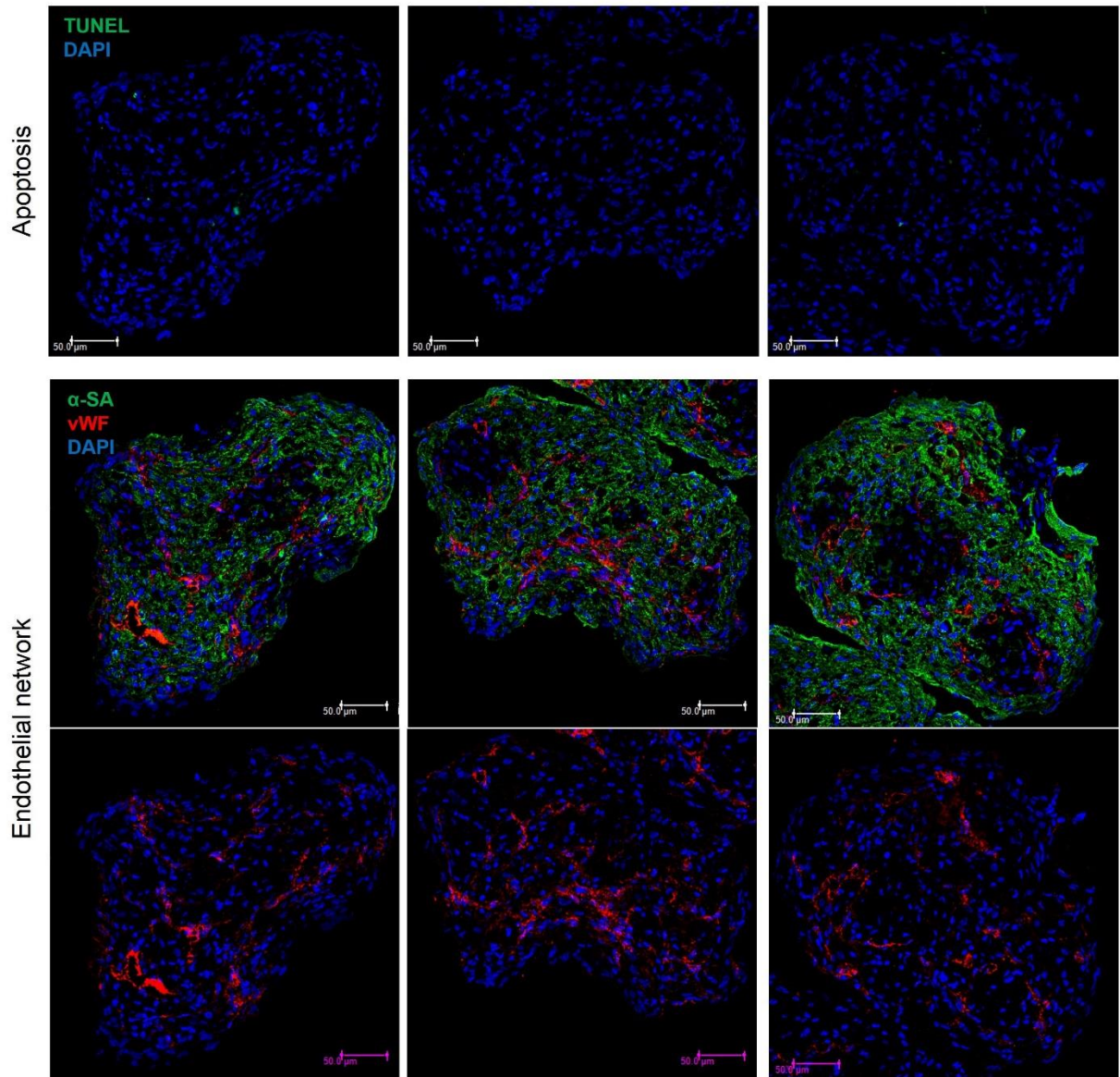


Figure 3.13.



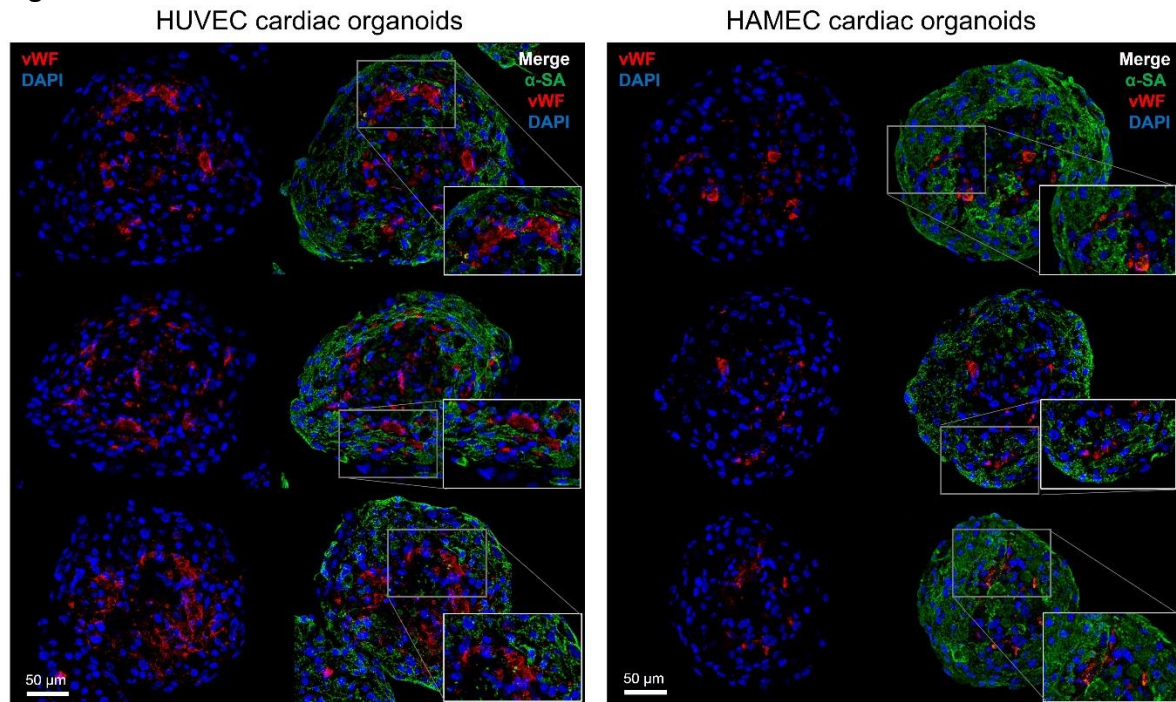
**Figure 3.13.** Evaluation of putative vasculature using an oxygen-reduced environment. Cardiac organoids were placed in 21% O<sub>2</sub> (control) or 10% O<sub>2</sub> (oxygen reduction) starting at D0 until D10 (D0-D10; before formation of putative vasculature) or D10 until D20 (D10-D20; after formation of putative vasculature). Compared to time-matched controls at D10 and D20 and vascularized organoids with oxygen reduction, cardiac organoids without putative vasculature under oxygen reduction showed high presence of TUNEL apoptosis staining (green); blue-DAPI nuclear stain. Cardiac organoids were fabricated using a developing stage cell ratio.

Figure 3.14.



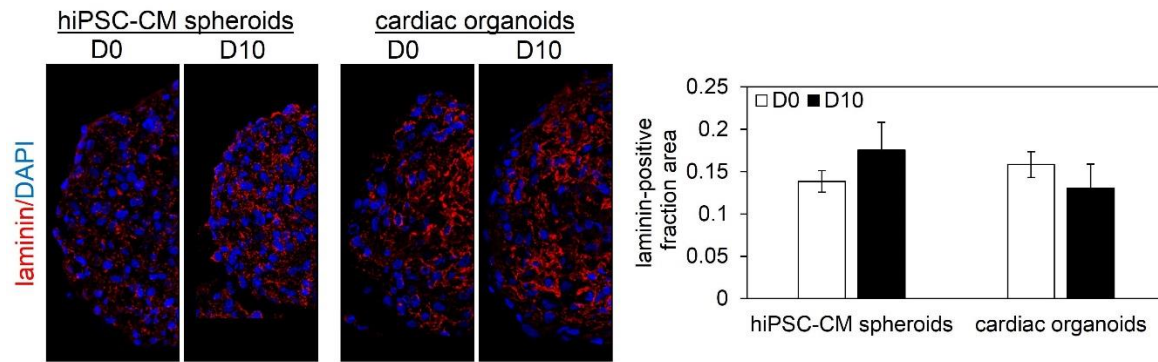
**Figure 3.14.** Evaluation of putative vasculature using macro-tissue assembly. After 10 days of aggregation of five D10 cardiac organoids, the macro-tissue reached dimensions beyond the oxygen tension range of a 100-200 μm radius micro-tissues. Across all repeats, there were minimal TUNEL-positive apoptotic nuclei (green); blue-DAPI. Endothelial vWF-positive (red) staining showed extensive regions of connected, immunostained endothelial cells (i.e., networks) across the newly formed macro-tissue. Green-alpha sarcomeric actinin, α-SA. Cardiac organoids were fabricated using a developing stage cell ratio.

Figure 3.15.



**Figure 3.15.** Endothelial cell source affect structural functionality. Cardiac organoids made with human umbilical vein endothelial cells (HUVECs) at a developing stage cell ratio with human adipose-derived stem cells (hADSCs) show consistently higher density of vWF-positive (red) cells on D10 compared to cardiac organoids made with human adipose-derived microvascular endothelial cells (HAMECs) at the same ratio, while cardiomyocyte organization (green, alpha sarcomeric actinin  $\alpha$ -SA-positive) is consistent between organoids. Both HUVECs and HAMECs show evidence of endothelial network formation (inset).

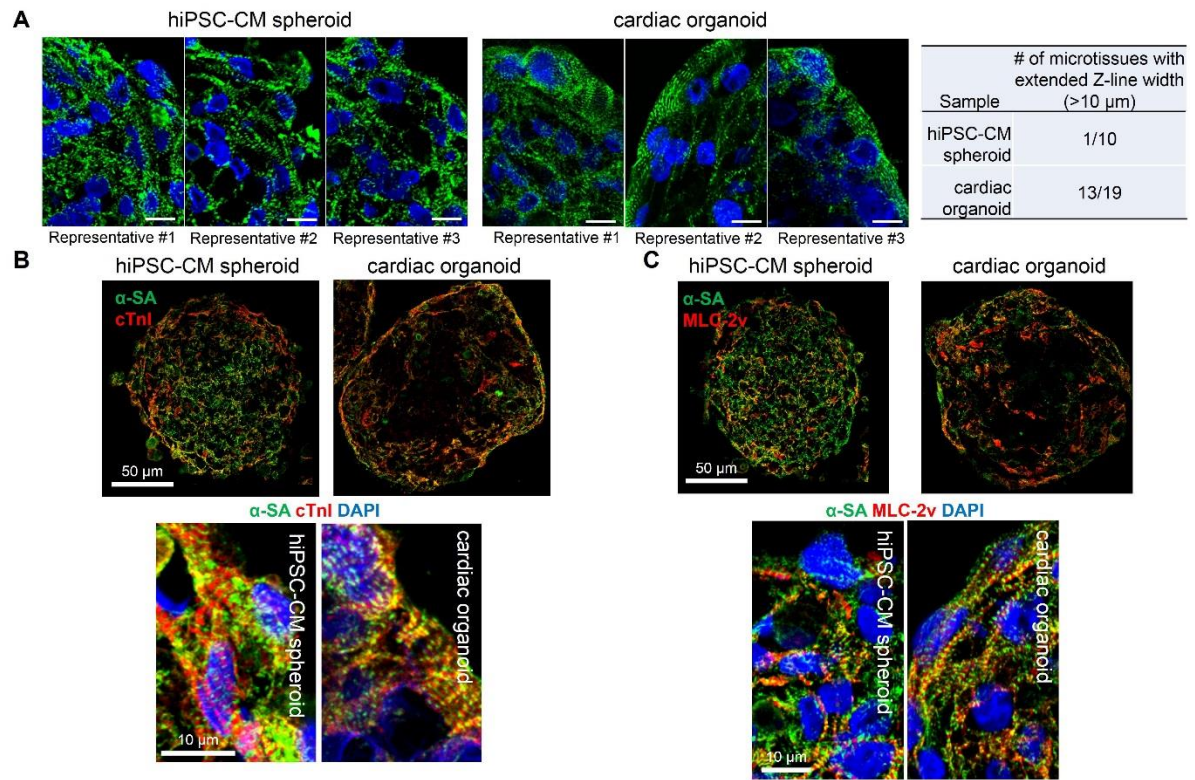
Figure 3.16.



**Figure 3.16.** Both hiPSC-CM spheroids and cardiac organoids showed immunofluorescent expression of laminin that did not change significantly over time. Quantification of ECM components was based on the ratio of ECM-positive covered area divided by total spheroid area; n=3-6 microtissues. Cardiac organoids with a developing stage cell ratio were used for media screening. hiPSC-CM-human induced pluripotent stem cell-derived cardiomyocyte.

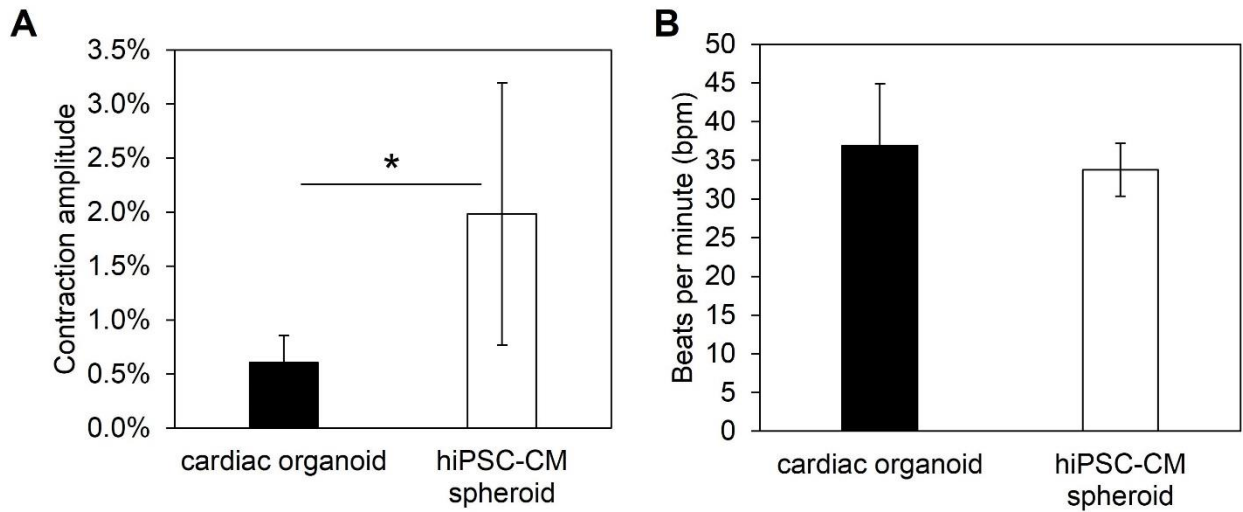


Figure 3.17.



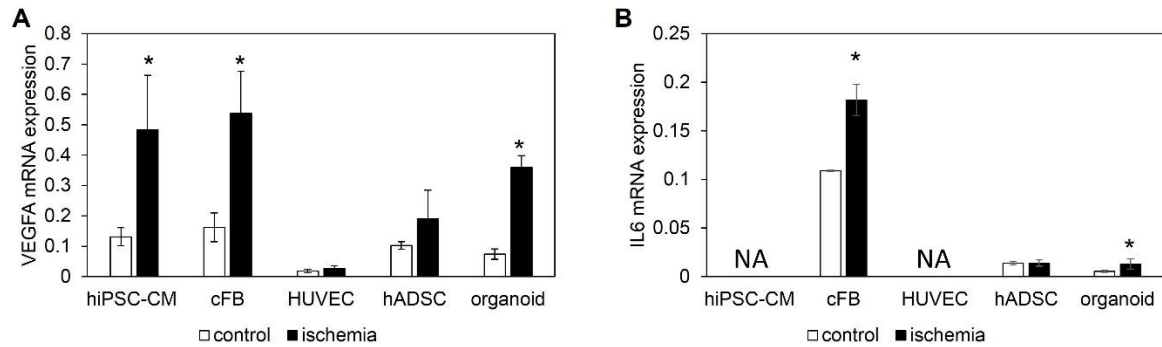
**Figure 3.17.** Human cardiac organoids support contractile development of hiPSC-CMs. (A) Cardiac organoids at D10 showed a higher occurrence of the observed extended Z-line width (> 10  $\mu$ m) across different spheroids and experiments. hiPSC-CM spheroids: n=3 experiments; cardiac organoids: n=5 experiments. (B) Cardiac organoids showed increased adult cardiac troponin I (cTnI)-positive and (C) ventricular myosin light chain (MLC-2v)-positive fraction area over  $\alpha$ -sarcomeric actinin ( $\alpha$ -SA)-positive area (hiPSC-CM-specific areas) at D10, represented by low and high magnification immunofluorescent images, n=3 microtissues. hiPSC-CM-human induced pluripotent stem cell-derived cardiomyocyte. Cardiac organoids were fabricated using a developing stage ratio of cells.

Figure 3.18.



**Figure 3.18.** Functional analysis of human cardiac organoids and hiPSC-CM spheroids. (A) At D10, cardiac organoids showed a significantly lower contraction amplitude (i.e., fractional area change) than spheroids of 100% hiPSC-CM (hiPSC-CM spheroids); n=28-41 microtissues. (B) Cardiac organoids and hiPSC-CM spheroids showed similar beat rates (beats per minute) on D10; n=23-31 microtissues. Cardiac organoids were fabricated using a developing stage cell ratio. Asterisk represents significant difference,  $p < 0.05$ .

Figure 3.19.



**Figure 3.19.** Response of individual cell types to ischemia on D10. (A) hiPSC-CM and cFB spheroids showed significant increases in VEGFA gene expression in response to 6 hrs of ischemia (1 g/L glucose, serum-free, 1% O<sub>2</sub>), contributing to the significant increase in cardiac organoid expression. (B) cFB-only spheroids showed significant increase in IL6 gene expression. Cardiac organoids were fabricated using a developing stage cell ratio; n=3 experiments; 10-15 microtissues/experiment. Asterisk represents significant difference with control, p < 0.05.

## CHAPTER FIVE

### FUTURE DIRECTION AND OUTLOOK

The development of biomimetic models for cardiac tissue requires the appropriate understanding of the biological system and necessary strategies to recapitulate those processes. Throughout this exploration, I gained a unique perspective into multiple dimensions of biomimicry, from extracellular matrix interactions, to electrically compatible strategies, and mechanisms of multi-cellular self-assembly. With an understanding of the strengths of each biomimetic approach, these strategies can be leveraged for applications in basic research, drug discovery, and cell therapy. As heart failure poses an imminent challenge to human health, future directions will consist of adapting these approaches to enhance our understanding of cardiac tissue physiology and self-assembly, to model cardiac pathological conditions, and to advance the current cell delivery vehicle for heart repair.

The exploration presented here contributes to the growing knowledge of scaffold-based and scaffold-free tissue-engineered constructs. With extracellular matrix remodeling being a hallmark of heart failure pathology, the use of tunable materials, such as functionalized alginate or electrically conductive silicon nanowires, may provide an adaptable tool to investigate microenvironment-dependent changes in cell behavior. Furthermore, given the heterogeneous cell-cell interactions, a multicellular 3D cardiac organoid model not only provides a robust platform to investigate the role of individual cells but also provides a tissue-level perspective that incorporates innumerable variables,



such as synergistic signaling mechanisms between cells, to more accurately model the complex multicellular environment of heart tissue. This avoids false-positive results from single cell or 2D systems that are later counteracted, for example, by inhibitory signaling from other cell types within a tissue/organisms. In the end, improvements in the treatment of heart failure depends on relevant and accurate models. Pursuing a better in vitro cardiac tissue model using hiPSC technology will allow for a humanized, personalized model that can avoid the disadvantages of single cell systems and translational discrepancies of animal studies for the next generation of cardiovascular research.

## REFERENCES

- 1 Heron, M. *et al.* Deaths: final data for 2006. *National vital statistics reports : from the Centers for Disease Control and Prevention, National Center for Health Statistics, National Vital Statistics System* **57**, 1-134 (2009).
- 2 Roger, V. L. *et al.* Heart disease and stroke statistics--2011 update: a report from the American Heart Association. *Circulation* **123**, e18-e209, doi:10.1161/CIR.0b013e3182009701 (2011).
- 3 Baroldi, G. Acute coronary occlusion as a cause of myocardial infarct and sudden coronary heart death. *Am J Cardiol* **16**, 859-880 (1965).
- 4 Roberts, W. C. Coronary arteries in fatal acute myocardial infarction. *Circulation* **45**, 215-230 (1972).
- 5 Fulton, W. F. Pathological concepts in acute coronary thrombosis: relevance to treatment. *Br Heart J* **70**, 403-408 (1993).
- 6 Kikuchi, K. & Poss, K. D. Cardiac regenerative capacity and mechanisms. *Annu Rev Cell Dev Biol* **28**, 719-741, doi:10.1146/annurev-cellbio-101011-155739 (2012).
- 7 Laflamme, M. A. *et al.* Cardiomyocytes derived from human embryonic stem cells in pro-survival factors enhance function of infarcted rat hearts. *Nature biotechnology* **25**, 1015-1024, doi:10.1038/nbt1327 (2007).
- 8 Mignone, J. L., Kreutziger, K. L., Paige, S. L. & Murry, C. E. Cardiogenesis from human embryonic stem cells. *Circulation journal : official journal of the Japanese Circulation Society* **74**, 2517-2526 (2010).
- 9 Hirt, M. N., Hansen, A. & Eschenhagen, T. Cardiac tissue engineering: state of the art. *Circulation research* **114**, 354-367, doi:10.1161/CIRCRESAHA.114.300522 (2014).
- 10 Liao, B., Zhang, D. & Bursac, N. Functional cardiac tissue engineering. *Regenerative medicine* **7**, 187-206, doi:10.2217/rme.11.122 (2012).
- 11 Vunjak-Novakovic, G. *et al.* Challenges in cardiac tissue engineering. *Tissue engineering. Part B, Reviews* **16**, 169-187, doi:10.1089/ten.TEB.2009.0352 (2010).
- 12 Prowse, A. B. *et al.* Transforming the promise of pluripotent stem cell-derived cardiomyocytes to a therapy: challenges and solutions for clinical trials. *The Canadian journal of cardiology* **30**, 1335-1349, doi:10.1016/j.cjca.2014.08.005 (2014).
- 13 Barad, L., Schick, R., Zeevi-Levin, N., Itskovitz-Eldor, J. & Binah, O. Human embryonic stem cells vs human induced pluripotent stem cells for cardiac repair. *The Canadian journal of cardiology* **30**, 1279-1287, doi:10.1016/j.cjca.2014.06.023 (2014).

- 14 Chong, J. J. *et al.* Human embryonic-stem-cell-derived cardiomyocytes regenerate non-human primate hearts. *Nature*, doi:10.1038/nature13233 (2014).
- 15 Lian, X. *et al.* Robust cardiomyocyte differentiation from human pluripotent stem cells via temporal modulation of canonical Wnt signaling. *Proceedings of the National Academy of Sciences of the United States of America*, doi:10.1073/pnas.1200250109 (2012).
- 16 Burridge, P. W. *et al.* Chemically defined generation of human cardiomyocytes. *Nature methods* **11**, 855-860, doi:10.1038/nmeth.2999 (2014).
- 17 Ye, L. *et al.* Cardiac repair in a porcine model of acute myocardial infarction with human induced pluripotent stem cell-derived cardiovascular cells. *Cell stem cell* **15**, 750-761, doi:10.1016/j.stem.2014.11.009 (2014).
- 18 Zwi-Dantsis, L. *et al.* Derivation and cardiomyocyte differentiation of induced pluripotent stem cells from heart failure patients. *European heart journal* **34**, 1575-1586, doi:10.1093/eurheartj/ehs096 (2013).
- 19 Bolli, R. *et al.* Myocardial protection at a crossroads: the need for translation into clinical therapy. *Circulation research* **95**, 125-134, doi:10.1161/01.RES.0000137171.97172.d7 (2004).
- 20 Gheorghiade, M. *et al.* Developing New Treatments for Heart Failure: Focus on the Heart. *Circulation. Heart failure* **9**, doi:10.1161/CIRCHEARTFAILURE.115.002727 (2016).
- 21 Nunes, S. S. *et al.* Biowire: a platform for maturation of human pluripotent stem cell-derived cardiomyocytes. *Nature methods* **10**, 781-787, doi:10.1038/nmeth.2524 (2013).
- 22 Lundy, S. D., Zhu, W. Z., Regnier, M. & Laflamme, M. A. Structural and Functional Maturation of Cardiomyocytes Derived from Human Pluripotent Stem Cells. *Stem cells and development*, doi:10.1089/scd.2012.0490 (2013).
- 23 Lieu, D. K. *et al.* Mechanism-based facilitated maturation of human pluripotent stem cell-derived cardiomyocytes. *Circ Arrhythm Electrophysiol* **6**, 191-201, doi:10.1161/CIRCEP.111.973420 (2013).
- 24 van den Heuvel, N. H., van Veen, T. A., Lim, B. & Jonsson, M. K. Lessons from the heart: mirroring electrophysiological characteristics during cardiac development to in vitro differentiation of stem cell derived cardiomyocytes. *Journal of molecular and cellular cardiology* **67**, 12-25, doi:10.1016/j.yjmcc.2013.12.011 (2014).
- 25 Kensah, G. *et al.* Murine and human pluripotent stem cell-derived cardiac bodies form contractile myocardial tissue in vitro. *European heart journal* **34**, 1134-1146, doi:10.1093/eurheartj/ehs349 (2013).
- 26 Zhang, D. *et al.* Tissue-engineered cardiac patch for advanced functional maturation of human ESC-derived cardiomyocytes. *Biomaterials* **34**, 5813-5820, doi:10.1016/j.biomaterials.2013.04.026 (2013).

- 27 Mihic, A. *et al.* The effect of cyclic stretch on maturation and 3D tissue formation of human embryonic stem cell-derived cardiomyocytes. *Biomaterials*, doi:10.1016/j.biomaterials.2013.12.052 (2014).
- 28 Desroches, B. R. *et al.* Functional scaffold-free 3-D cardiac microtissues: a novel model for the investigation of heart cells. *American journal of physiology. Heart and circulatory physiology* **302**, H2031-2042, doi:10.1152/ajpheart.00743.2011 (2012).
- 29 Kelm, J. M. *et al.* Design of artificial myocardial microtissues. *Tissue Eng* **10**, 201-214, doi:10.1089/107632704322791853 (2004).
- 30 Yang, X., Pabon, L. & Murry, C. E. Engineering adolescence: maturation of human pluripotent stem cell-derived cardiomyocytes. *Circulation research* **114**, 511-523, doi:10.1161/CIRCRESAHA.114.300558 (2014).
- 31 Reinecke, H., Zhang, M., Bartosek, T. & Murry, C. E. Survival, integration, and differentiation of cardiomyocyte grafts: a study in normal and injured rat hearts. *Circulation* **100**, 193-202 (1999).
- 32 Bian, W., Badie, N., Himel, H. D. t. & Bursac, N. Robust T-tubulation and maturation of cardiomyocytes using tissue-engineered epicardial mimetics. *Biomaterials* **35**, 3819-3828, doi:10.1016/j.biomaterials.2014.01.045 (2014).
- 33 Radisic, M. *et al.* Biomimetic approach to cardiac tissue engineering: oxygen carriers and channeled scaffolds. *Tissue Eng* **12**, 2077-2091, doi:10.1089/ten.2006.12.2077 (2006).
- 34 Feric, N. T. & Radisic, M. Maturing human pluripotent stem cell-derived cardiomyocytes in human engineered cardiac tissues. *Adv Drug Deliv Rev* **96**, 110-134, doi:10.1016/j.addr.2015.04.019 (2016).
- 35 Hirt, M. N. *et al.* Functional improvement and maturation of rat and human engineered heart tissue by chronic electrical stimulation. *Journal of molecular and cellular cardiology* **74**, 151-161, doi:10.1016/j.yjmcc.2014.05.009 (2014).
- 36 Godier-Furnemont, A. F. *et al.* Physiologic force-frequency response in engineered heart muscle by electromechanical stimulation. *Biomaterials* **60**, 82-91, doi:10.1016/j.biomaterials.2015.03.055 (2015).
- 37 Radisic, M. *et al.* Functional assembly of engineered myocardium by electrical stimulation of cardiac myocytes cultured on scaffolds. *Proceedings of the National Academy of Sciences of the United States of America* **101**, 18129-18134, doi:10.1073/pnas.0407817101 (2004).
- 38 Baumgartner, S. *et al.* Electrophysiological and morphological maturation of murine fetal cardiomyocytes during electrical stimulation in vitro. *Journal of cardiovascular pharmacology and therapeutics* **20**, 104-112, doi:10.1177/1074248414536273 (2015).
- 39 Eng, G. *et al.* Autonomous beating rate adaptation in human stem cell-derived cardiomyocytes. *Nature communications* **7**, 10312, doi:10.1038/ncomms10312 (2016).

- 40 Tandon, N. *et al.* Optimization of electrical stimulation parameters for cardiac tissue engineering. *Journal of tissue engineering and regenerative medicine* **5**, e115-125, doi:10.1002/term.377 (2011).
- 41 Tandon, N. *et al.* Electrical stimulation systems for cardiac tissue engineering. *Nat Protoc* **4**, 155-173, doi:10.1038/nprot.2008.183 (2009).
- 42 Maidhof, R. *et al.* Biomimetic perfusion and electrical stimulation applied in concert improved the assembly of engineered cardiac tissue. *Journal of tissue engineering and regenerative medicine* **6**, e12-23, doi:10.1002/term.525 (2012).
- 43 Dvir, T. *et al.* Nanowired three-dimensional cardiac patches. *Nature nanotechnology* **6**, 720-725, doi:10.1038/nnano.2011.160 (2011).
- 44 Shin, S. R. *et al.* Carbon-nanotube-embedded hydrogel sheets for engineering cardiac constructs and bioactuators. *ACS nano* **7**, 2369-2380, doi:10.1021/nn305559j (2013).
- 45 Tan, Y. *et al.* Silicon nanowire-induced maturation of cardiomyocytes derived from human induced pluripotent stem cells. *Nano letters* **15**, 2765-2772, doi:10.1021/nl502227a (2015).
- 46 Mathur, A. *et al.* Human iPSC-based Cardiac Microphysiological System For Drug Screening Applications. *Scientific reports* **5**, 8883, doi:10.1038/srep08883 (2015).
- 47 Mihic, A. *et al.* The effect of cyclic stretch on maturation and 3D tissue formation of human embryonic stem cell-derived cardiomyocytes. *Biomaterials* **35**, 2798-2808, doi:10.1016/j.biomaterials.2013.12.052 (2014).
- 48 Mannhardt, I. *et al.* Human Engineered Heart Tissue: Analysis of Contractile Force. *Stem cell reports* **7**, 29-42, doi:10.1016/j.stemcr.2016.04.011 (2016).
- 49 Richards, D. J. *et al.* Nanowires and Electrical Stimulation Synergistically Improve Functions of hiPSC Cardiac Spheroids. *Nano letters* **16**, 4670-4678, doi:10.1021/acs.nanolett.6b02093 (2016).
- 50 Thavandiran, N. *et al.* Design and formulation of functional pluripotent stem cell-derived cardiac microtissues. *Proceedings of the National Academy of Sciences of the United States of America* **110**, E4698-4707, doi:10.1073/pnas.1311120110 (2013).
- 51 Stevens, K. R. *et al.* Physiological function and transplantation of scaffold-free and vascularized human cardiac muscle tissue. *Proceedings of the National Academy of Sciences of the United States of America* **106**, 16568-16573, doi:10.1073/pnas.0908381106 (2009).
- 52 Ronaldson-Bouchard, K. *et al.* Advanced maturation of human cardiac tissue grown from pluripotent stem cells. *Nature* **556**, 239-243, doi:10.1038/s41586-018-0016-3 (2018).
- 53 Hussain, A., Collins, G., Yip, D. & Cho, C. H. Functional 3-D cardiac co-culture model using bioactive chitosan nanofiber scaffolds. *Biotechnology and bioengineering* **110**, 637-647, doi:10.1002/bit.24727 (2013).

- 54 Nichol, J. W., Engelmayr, G. C., Jr., Cheng, M. & Freed, L. E. Co-culture induces alignment in engineered cardiac constructs via MMP-2 expression. *Biochemical and biophysical research communications* **373**, 360-365, doi:10.1016/j.bbrc.2008.06.019 (2008).
- 55 Saini, H., Navaei, A., Van Putten, A. & Nikkhah, M. 3D cardiac microtissues encapsulated with the co-culture of cardiomyocytes and cardiac fibroblasts. *Advanced healthcare materials* **4**, 1961-1971, doi:10.1002/adhm.201500331 (2015).
- 56 Baker, L. A., Tiriach, H., Clevers, H. & Tuveson, D. A. Modeling pancreatic cancer with organoids. *Trends Cancer* **2**, 176-190, doi:10.1016/j.trecan.2016.03.004 (2016).
- 57 Clevers, H. Modeling Development and Disease with Organoids. *Cell* **165**, 1586-1597, doi:10.1016/j.cell.2016.05.082 (2016).
- 58 Lancaster, M. A. & Knoblich, J. A. Organogenesis in a dish: modeling development and disease using organoid technologies. *Science* **345**, 1247125, doi:10.1126/science.1247125 (2014).
- 59 McMurray, J. J. *et al.* Angiotensin-neprilysin inhibition versus enalapril in heart failure. *N Engl J Med* **371**, 993-1004, doi:10.1056/NEJMoa1409077 (2014).
- 60 Sacks, C. A., Jarcho, J. A. & Curfman, G. D. Paradigm shifts in heart-failure therapy--a timeline. *N Engl J Med* **371**, 989-991, doi:10.1056/NEJMp1410241 (2014).
- 61 Hay, M., Thomas, D. W., Craighead, J. L., Economides, C. & Rosenthal, J. Clinical development success rates for investigational drugs. *Nat Biotechnol* **32**, 40-51, doi:10.1038/nbt.2786 (2014).
- 62 Fine, B. & Vunjak-Novakovic, G. Shortcomings of Animal Models and the Rise of Engineered Human Cardiac Tissue. *Acs Biomater Sci Eng* **3**, 1884-1897, doi:10.1021/acsbiomaterials.6b00662 (2017).
- 63 Kaye, D. M. & Krum, H. Drug discovery for heart failure: a new era or the end of the pipeline? *Nat Rev Drug Discov* **6**, 127-139, doi:10.1038/nrd2219 (2007).
- 64 Klocke, R., Tian, W., Kuhlmann, M. T. & Nikol, S. Surgical animal models of heart failure related to coronary heart disease. *Cardiovascular research* **74**, 29-38, doi:10.1016/j.cardiores.2006.11.026 (2007).
- 65 Piacentino, V., 3rd *et al.* Cellular basis of abnormal calcium transients of failing human ventricular myocytes. *Circulation research* **92**, 651-658, doi:10.1161/01.RES.0000062469.83985.9B (2003).
- 66 Bers, D. M. Calcium fluxes involved in control of cardiac myocyte contraction. *Circulation research* **87**, 275-281 (2000).
- 67 Blinova, K. *et al.* Comprehensive Translational Assessment of Human-Induced Pluripotent Stem Cell Derived Cardiomyocytes for Evaluating Drug-Induced Arrhythmias. *Toxicological sciences : an official journal of the Society of Toxicology* **155**, 234-247, doi:10.1093/toxsci/kfw200 (2017).

- 68 Fermini, B. *et al.* A New Perspective in the Field of Cardiac Safety Testing through the Comprehensive In Vitro Proarrhythmia Assay Paradigm. *J. Biomol. Screen.* **21**, 1-11, doi:10.1177/1087057115594589 (2016).
- 69 Sager, P. T., Gintant, G., Turner, J. R., Pettit, S. & Stockbridge, N. Rechanneling the cardiac proarrhythmia safety paradigm: a meeting report from the Cardiac Safety Research Consortium. *Am Heart J* **167**, 292-300, doi:10.1016/j.ahj.2013.11.004 (2014).
- 70 ICH. (2005).
- 71 ICH. (2005).
- 72 Redfern, W. S. *et al.* Relationships between preclinical cardiac electrophysiology, clinical QT interval prolongation and torsade de pointes for a broad range of drugs: evidence for a provisional safety margin in drug development. *Cardiovascular research* **58**, 32-45 (2003).
- 73 Laverty, H. *et al.* How can we improve our understanding of cardiovascular safety liabilities to develop safer medicines? *Br J Pharmacol* **163**, 675-693, doi:10.1111/j.1476-5381.2011.01255.x (2011).
- 74 Paul, S. M. *et al.* How to improve R&D productivity: the pharmaceutical industry's grand challenge. *Nat Rev Drug Discov* **9**, 203-214, doi:10.1038/nrd3078 (2010).
- 75 Takahashi, K. *et al.* Induction of pluripotent stem cells from adult human fibroblasts by defined factors. *Cell* **131**, 861-872, doi:10.1016/j.cell.2007.11.019 (2007).
- 76 Yu, J. *et al.* Induced pluripotent stem cell lines derived from human somatic cells. *Science* **318**, 1917-1920, doi:10.1126/science.1151526 (2007).
- 77 Yoshida, Y. & Yamanaka, S. iPS cells: a source of cardiac regeneration. *Journal of molecular and cellular cardiology* **50**, 327-332, doi:10.1016/j.yjmcc.2010.10.026 (2011).
- 78 Spencer, C. I. *et al.* Calcium transients closely reflect prolonged action potentials in iPSC models of inherited cardiac arrhythmia. *Stem cell reports* **3**, 269-281, doi:10.1016/j.stemcr.2014.06.003 (2014).
- 79 Yokoo, N. *et al.* The effects of cardioactive drugs on cardiomyocytes derived from human induced pluripotent stem cells. *Biochemical and biophysical research communications* **387**, 482-488, doi:10.1016/j.bbrc.2009.07.052 (2009).
- 80 Tanaka, T. *et al.* In vitro pharmacologic testing using human induced pluripotent stem cell-derived cardiomyocytes. *Biochemical and biophysical research communications* **385**, 497-502, doi:10.1016/j.bbrc.2009.05.073 (2009).
- 81 Gibson, J. K., Yue, Y., Bronson, J., Palmer, C. & Numann, R. Human stem cell-derived cardiomyocytes detect drug-mediated changes in action potentials and ion currents. *J Pharmacol Toxicol Methods* **70**, 255-267, doi:10.1016/j.vascn.2014.09.005 (2014).

- 82 Ma, J. *et al.* High purity human-induced pluripotent stem cell-derived cardiomyocytes: electrophysiological properties of action potentials and ionic currents. *American journal of physiology. Heart and circulatory physiology* **301**, H2006-2017, doi:10.1152/ajpheart.00694.2011 (2011).
- 83 Maddah, M. *et al.* A Non-invasive Platform for Functional Characterization of Stem-Cell-Derived Cardiomyocytes with Applications in Cardiotoxicity Testing. *Stem cell reports*, doi:10.1016/j.stemcr.2015.02.007 (2015).
- 84 Kaneko, T. *et al.* On-chip in vitro cell-network pre-clinical cardiac toxicity using spatiotemporal human cardiomyocyte measurement on a chip. *Scientific reports* **4**, 4670, doi:10.1038/srep04670 (2014).
- 85 Hansen, A. *et al.* Development of a drug screening platform based on engineered heart tissue. *Circulation research* **107**, 35-44, doi:10.1161/CIRCRESAHA.109.211458 (2010).
- 86 Boudou, T. *et al.* A microfabricated platform to measure and manipulate the mechanics of engineered cardiac microtissues. *Tissue engineering. Part A* **18**, 910-919, doi:10.1089/ten.TEA.2011.0341 (2012).
- 87 Brandenburger, M. *et al.* Organotypic slice culture from human adult ventricular myocardium. *Cardiovascular research* **93**, 50-59, doi:10.1093/cvr/cvr259 (2012).
- 88 Sinha, G. The organoid architect. *Science* **357**, 746-749, doi:10.1126/science.357.6353.746 (2017).
- 89 Lancaster, M. A. *et al.* Cerebral organoids model human brain development and microcephaly. *Nature* **501**, 373-379, doi:10.1038/nature12517 (2013).
- 90 Dekkers, J. F. *et al.* A functional CFTR assay using primary cystic fibrosis intestinal organoids. *Nat Med* **19**, 939-945, doi:10.1038/nm.3201 (2013).
- 91 Schwank, G. *et al.* Functional repair of CFTR by CRISPR/Cas9 in intestinal stem cell organoids of cystic fibrosis patients. *Cell stem cell* **13**, 653-658, doi:10.1016/j.stem.2013.11.002 (2013).
- 92 Chakradhar, S. Put to the test: Organoid-based testing becomes a clinical tool. *Nat Med* **23**, 796-799, doi:10.1038/nm0717-796 (2017).
- 93 Triedman, J. K. & Newburger, J. W. Trends in Congenital Heart Disease: The Next Decade. *Circulation* **133**, 2716-2733, doi:10.1161/CIRCULATIONAHA.116.023544 (2016).
- 94 Benjamin, E. J. *et al.* Heart Disease and Stroke Statistics-2017 Update: A Report From the American Heart Association. *Circulation* **135**, e146-e603, doi:10.1161/CIR.0000000000000485 (2017).
- 95 Chanana, A. M., Rhee, J. W. & Wu, J. C. Human-induced pluripotent stem cell approaches to model inborn and acquired metabolic heart diseases. *Curr Opin Cardiol* **31**, 266-274, doi:10.1097/HCO.0000000000000277 (2016).
- 96 Liang, P. *et al.* Drug screening using a library of human induced pluripotent stem cell-derived cardiomyocytes reveals disease-specific patterns of cardiotoxicity. *Circulation* **127**, 1677-1691, doi:10.1161/CIRCULATIONAHA.113.001883 (2013).



- 97 Lodola, F. *et al.* Adeno-associated virus-mediated CASQ2 delivery rescues phenotypic alterations in a patient-specific model of recessive catecholaminergic polymorphic ventricular tachycardia. *Cell Death Dis* **7**, e2393, doi:10.1038/cddis.2016.304 (2016).
- 98 Ma, D. *et al.* Generation of patient-specific induced pluripotent stem cell-derived cardiomyocytes as a cellular model of arrhythmogenic right ventricular cardiomyopathy. *European heart journal* **34**, 1122-1133, doi:10.1093/eurheartj/ehs226 (2013).
- 99 Matsa, E. *et al.* Transcriptome Profiling of Patient-Specific Human iPSC-Cardiomyocytes Predicts Individual Drug Safety and Efficacy Responses In Vitro. *Cell stem cell* **19**, 311-325, doi:10.1016/j.stem.2016.07.006 (2016).
- 100 Oh, Y., Wei, H., Ma, D., Sun, X. & Liew, R. Clinical applications of patient-specific induced pluripotent stem cells in cardiovascular medicine. *Heart* **98**, 443-449, doi:10.1136/heartjnl-2011-301317 (2012).
- 101 Sun, N. *et al.* Patient-specific induced pluripotent stem cells as a model for familial dilated cardiomyopathy. *Science translational medicine* **4**, 130ra147, doi:10.1126/scitranslmed.3003552 (2012).
- 102 Wang, G. *et al.* Modeling the mitochondrial cardiomyopathy of Barth syndrome with induced pluripotent stem cell and heart-on-chip technologies. *Nat Med* **20**, 616-623, doi:10.1038/nm.3545 (2014).
- 103 Segers, V. F. & Lee, R. T. Stem-cell therapy for cardiac disease. *Nature* **451**, 937-942, doi:10.1038/nature06800 (2008).
- 104 Oh, S. I. *et al.* Technological progress in generation of induced pluripotent stem cells for clinical applications. *ScientificWorldJournal* **2012**, 417809, doi:10.1100/2012/417809 (2012).
- 105 Hodgson, D. M. *et al.* Stable benefit of embryonic stem cell therapy in myocardial infarction. *American journal of physiology. Heart and circulatory physiology* **287**, H471-479, doi:10.1152/ajpheart.01247.2003 (2004).
- 106 Min, J. Y. *et al.* Transplantation of embryonic stem cells improves cardiac function in postinfarcted rats. *J Appl Physiol (1985)* **92**, 288-296 (2002).
- 107 Min, J. Y. *et al.* Long-term improvement of cardiac function in rats after infarction by transplantation of embryonic stem cells. *J Thorac Cardiovasc Surg* **125**, 361-369, doi:10.1067/mtc.2003.101 (2003).
- 108 Singla, D. K. *et al.* Transplantation of embryonic stem cells into the infarcted mouse heart: formation of multiple cell types. *Journal of molecular and cellular cardiology* **40**, 195-200, doi:10.1016/j.yjmcc.2005.09.001 (2006).
- 109 Nussbaum, J. *et al.* Transplantation of undifferentiated murine embryonic stem cells in the heart: teratoma formation and immune response. *FASEB journal : official publication of the Federation of American Societies for Experimental Biology* **21**, 1345-1357, doi:10.1096/fj.06-6769com (2007).

- 110 Swijnenburg, R. J. *et al.* Embryonic stem cell immunogenicity increases upon differentiation after transplantation into ischemic myocardium. *Circulation* **112**, 1166-172, doi:10.1161/CIRCULATIONAHA.104.525824 (2005).
- 111 Caspi, O. *et al.* Transplantation of human embryonic stem cell-derived cardiomyocytes improves myocardial performance in infarcted rat hearts. *Journal of the American College of Cardiology* **50**, 1884-1893, doi:10.1016/j.jacc.2007.07.054 (2007).
- 112 Bearzi, C. *et al.* Human cardiac stem cells. *Proceedings of the National Academy of Sciences of the United States of America* **104**, 14068-14073, doi:10.1073/pnas.0706760104 (2007).
- 113 Menard, C. *et al.* Transplantation of cardiac-committed mouse embryonic stem cells to infarcted sheep myocardium: a preclinical study. *Lancet* **366**, 1005-1012, doi:10.1016/S0140-6736(05)67380-1 (2005).
- 114 Lee, S. T. *et al.* Intramyocardial injection of autologous cardiospheres or cardiosphere-derived cells preserves function and minimizes adverse ventricular remodeling in pigs with heart failure post-myocardial infarction. *Journal of the American College of Cardiology* **57**, 455-465, doi:10.1016/j.jacc.2010.07.049 (2011).
- 115 Behfar, A., Crespo-Diaz, R., Terzic, A. & Gersh, B. J. Cell therapy for cardiac repair-lessons from clinical trials. *Nat Rev Cardiol* **11**, 232-246, doi:10.1038/nrcardio.2014.9 (2014).
- 116 Bartunek, J. *et al.* Cardiopoietic stem cell therapy in heart failure: the C-CURE (Cardiopoietic stem Cell therapy in heart failURE) multicenter randomized trial with lineage-specified biologics. *Journal of the American College of Cardiology* **61**, 2329-2338, doi:10.1016/j.jacc.2013.02.071 (2013).
- 117 Kehat, I. *et al.* Electromechanical integration of cardiomyocytes derived from human embryonic stem cells. *Nat Biotechnol* **22**, 1282-1289, doi:10.1038/nbt1014 (2004).
- 118 Xue, T. *et al.* Functional integration of electrically active cardiac derivatives from genetically engineered human embryonic stem cells with quiescent recipient ventricular cardiomyocytes: insights into the development of cell-based pacemakers. *Circulation* **111**, 11-20, doi:10.1161/01.CIR.0000151313.18547.A2 (2005).
- 119 Laflamme, M. A. *et al.* Formation of human myocardium in the rat heart from human embryonic stem cells. *The American journal of pathology* **167**, 663-671, doi:10.1016/S0002-9440(10)62041-X (2005).
- 120 Chong, J. J. *et al.* Human embryonic-stem-cell-derived cardiomyocytes regenerate non-human primate hearts. *Nature* **510**, 273-277, doi:10.1038/nature13233 (2014).

- 121 Anderson, M. E., Goldhaber, J., Houser, S. R., Puceat, M. & Sussman, M. A. Embryonic stem cell-derived cardiac myocytes are not ready for human trials. *Circulation research* **115**, 335-338, doi:10.1161/CIRCRESAHA.114.304616 (2014).
- 122 Winter, E. M. *et al.* A new direction for cardiac regeneration therapy: application of synergistically acting epicardium-derived cells and cardiomyocyte progenitor cells. *Circulation. Heart failure* **2**, 643-653, doi:10.1161/CIRCHEARTFAILURE.108.843722 (2009).
- 123 Williams, A. R. *et al.* Enhanced effect of combining human cardiac stem cells and bone marrow mesenchymal stem cells to reduce infarct size and to restore cardiac function after myocardial infarction. *Circulation* **127**, 213-223, doi:10.1161/CIRCULATIONAHA.112.131110 (2013).
- 124 Lee, W. Y. *et al.* Vascularization and restoration of heart function in rat myocardial infarction using transplantation of human cbMSC/HUVEC core-shell bodies. *Biomaterials* **33**, 2127-2136, doi:10.1016/j.biomaterials.2011.11.059 (2012).
- 125 Kim, J. H. *et al.* Therapeutic angiogenesis of three-dimensionally cultured adipose-derived stem cells in rat infarcted hearts. *Cytotherapy* **15**, 542-556, doi:10.1016/j.jcyt.2012.11.016 (2013).
- 126 Quijada, P. *et al.* Cardiac Stem Cell Hybrids Enhance Myocardial Repair. *Circulation research* **117**, 695-706, doi:10.1161/CIRCRESAHA.115.306838 (2015).
- 127 Lee, M. & Wu, B. M. Recent advances in 3D printing of tissue engineering scaffolds. *Methods in molecular biology* **868**, 257-267, doi:10.1007/978-1-61779-764-4\_15 (2012).
- 128 Mandrycky, C., Wang, Z., Kim, K. & Kim, D. H. 3D bioprinting for engineering complex tissues. *Biotechnol Adv*, doi:10.1016/j.biotechadv.2015.12.011 (2015).
- 129 Mironov, V., Kasyanov, V. & Markwald, R. R. Organ printing: from bioprinter to organ biofabrication line. *Curr Opin Biotechnol* **22**, 667-673, doi:10.1016/j.copbio.2011.02.006 (2011).
- 130 Murphy, S. V. & Atala, A. 3D bioprinting of tissues and organs. *Nat Biotechnol* **32**, 773-785, doi:10.1038/nbt.2958 (2014).
- 131 Yeong, W. Y., Chua, C. K., Leong, K. F. & Chandrasekaran, M. Rapid prototyping in tissue engineering: challenges and potential. *Trends Biotechnol* **22**, 643-652, doi:10.1016/j.tibtech.2004.10.004 (2004).
- 132 Visconti, R. P. *et al.* Towards organ printing: engineering an intra-organ branched vascular tree. *Expert Opin Biol Ther* **10**, 409-420, doi:10.1517/14712590903563352 (2010).
- 133 Fedorovich, N. E., Alblas, J., Hennink, W. E., Oner, F. C. & Dhert, W. J. Organ printing: the future of bone regeneration? *Trends Biotechnol* **29**, 601-606, doi:10.1016/j.tibtech.2011.07.001 (2011).

- 134 Kim, S. S. *et al.* Survival and function of hepatocytes on a novel three-dimensional synthetic biodegradable polymer scaffold with an intrinsic network of channels. *Ann Surg* **228**, 8-13 (1998).
- 135 Norotte, C., Marga, F. S., Niklason, L. E. & Forgacs, G. Scaffold-free vascular tissue engineering using bioprinting. *Biomaterials* **30**, 5910-5917, doi:10.1016/j.biomaterials.2009.06.034 (2009).
- 136 Gao, G. & Cui, X. Three-dimensional bioprinting in tissue engineering and regenerative medicine. *Biotechnology letters*, doi:10.1007/s10529-015-1975-1 (2015).
- 137 Chang, R., Emami, K., Wu, H. & Sun, W. Biofabrication of a three-dimensional liver micro-organ as an in vitro drug metabolism model. *Biofabrication* **2**, 045004, doi:10.1088/1758-5082/2/4/045004 (2010).
- 138 Marga, F. *et al.* Toward engineering functional organ modules by additive manufacturing. *Biofabrication* **4**, 022001, doi:10.1088/1758-5082/4/2/022001 (2012).
- 139 Xu, T. *et al.* Hybrid printing of mechanically and biologically improved constructs for cartilage tissue engineering applications. *Biofabrication* **5**, 015001, doi:10.1088/1758-5082/5/1/015001 (2013).
- 140 Ebrahimkhani, M. R., Young, C. L., Lauffenburger, D. A., Griffith, L. G. & Borenstein, J. T. Approaches to in vitro tissue regeneration with application for human disease modeling and drug development. *Drug Discov Today* **19**, 754-762, doi:10.1016/j.drudis.2014.04.017 (2014).
- 141 Griffith, L. G. & Swartz, M. A. Capturing complex 3D tissue physiology in vitro. *Nat Rev Mol Cell Biol* **7**, 211-224, doi:10.1038/nrm1858 (2006).
- 142 Khetani, S. R. & Bhatia, S. N. Engineering tissues for in vitro applications. *Curr Opin Biotechnol* **17**, 524-531, doi:10.1016/j.copbio.2006.08.009 (2006).
- 143 Raimondi, M. T. Engineered tissue as a model to study cell and tissue function from a biophysical perspective. *Curr Drug Discov Technol* **3**, 245-268 (2006).
- 144 Porteus, M. Translating the lessons from gene therapy to the development of regenerative medicine. *Molecular therapy : the journal of the American Society of Gene Therapy* **19**, 439-441, doi:10.1038/mt.2011.14 (2011).
- 145 Bernstein, B. E., Meissner, A. & Lander, E. S. The mammalian epigenome. *Cell* **128**, 669-681, doi:10.1016/j.cell.2007.01.033 (2007).
- 146 Goldberg, A. D., Allis, C. D. & Bernstein, E. Epigenetics: a landscape takes shape. *Cell* **128**, 635-638, doi:10.1016/j.cell.2007.02.006 (2007).
- 147 Marga, F., Neagu, A., Kosztin, I. & Forgacs, G. Developmental biology and tissue engineering. *Birth Defects Res C Embryo Today* **81**, 320-328, doi:10.1002/bdrc.20109 (2007).
- 148 Lin, H. R. & Yeh, Y. J. Porous alginate/hydroxyapatite composite scaffolds for bone tissue engineering: preparation, characterization, and in vitro studies. *J Biomed Mater Res B Appl Biomater* **71**, 52-65, doi:10.1002/jbm.b.30065 (2004).

- 149 Nakamura, M., Iwanaga, S., Henmi, C., Arai, K. & Nishiyama, Y. Biomatrices and biomaterials for future developments of bioprinting and biofabrication. *Biofabrication* **2**, 014110, doi:10.1088/1758-5082/2/1/014110 (2010).
- 150 Rowley, J. A., Madlambayan, G. & Mooney, D. J. Alginate hydrogels as synthetic extracellular matrix materials. *Biomaterials* **20**, 45-53 (1999).
- 151 Yao, R., Zhang, R., Luan, J. & Lin, F. Alginate and alginate/gelatin microspheres for human adipose-derived stem cell encapsulation and differentiation. *Biofabrication* **4**, 025007, doi:10.1088/1758-5082/4/2/025007 (2012).
- 152 Xu, C., Chai, W., Huang, Y. & Markwald, R. R. Scaffold-free inkjet printing of three-dimensional zigzag cellular tubes. *Biotechnology and bioengineering* **109**, 3152-3160, doi:10.1002/bit.24591 (2012).
- 153 Billiet, T., Vandenhaute, M., Schelfhout, J., Van Vlierberghe, S. & Dubruel, P. A review of trends and limitations in hydrogel-rapid prototyping for tissue engineering. *Biomaterials* **33**, 6020-6041, doi:10.1016/j.biomaterials.2012.04.050 (2012).
- 154 Lewis, K. J. & Anseth, K. S. Hydrogel scaffolds to study cell biology in four dimensions. *MRS Bull* **38**, 260-268, doi:10.1557/mrs.2013.54 (2013).
- 155 Badylak, S. F. The extracellular matrix as a scaffold for tissue reconstruction. *Semin. Cell Dev. Biol.* **13**, 377-383 (2002).
- 156 Kim, B. S. & Mooney, D. J. Development of biocompatible synthetic extracellular matrices for tissue engineering. *Trends Biotechnol* **16**, 224-230 (1998).
- 157 Orive, G., Carcaboso, A. M., Hernandez, R. M., Gascon, A. R. & Pedraz, J. L. Biocompatibility evaluation of different alginates and alginate-based microcapsules. *Biomacromolecules* **6**, 927-931, doi:10.1021/bm049380x (2005).
- 158 Bouhadir, K. H. *et al.* Degradation of partially oxidized alginate and its potential application for tissue engineering. *Biotechnol Prog* **17**, 945-950, doi:10.1021/bp010070p (2001).
- 159 Lee, K. Y. & Mooney, D. J. Alginate: properties and biomedical applications. *Prog Polym Sci* **37**, 106-126, doi:10.1016/j.progpolymsci.2011.06.003 (2012).
- 160 Wang, L., Shansky, J., Borselli, C., Mooney, D. & Vandenburgh, H. Design and fabrication of a biodegradable, covalently crosslinked shape-memory alginate scaffold for cell and growth factor delivery. *Tissue engineering. Part A* **18**, 2000-2007, doi:10.1089/ten.TEA.2011.0663 (2012).
- 161 Gimble, J. M., Katz, A. J. & Bunnell, B. A. Adipose-derived stem cells for regenerative medicine. *Circulation research* **100**, 1249-1260, doi:10.1161/01.RES.0000265074.83288.09 (2007).
- 162 Alsberg, E., Anderson, K. W., Albeiruti, A., Rowley, J. A. & Mooney, D. J. Engineering growing tissues. *Proceedings of the National Academy of Sciences of the United States of America* **99**, 12025-12030, doi:10.1073/pnas.192291499 (2002).

- 163 Boontheekul, T., Kong, H. J. & Mooney, D. J. Controlling alginate gel degradation utilizing partial oxidation and bimodal molecular weight distribution. *Biomaterials* **26**, 2455-2465, doi:10.1016/j.biomaterials.2004.06.044 (2005).
- 164 Malda, J. *et al.* 25th anniversary article: Engineering hydrogels for biofabrication. *Adv Mater* **25**, 5011-5028, doi:10.1002/adma.201302042 (2013).
- 165 Derby, B. Printing and prototyping of tissues and scaffolds. *Science* **338**, 921-926, doi:10.1126/science.1226340 (2012).
- 166 Ferris, C. J., Gilmore, K. G., Wallace, G. G. & In het Panhuis, M. Biofabrication: an overview of the approaches used for printing of living cells. *Appl Microbiol Biotechnol* **97**, 4243-4258, doi:10.1007/s00253-013-4853-6 (2013).
- 167 Blaeser, A. *et al.* Biofabrication under fluorocarbon: a novel freeform fabrication technique to generate high aspect ratio tissue-engineered constructs. *Biores Open Access* **2**, 374-384, doi:10.1089/biores.2013.0031 (2013).
- 168 Gaetani, R. *et al.* Cardiac tissue engineering using tissue printing technology and human cardiac progenitor cells. *Biomaterials* **33**, 1782-1790, doi:10.1016/j.biomaterials.2011.11.003 (2012).
- 169 Guillotin, B. *et al.* Laser assisted bioprinting of engineered tissue with high cell density and microscale organization. *Biomaterials* **31**, 7250-7256, doi:10.1016/j.biomaterials.2010.05.055 (2010).
- 170 Murphy, S. V., Skardal, A. & Atala, A. Evaluation of hydrogels for bio-printing applications. *Journal of biomedical materials research. Part A* **101**, 272-284, doi:10.1002/jbm.a.34326 (2013).
- 171 Lin, H. *et al.* Application of visible light-based projection stereolithography for live cell-scaffold fabrication with designed architecture. *Biomaterials* **34**, 331-339, doi:10.1016/j.biomaterials.2012.09.048 (2013).
- 172 Schuurman, W. *et al.* Gelatin-methacrylamide hydrogels as potential biomaterials for fabrication of tissue-engineered cartilage constructs. *Macromol Biosci* **13**, 551-561, doi:10.1002/mabi.201200471 (2013).
- 173 Fedorovich, N. E., De Wijn, J. R., Verbout, A. J., Alblas, J. & Dhert, W. J. Three-dimensional fiber deposition of cell-laden, viable, patterned constructs for bone tissue printing. *Tissue engineering. Part A* **14**, 127-133, doi:10.1089/ten.a.2007.0158 (2008).
- 174 Fedorovich, N. E. *et al.* Biofabrication of osteochondral tissue equivalents by printing topologically defined, cell-laden hydrogel scaffolds. *Tissue engineering. Part C, Methods* **18**, 33-44, doi:10.1089/ten.TEC.2011.0060 (2012).
- 175 Tirella, A., Orsini, A., Vozzi, G. & Ahluwalia, A. A phase diagram for microfabrication of geometrically controlled hydrogel scaffolds. *Biofabrication* **1**, 045002, doi:10.1088/1758-5082/1/4/045002 (2009).
- 176 Bryant, S. J. & Anseth, K. S. Hydrogel properties influence ECM production by chondrocytes photoencapsulated in poly(ethylene glycol) hydrogels. *J Biomed Mater Res* **59**, 63-72 (2002).

- 177 Nicodemus, G. D. & Bryant, S. J. Cell encapsulation in biodegradable hydrogels for tissue engineering applications. *Tissue engineering. Part B, Reviews* **14**, 149-165, doi:10.1089/ten.teb.2007.0332 (2008).
- 178 Kong, H. J., Kaigler, D., Kim, K. & Mooney, D. J. Controlling rigidity and degradation of alginate hydrogels via molecular weight distribution. *Biomacromolecules* **5**, 1720-1727, doi:10.1021/bm049879r (2004).
- 179 Kang, K. H., Hockaday, L. A. & Butcher, J. T. Quantitative optimization of solid freeform deposition of aqueous hydrogels. *Biofabrication* **5**, 035001, doi:10.1088/1758-5082/5/3/035001 (2013).
- 180 Tholpady, S. S. *et al.* The cellular plasticity of human adipocytes. *Ann Plast Surg* **54**, 651-656 (2005).
- 181 Spiegelman, B. M. & Ginty, C. A. Fibronectin modulation of cell shape and lipogenic gene expression in 3T3-adipocytes. *Cell* **35**, 657-666 (1983).
- 182 McBeath, R., Pirone, D. M., Nelson, C. M., Bhadriraju, K. & Chen, C. S. Cell shape, cytoskeletal tension, and RhoA regulate stem cell lineage commitment. *Dev Cell* **6**, 483-495 (2004).
- 183 Ruoslahti, E. RGD and other recognition sequences for integrins. *Annu Rev Cell Dev Biol* **12**, 697-715, doi:10.1146/annurev.cellbio.12.1.697 (1996).
- 184 D'Souza, S. E., Ginsberg, M. H. & Plow, E. F. Arginyl-glycyl-aspartic acid (RGD): a cell adhesion motif. *Trends Biochem. Sci.* **16**, 246-250 (1991).
- 185 Pfaff, M. *et al.* Selective recognition of cyclic RGD peptides of NMR defined conformation by alpha IIb beta 3, alpha V beta 3, and alpha 5 beta 1 integrins. *The Journal of biological chemistry* **269**, 20233-20238 (1994).
- 186 Zuk, P. A. *et al.* Human adipose tissue is a source of multipotent stem cells. *Mol Biol Cell* **13**, 4279-4295, doi:10.1091/mbc.E02-02-0105 (2002).
- 187 Zuk, P. A. *et al.* Multilineage cells from human adipose tissue: implications for cell-based therapies. *Tissue Eng* **7**, 211-228, doi:10.1089/107632701300062859 (2001).
- 188 Zhu, Y. *et al.* Adipose-derived stem cell: a better stem cell than BMSC. *Cell biochemistry and function* **26**, 664-675, doi:10.1002/cbf.1488 (2008).
- 189 Matsuoka, F. *et al.* Morphology-based prediction of osteogenic differentiation potential of human mesenchymal stem cells. *PloS one* **8**, e55082, doi:10.1371/journal.pone.0055082 (2013).
- 190 Hauselmann, H. J. *et al.* Phenotypic stability of bovine articular chondrocytes after long-term culture in alginate beads. *J Cell Sci* **107 ( Pt 1)**, 17-27 (1994).
- 191 Stains, J. P. & Civitelli, R. Cell-cell interactions in regulating osteogenesis and osteoblast function. *Birth Defects Res C Embryo Today* **75**, 72-80, doi:10.1002/bdrc.20034 (2005).
- 192 Benton, J. A., Fairbanks, B. D. & Anseth, K. S. Characterization of valvular interstitial cell function in three dimensional matrix metalloproteinase

- degradable PEG hydrogels. *Biomaterials* **30**, 6593-6603, doi:10.1016/j.biomaterials.2009.08.031 (2009).
- 193 Yellowley, C. E., Hancox, J. C. & Donahue, H. J. Effects of cell swelling on intracellular calcium and membrane currents in bovine articular chondrocytes. *Journal of cellular biochemistry* **86**, 290-301, doi:10.1002/jcb.10217 (2002).
- 194 Pataky, K. *et al.* Microdrop printing of hydrogel bioinks into 3D tissue-like geometries. *Adv Mater* **24**, 391-396, doi:10.1002/adma.201102800 (2012).
- 195 Hollister, S. J. Porous scaffold design for tissue engineering. *Nat Mater* **4**, 518-524, doi:10.1038/nmat1421 (2005).
- 196 Langer, R. & Vacanti, J. P. Tissue engineering. *Science* **260**, 920-926 (1993).
- 197 Mironov, V. *et al.* Organ printing: tissue spheroids as building blocks. *Biomaterials* **30**, 2164-2174, doi:10.1016/j.biomaterials.2008.12.084 (2009).
- 198 Tan, Y. *et al.* Cell number per spheroid and electrical conductivity of nanowires influence the function of silicon nanowired human cardiac spheroids. *Acta Biomater* **51**, 495-504, doi:10.1016/j.actbio.2017.01.029 (2017).
- 199 Schmidt, V., Wittemann, J. V., Senz, S. & Gosele, U. Silicon Nanowires: A Review on Aspects of their Growth and their Electrical Properties. *Adv Mater* **21**, 2681-2702 (2009).
- 200 Tian, B. & Lieber, C. M. Synthetic nanoelectronic probes for biological cells and tissues. *Annual review of analytical chemistry* **6**, 31-51, doi:10.1146/annurev-anchem-062012-092623 (2013).
- 201 Zheng, G. F., Lu, W., Jin, S. & Lieber, C. M. Synthesis and fabrication of high performance n-type silicon nanowire transistors. *Adv Mater* **16**, 1890-1893 (2004).
- 202 Mazzoleni, A. P., Siskin, B. F. & Kahler, R. L. Conductivity values of tissue culture medium from 20 degrees C to 40 degrees C. *Bioelectromagnetics* **7**, 95-99 (1986).
- 203 Garipcan, B. *et al.* In Vitro Biocompatibility of n-Type and Undoped Silicon Nanowires. *Adv. Eng. Mater.* **13**, B3-B9 (2009).
- 204 Zimmerman, J. F. *et al.* Cellular uptake and dynamics of unlabeled freestanding silicon nanowires. *Sci Adv* **2**, e1601039, doi:10.1126/sciadv.1601039 (2016).
- 205 Jiang, K. *et al.* Medicinal surface modification of silicon nanowires: impact on calcification and stromal cell proliferation. *ACS applied materials & interfaces* **1**, 266-269, doi:10.1021/am800219r (2009).
- 206 Nagesha, D. K., Whitehead, M. A. & Coffer, J. L. Biorelevant Calcification and Non-Cytotoxic Behavior in Silicon Nanowires. *Adv Mater* **17**, 921-924 (2005).
- 207 Anderson, S. H. C., Elliott, H., Wallis, D. J., Canham, L. T. & Powell, J. J. Dissolution of different forms of partially porous silicon wafers under simulated physiological conditions. *phys. stat. sol (a)* **197**, 331-335 (2003).
- 208 Zhou, W. *et al.* Long term stability of nanowire nanoelectronics in physiological environments. *Nano letters* **14**, 1614-1619, doi:10.1021/nl500070h (2014).



- 209 Tolli, M. A. *et al.* In vivo biocompatibility of porous silicon biomaterials for drug delivery to the heart. *Biomaterials* **35**, 8394-8405, doi:10.1016/j.biomaterials.2014.05.078 (2014).
- 210 Inoue, N. *et al.* Rapid electrical stimulation of contraction modulates gap junction protein in neonatal rat cultured cardiomyocytes: involvement of mitogen-activated protein kinases and effects of angiotensin II-receptor antagonist. *Journal of the American College of Cardiology* **44**, 914-922, doi:10.1016/j.jacc.2004.05.054 (2004).
- 211 Au, H. T., Cheng, I., Chowdhury, M. F. & Radisic, M. Interactive effects of surface topography and pulsatile electrical field stimulation on orientation and elongation of fibroblasts and cardiomyocytes. *Biomaterials* **28**, 4277-4293, doi:10.1016/j.biomaterials.2007.06.001 (2007).
- 212 Kato, S., Ivester, C. T., Cooper, G. t., Zile, M. R. & McDermott, P. J. Growth effects of electrically stimulated contraction on adult feline cardiocytes in primary culture. *Am J Physiol* **268**, H2495-2504 (1995).
- 213 Palatinus, J. A., Rhett, J. M. & Gourdie, R. G. The connexin43 carboxyl terminus and cardiac gap junction organization. *Biochimica et biophysica acta* **1818**, 1831-1843, doi:10.1016/j.bbamem.2011.08.006 (2012).
- 214 Vreeker, A. *et al.* Assembly of the cardiac intercalated disk during pre- and postnatal development of the human heart. *PloS one* **9**, e94722, doi:10.1371/journal.pone.0094722 (2014).
- 215 Giepmans, B. N. Gap junctions and connexin-interacting proteins. *Cardiovascular research* **62**, 233-245, doi:10.1016/j.cardiores.2003.12.009 (2004).
- 216 Shaw, R. M. *et al.* Microtubule plus-end-tracking proteins target gap junctions directly from the cell interior to adherens junctions. *Cell* **128**, 547-560, doi:10.1016/j.cell.2006.12.037 (2007).
- 217 Miyata, S., Minobe, W., Bristow, M. R. & Leinwand, L. A. Myosin heavy chain isoform expression in the failing and nonfailing human heart. *Circulation research* **86**, 386-390 (2000).
- 218 Krenz, M. & Robbins, J. Impact of beta-myosin heavy chain expression on cardiac function during stress. *Journal of the American College of Cardiology* **44**, 2390-2397, doi:10.1016/j.jacc.2004.09.044 (2004).
- 219 Lompre, A. M., Nadal-Ginard, B. & Mahdavi, V. Expression of the cardiac ventricular alpha- and beta-myosin heavy chain genes is developmentally and hormonally regulated. *The Journal of biological chemistry* **259**, 6437-6446 (1984).
- 220 Pope, B., Hoh, J. F. & Weeds, A. The ATPase activities of rat cardiac myosin isoenzymes. *FEBS letters* **118**, 205-208 (1980).
- 221 Bedada, F. B. *et al.* Acquisition of a quantitative, stoichiometrically conserved ratiometric marker of maturation status in stem cell-derived cardiac myocytes. *Stem cell reports* **3**, 594-605, doi:10.1016/j.stemcr.2014.07.012 (2014).

- 222 Schwan, J. & Campbell, S. G. Prospects for In Vitro Myofilament Maturation in Stem Cell-Derived Cardiac Myocytes. *Biomark Insights* **10**, 91-103, doi:10.4137/BMI.S23912 (2015).
- 223 Kim, C. *et al.* Non-cardiomyocytes influence the electrophysiological maturation of human embryonic stem cell-derived cardiomyocytes during differentiation. *Stem cells and development* **19**, 783-795, doi:10.1089/scd.2009.0349 (2010).
- 224 Sizarov, A. *et al.* Molecular analysis of patterning of conduction tissues in the developing human heart. *Circ Arrhythm Electrophysiol* **4**, 532-542, doi:10.1161/CIRCEP.111.963421 (2011).
- 225 Bett, G. C. *et al.* Electronic "expression" of the inward rectifier in cardiocytes derived from human-induced pluripotent stem cells. *Heart rhythm : the official journal of the Heart Rhythm Society* **10**, 1903-1910, doi:10.1016/j.hrthm.2013.09.061 (2013).
- 226 Menasche, P. Stem cell therapy for heart failure: are arrhythmias a real safety concern? *Circulation* **119**, 2735-2740, doi:10.1161/CIRCULATIONAHA.108.812693 (2009).
- 227 Silvestre, J. & Menasche, P. The evolution of stem cell theory for heart failure. *EBioMedicine* (2015 ).
- 228 Quijada, P. & Sussman, M. A. Making it stick: chasing the optimal stem cells for cardiac regeneration. *Expert Rev Cardiovasc Ther* **12**, 1275-1288, doi:10.1586/14779072.2014.972941 (2014).
- 229 Lee, W. Y. *et al.* Enhancement of cell retention and functional benefits in myocardial infarction using human amniotic-fluid stem-cell bodies enriched with endogenous ECM. *Biomaterials* **32**, 5558-5567, doi:10.1016/j.biomaterials.2011.04.031 (2011).
- 230 Moon, S. H. *et al.* The use of aggregates of purified cardiomyocytes derived from human ESCs for functional engraftment after myocardial infarction. *Biomaterials* **34**, 4013-4026, doi:10.1016/j.biomaterials.2013.02.022 (2013).
- 231 Fernandes, S. *et al.* Comparison of Human Embryonic Stem Cell-Derived Cardiomyocytes, Cardiovascular Progenitors, and Bone Marrow Mononuclear Cells for Cardiac Repair. *Stem cell reports* **5**, 753-762, doi:10.1016/j.stemcr.2015.09.011 (2015).
- 232 Wu, Y. *et al.* Controlled Growth and Structures of Molecular-Scale Silicon Nanowires. *Nano Lett.* **4**, 433-436, doi:10.1021/nl035162i (2004).
- 233 Takebe, T. *et al.* Vascularized and functional human liver from an iPSC-derived organ bud transplant. *Nature* **499**, 481-484, doi:10.1038/nature12271 (2013).
- 234 Takasato, M. *et al.* Kidney organoids from human iPS cells contain multiple lineages and model human nephrogenesis. *Nature* **526**, 564-568, doi:10.1038/nature15695 (2015).

- 235 Dye, B. R. *et al.* A bioengineered niche promotes in vivo engraftment and maturation of pluripotent stem cell derived human lung organoids. *eLife* **5**, doi:10.7554/eLife.19732 (2016).
- 236 Shkumatov, A., Baek, K. & Kong, H. Matrix rigidity-modulated cardiovascular organoid formation from embryoid bodies. *PloS one* **9**, e94764, doi:10.1371/journal.pone.0094764 (2014).
- 237 Takebe, T. *et al.* Vascularized and Complex Organ Buds from Diverse Tissues via Mesenchymal Cell-Driven Condensation. *Cell stem cell* **16**, 556-565, doi:10.1016/j.stem.2015.03.004 (2015).
- 238 Gunter, J. *et al.* Microtissues in Cardiovascular Medicine: Regenerative Potential Based on a 3D Microenvironment. *Stem Cells Int* **2016**, 9098523, doi:10.1155/2016/9098523 (2016).
- 239 Matsa, E., Ahrens, J. H. & Wu, J. C. Human Induced Pluripotent Stem Cells as a Platform for Personalized and Precision Cardiovascular Medicine. *Physiol. Rev.* **96**, 1093-1126, doi:10.1152/physrev.00036.2015 (2016).
- 240 Matsa, E. *et al.* Transcriptome Profiling of Patient-Specific Human iPSC-Cardiomyocytes Predicts Individual Drug Safety and Efficacy Responses In Vitro. *Cell stem cell*, doi:10.1016/j.stem.2016.07.006 (2016).
- 241 Ogle, B. M. *et al.* Distilling complexity to advance cardiac tissue engineering. *Science translational medicine* **8**, 342ps313, doi:10.1126/scitranslmed.aad2304 (2016).
- 242 Ribas, J. *et al.* Cardiovascular Organ-on-a-Chip Platform for Drug Discovery and Development. *Applied In Vitro Toxicology* **2**, 82-96, doi:10.1089/aivt.2016.0002 (2016).
- 243 Tiburcy, M. *et al.* Defined Engineered Human Myocardium with Advanced Maturation for Applications in Heart Failure Modelling and Repair. *Circulation*, doi:10.1161/CIRCULATIONAHA.116.024145 (2017).
- 244 Kelm, J. M. *et al.* Tissue-transplant fusion and vascularization of myocardial microtissues and macro tissues implanted into chicken embryos and rats. *Tissue Eng* **12**, 2541-2553, doi:10.1089/ten.2006.12.2541 (2006).
- 245 BurrIDGE, P. W. *et al.* Multi-cellular interactions sustain long-term contractility of human pluripotent stem cell-derived cardiomyocytes. *American journal of translational research* **6**, 724-735 (2014).
- 246 Kaneko, T., Nomura, F. & Yasuda, K. On-chip constructive cell-network study (I): contribution of cardiac fibroblasts to cardiomyocyte beating synchronization and community effect. *J Nanobiotechnology* **9**, 21, doi:10.1186/1477-3155-9-21 (2011).
- 247 Roberts, M. A. *et al.* Stromal Cells in Dense Collagen Promote Cardiomyocyte and Microvascular Patterning in Engineered Human Heart Tissue. *Tissue engineering. Part A* **22**, 633-644, doi:10.1089/ten.TEA.2015.0482 (2016).

- 248 Kelm, J. M. *et al.* VEGF profiling and angiogenesis in human microtissues. *J Biotechnol* **118**, 213-229, doi:10.1016/j.jbiotec.2005.03.016 (2005).
- 249 Garzoni, L. R. *et al.* Dissecting coronary angiogenesis: 3D co-culture of cardiomyocytes with endothelial or mesenchymal cells. *Exp Cell Res* **315**, 3406-3418, doi:10.1016/j.yexcr.2009.09.016 (2009).
- 250 Smart, N., Dube, K. N. & Riley, P. R. Coronary vessel development and insight towards neovascular therapy. *Int J Exp Pathol* **90**, 262-283, doi:10.1111/j.1365-2613.2009.00646.x (2009).
- 251 Dyer, L., Pi, X. & Patterson, C. Connecting the coronaries: how the coronary plexus develops and is functionalized. *Dev Biol* **395**, 111-119, doi:10.1016/j.ydbio.2014.08.024 (2014).
- 252 Olivey, H. E. & Svensson, E. C. Epicardial-myocardial signaling directing coronary vasculogenesis. *Circulation research* **106**, 818-832, doi:10.1161/CIRCRESAHA.109.209197 (2010).
- 253 Reese, D. E., Mikawa, T. & Bader, D. M. Development of the coronary vessel system. *Circulation research* **91**, 761-768 (2002).
- 254 de Bakker, B. S., de Jong, K. H., Hagoort, J., Oostra, R. J. & Moorman, A. F. Towards a 3-dimensional atlas of the developing human embryo: the Amsterdam experience. *Reprod. Toxicol.* **34**, 225-236, doi:10.1016/j.reprotox.2012.05.087 (2012).
- 255 de Boer, B. A., van den Berg, G., de Boer, P. A., Moorman, A. F. & Ruijter, J. M. Growth of the developing mouse heart: an interactive qualitative and quantitative 3D atlas. *Dev Biol* **368**, 203-213, doi:10.1016/j.ydbio.2012.05.001 (2012).
- 256 Wong, M. D. *et al.* 4D atlas of the mouse embryo for precise morphological staging. *Development* **142**, 3583-3591, doi:10.1242/dev.125872 (2015).
- 257 Madden, L., Juhas, M., Kraus, W. E., Truskey, G. A. & Bursac, N. Bioengineered human myobundles mimic clinical responses of skeletal muscle to drugs. *eLife* **4**, doi:10.7554/eLife.04885 (2015).
- 258 Jackman, C. P., Carlson, A. L. & Bursac, N. Dynamic culture yields engineered myocardium with near-adult functional output. *Biomaterials* **111**, 66-79, doi:10.1016/j.biomaterials.2016.09.024 (2016).
- 259 Adler, C. P. Relationship between deoxyribonucleic acid content and nucleoli in human heart muscle cells and estimation of cell number during cardiac growth and hyperfunction. *Recent Adv Stud Cardiac Struct Metab* **8**, 373-386 (1975).
- 260 Adler, C. P. & Friedburg, H. Myocardial DNA content, ploidy level and cell number in geriatric hearts: post-mortem examinations of human myocardium in old age. *Journal of molecular and cellular cardiology* **18**, 39-53 (1986).
- 261 Banerjee, I., Fuseler, J. W., Price, R. L., Borg, T. K. & Baudino, T. A. Determination of cell types and numbers during cardiac development in the neonatal and adult

- rat and mouse. *American journal of physiology. Heart and circulatory physiology* **293**, H1883-1891, doi:10.1152/ajpheart.00514.2007 (2007).
- 262 Rubina, K. *et al.* Adipose stromal cells stimulate angiogenesis via promoting progenitor cell differentiation, secretion of angiogenic factors, and enhancing vessel maturation. *Tissue engineering. Part A* **15**, 2039-2050, doi:10.1089/ten.tea.2008.0359 (2009).
- 263 Strassburg, S., Nienhueser, H., Bjorn Stark, G., Finkenzeller, G. & Torio-Padron, N. Co-culture of adipose-derived stem cells and endothelial cells in fibrin induces angiogenesis and vasculogenesis in a chorioallantoic membrane model. *Journal of tissue engineering and regenerative medicine* **10**, 496-506, doi:10.1002/term.1769 (2016).
- 264 Crisan, M. *et al.* A perivascular origin for mesenchymal stem cells in multiple human organs. *Cell stem cell* **3**, 301-313, doi:10.1016/j.stem.2008.07.003 (2008).
- 265 Caplan, A. I. The new MSC: MSCs as pericytes are sentinels and gatekeepers. *J Orthop Res*, doi:10.1002/jor.23560 (2017).
- 266 Caplan, A. I. All MSCs are pericytes? *Cell stem cell* **3**, 229-230, doi:10.1016/j.stem.2008.08.008 (2008).
- 267 Zhang, W. *et al.* Maturation of human embryonic stem cell-derived cardiomyocytes (hESC-CMs) in 3D collagen matrix: Effects of niche cell supplementation and mechanical stimulation. *Acta Biomater* **49**, 204-217, doi:10.1016/j.actbio.2016.11.058 (2017).
- 268 Steinberg, M. S. Differential adhesion in morphogenesis: a modern view. *Curr. Opin. Genet. Dev.* **17**, 281-286, doi:10.1016/j.gde.2007.05.002 (2007).
- 269 Tomanek, R. J., Ratajska, A., Kitten, G. T., Yue, X. & Sandra, A. Vascular endothelial growth factor expression coincides with coronary vasculogenesis and angiogenesis. *Dev Dyn* **215**, 54-61, doi:10.1002/(SICI)1097-0177(199905)215:1<54::AID-DVDY6>3.0.CO;2-0 (1999).
- 270 Radisic, M. *et al.* Oxygen gradients correlate with cell density and cell viability in engineered cardiac tissue. *Biotechnology and bioengineering* **93**, 332-343, doi:10.1002/bit.20722 (2006).
- 271 Folkman, J. & Hochberg, M. Self-regulation of growth in three dimensions. *J. Exp. Med.* **138**, 745-753 (1973).
- 272 Caspi, O. *et al.* Tissue engineering of vascularized cardiac muscle from human embryonic stem cells. *Circulation research* **100**, 263-272, doi:10.1161/01.RES.0000257776.05673.ff (2007).
- 273 Kreutziger, K. L. *et al.* Developing vasculature and stroma in engineered human myocardium. *Tissue engineering. Part A* **17**, 1219-1228, doi:10.1089/ten.TEA.2010.0557 (2011).
- 274 Stoehr, A. *et al.* Spontaneous Formation of Extensive Vessel-Like Structures in Murine Engineered Heart Tissue. *Tissue engineering. Part A* **22**, 326-335, doi:10.1089/ten.TEA.2015.0242 (2016).

- 275 Rouwkema, J., Koopman, B., Blitterswijk, C., Dhert, W. & Malda, J. Supply of nutrients to cells in engineered tissues. *Biotechnol Genet Eng Rev* **26**, 163-178 (2010).
- 276 Monsuur, H. N. *et al.* Extensive Characterization and Comparison of Endothelial Cells Derived from Dermis and Adipose Tissue: Potential Use in Tissue Engineering. *PloS one* **11**, e0167056, doi:10.1371/journal.pone.0167056 (2016).
- 277 Melero-Martin, J. M. *et al.* In vivo vasculogenic potential of human blood-derived endothelial progenitor cells. *Blood* **109**, 4761-4768, doi:10.1182/blood-2006-12-062471 (2007).
- 278 Langley, R. R. *et al.* Tissue-specific microvascular endothelial cell lines from H-2K(b)-tsA58 mice for studies of angiogenesis and metastasis. *Cancer Res.* **63**, 2971-2976 (2003).
- 279 Craig, L. E., Spelman, J. P., Strandberg, J. D. & Zink, M. C. Endothelial cells from diverse tissues exhibit differences in growth and morphology. *Microvasc Res* **55**, 65-76, doi:10.1006/mvre.1997.2045 (1998).
- 280 Langenkamp, E. & Molema, G. Microvascular endothelial cell heterogeneity: general concepts and pharmacological consequences for anti-angiogenic therapy of cancer. *Cell and tissue research* **335**, 205-222, doi:10.1007/s00441-008-0642-4 (2009).
- 281 Jackson, C. J. & Nguyen, M. Human microvascular endothelial cells differ from macrovascular endothelial cells in their expression of matrix metalloproteinases. *Int J Biochem Cell Biol* **29**, 1167-1177 (1997).
- 282 Camelliti, P., Borg, T. K. & Kohl, P. Structural and functional characterisation of cardiac fibroblasts. *Cardiovascular research* **65**, 40-51, doi:10.1016/j.cardiores.2004.08.020 (2005).
- 283 Puissant, B. *et al.* Immunomodulatory effect of human adipose tissue-derived adult stem cells: comparison with bone marrow mesenchymal stem cells. *Br J Haematol* **129**, 118-129, doi:10.1111/j.1365-2141.2005.05409.x (2005).
- 284 Williams, C., Quinn, K. P., Georgakoudi, I. & Black, L. D., 3rd. Young developmental age cardiac extracellular matrix promotes the expansion of neonatal cardiomyocytes in vitro. *Acta Biomater* **10**, 194-204, doi:10.1016/j.actbio.2013.08.037 (2014).
- 285 Konstandin, M. H. *et al.* Fibronectin contributes to pathological cardiac hypertrophy but not physiological growth. *Basic research in cardiology* **108**, 375, doi:10.1007/s00395-013-0375-8 (2013).
- 286 Mamuya, W. S. & Brecher, P. Fibronectin expression in the normal and hypertrophic rat heart. *J Clin Invest* **89**, 392-401, doi:10.1172/JCI115598 (1992).
- 287 Sevilla, C. A., Dalecki, D. & Hocking, D. C. Regional fibronectin and collagen fibril co-assembly directs cell proliferation and microtissue morphology. *PloS one* **8**, e77316, doi:10.1371/journal.pone.0077316 (2013).

- 288 Sevilla, C. A., Dalecki, D. & Hocking, D. C. Extracellular matrix fibronectin stimulates the self-assembly of microtissues on native collagen gels. *Tissue engineering. Part A* **16**, 3805-3819, doi:10.1089/ten.TEA.2010.0316 (2010).
- 289 Shiraishi, I., Takamatsu, T. & Fujita, S. Three-dimensional observation with a confocal scanning laser microscope of fibronectin immunolabeling during cardiac looping in the chick embryo. *Anat Embryol (Berl)* **191**, 183-189 (1995).
- 290 Sottile, J. & Hocking, D. C. Fibronectin polymerization regulates the composition and stability of extracellular matrix fibrils and cell-matrix adhesions. *Mol Biol Cell* **13**, 3546-3559, doi:10.1091/mbc.E02-01-0048 (2002).
- 291 Herron, T. J. *et al.* Extracellular Matrix-Mediated Maturation of Human Pluripotent Stem Cell-Derived Cardiac Monolayer Structure and Electrophysiological Function. *Circ Arrhythm Electrophysiol* **9**, doi:10.1161/CIRCEP.113.003638 (2016).
- 292 Westermann, D. *et al.* Cardiac inflammation contributes to changes in the extracellular matrix in patients with heart failure and normal ejection fraction. *Circulation. Heart failure* **4**, 44-52, doi:10.1161/CIRCHEARTFAILURE.109.931451 (2011).
- 293 Deb, A. & Ubil, E. Cardiac fibroblast in development and wound healing. *Journal of molecular and cellular cardiology* **70**, 47-55, doi:10.1016/j.yjmcc.2014.02.017 (2014).
- 294 Madamanchi, A. Beta-adrenergic receptor signaling in cardiac function and heart failure. *Mcgill J Med* **10**, 99-104 (2007).
- 295 Matsa, E., Burrridge, P. W. & Wu, J. C. Human stem cells for modeling heart disease and for drug discovery. *Science translational medicine* **6**, 239ps236, doi:10.1126/scitranslmed.3008921 (2014).
- 296 Dell'Era, P. *et al.* Cardiac disease modeling using induced pluripotent stem cell-derived human cardiomyocytes. *World J Stem Cells* **7**, 329-342, doi:10.4252/wjsc.v7.i2.329 (2015).
- 297 Sala, L., Bellin, M. & Mummery, C. L. Integrating cardiomyocytes from human pluripotent stem cells in safety pharmacology: has the time come? *Br J Pharmacol*, doi:10.1111/bph.13577 (2016).
- 298 Mozaffarian, D. *et al.* Heart disease and stroke statistics--2015 update: a report from the American Heart Association. *Circulation* **131**, e29-322, doi:10.1161/CIR.0000000000000152 (2015).
- 299 Nian, M., Lee, P., Khaper, N. & Liu, P. Inflammatory cytokines and postmyocardial infarction remodeling. *Circulation research* **94**, 1543-1553, doi:10.1161/01.RES.0000130526.20854.fa (2004).
- 300 Hsieh, P. C., Davis, M. E., Lisowski, L. K. & Lee, R. T. Endothelial-cardiomyocyte interactions in cardiac development and repair. *Annu. Rev. Physiol.* **68**, 51-66, doi:10.1146/annurev.physiol.68.040104.124629 (2006).

- 301 Fan, D., Takawale, A., Lee, J. & Kassiri, Z. Cardiac fibroblasts, fibrosis and extracellular matrix remodeling in heart disease. *Fibrogenesis Tissue Repair* **5**, 15, doi:10.1186/1755-1536-5-15 (2012).